UNIVERSITY OF CRETE

DEPARTMENT OF PHYSICS

«Current research on photoelectron circular dichroism & 3D design of a PECD nozzle»

Olympia Maliaka

Supervisor:

Dr. Petros Samartzis

Heraklion, October 2020

Contents

Chapter 1. Current research in PECD

1.1 Basics

Chiral molecules are one group of molecules of great importance. By definition, a molecule is called chiral when it is not superimposable on its mirror image no matter the rotations and translations made. Chiral molecules exist in two forms, the enantiomers. Two enantiomers of a molecule are made of same atoms or groups and have almost identical physical properties. The differences in their behavior derive only due to their difference in handedness.

One effect that occurs in chiral molecules is called circular dichroism (CD). Circular dichroism is the differential absorption of left and right-handed circularly polarized light (LHC and RHC, respectively) from chiral molecules with optical activity.[1] Optical activity is a characteristic of gases or solutions of chiral molecules or any medium in general made of chiral substances. When linear polarized light propagates through them, the orientation of the plane of the polarization rotates with respect to the optical axis.[2] Natural circular dichroism or just circular dichroism was first observed by Jean-Baptiste Biot, Augustin Frensel and Aime Cotton in the early 19th century.[3]

The absorption of light by a sample can be described by the absorbance A, defined as $\log(\frac{I}{I_0})$, where I_0 in the intensity of the incident light and I is the corresponding intensity after the light has travelled a distance x through the medium. The absorbance A can be described also as: $A = \varepsilon cx$ (Beer-Lambert law), where ε is the molar decadic absorption coefficient, c is the molar concertation and x is the thickness of the sample. [4,5]

The molar decadic absorption coefficients are different for right circular polarized light and left circular polarized light for chiral molecules. Circular dichroism can then be described as the difference in the molar decadic absorption or simpler the difference in the absorption as:

$$\boldsymbol{\Delta\varepsilon(\lambda) = \varepsilon_L(\lambda) - \varepsilon_R(\lambda)} \text{ (Eq. 1)}$$

Where ε_L and ε_R is the absorption of left circular polarized light (LCP) right circular polarized (RCP) light, respectively.

To better understand circular dichroism, let's consider a symmetric molecule. That achiral molecule having some kind of symmetry for example a plane or a center, uniformly absorbs light.

In contrast, a chiral molecule does not have a reflection plane and therefore any rearrangement of its electron density will not have one either. The electrons move in some kind of helix and the electric field of circular polarized light draws helicities around the propagation axis with constant magnitude. The electric vector of the RCP light draws helicities clockwise, whereas the one of

LCP light draws helicities counter-clockwise. Thus, an asymmetry between the absorption with RCP an LCP light is expected.[5]

Figure 1 shows the absorption (ε) for an asymmetric molecule and the difference in the absorption, that is circular dichroism.[6]

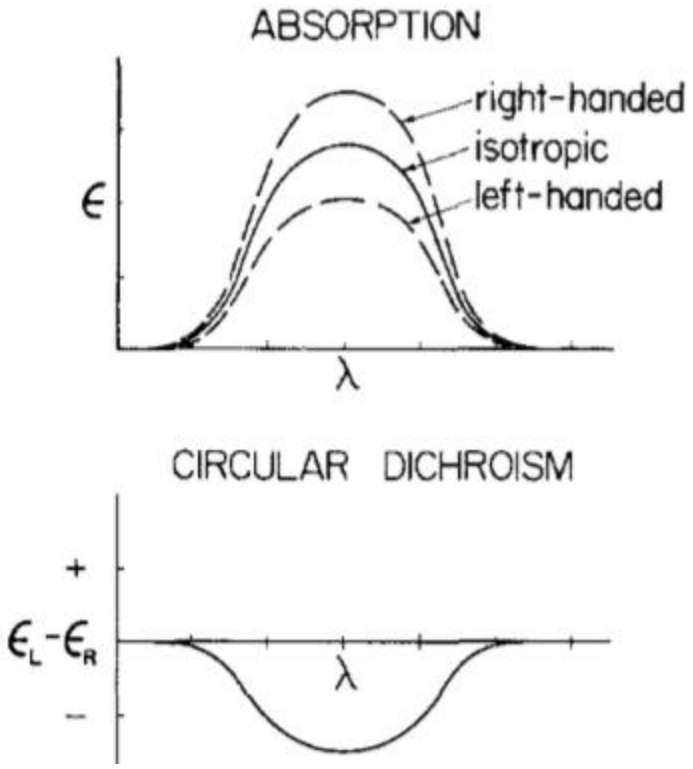

Figure 1. The absorption of light an asymmetric molecule and the corresponding circular dichroism.[5]

Circular dichroism exhibits only in a region of absorption. When measurements of circular dichroism are taken, the light has already diminished due to the absorption. Only weak dichroism can be measured in order to avoid too strong absorption of light.[6] The dissymmetry factor of circular dichroism $g = \frac{I_L - I_R}{<I>}$ rarely exceeds 0.01%.[23] I_L, I_R is the signal obtained with LCP and RCP light, respectively and $< I >$ is the mean or unpolarized signal.

In contrast, the asymmetry due to the Photoelectron Circular Dichroism (PECD) is several orders of magnitude greater.[7] PECD is also a chiroptical effect and is defined as the forward/backward asymmetry of the photoelectron angular distribution with respect to the light propagation axis. It was first predicted by Ritchie in 1976[8].

Ritchie proved the existence of unknown at the time experimental parameters related to the angular distribution of photoelectrons ejected by chiral molecules. The angular distribution of the pre-mentioned photoelectrons are given by:

$$I(\theta) = \sum_L b_L P_L(\cos\theta) \text{ (Eq. 2)}$$

Where P_L is Legendre polynomial of L-order, b_L the corresponding coefficient and θ the angle of ejection defined as the angle between the momentum of the photoelectron and the direction of the incidence photons.

The coefficients b_L are zero for odd L if both or one of the two follow assumptions is made:

- The molecules under investigation are in a statistical state with space-in-version symmetry and
- For each molecule not in a parity eigenstate there is another in the corresponding space inverted eigenstate.

Ritchie showed that the above assumptions do not occur for chiral molecules and thus b_L is important whenever the electric-dipole matrix element depends on the structure of the chiral molecule. Moreover, the first odd Legendre coefficient survives only for chiral molecules and shows dependence on the circular polarization of photons and on the handedness of the molecule. It has opposite sign for the two enantiomers of a specific chiral molecule and it is cancelled for a mixture containing both enantiomers, a "racemic" mixture. If $b_1^{\{p=+1\}}$ is the first order coefficient for RCP light $(p = +1)$, and the corresponding coefficient for LCP light $(p = -1)$ is $b_1^{\{p=-1\}}$ then: $b_1^{\{p=+1\}} = -b_1^{\{p=-1\}}$. Therefore, the forward-backward asymmetry arises when the helicity of the light is changed or when the helicity is fixed and the enantiomer is changed.[9]

Ritchie also expressed the differential cross section in a way in which four 3-J symbols appear and was able to extract the corresponding selection rules. The 3-J symbols are an alternative to Clebsch–Gordan coefficients for adding angular momenta.[10]

Based on them, Ritchie concluded that the angular distribution behaves as $A + C\cos^2\theta$ for a linearly polarized photon and unpolarized target and as $A \pm B\cos\theta + C\cos^2\theta$ for RCP and LCP, respectively. Figure 2 shows the angular distribution of photoelectrons of a model one-electron calculation. The empty circles correspond to linearly polarized light, solid circles to left circular polarization and plus signs to right circular polarization.

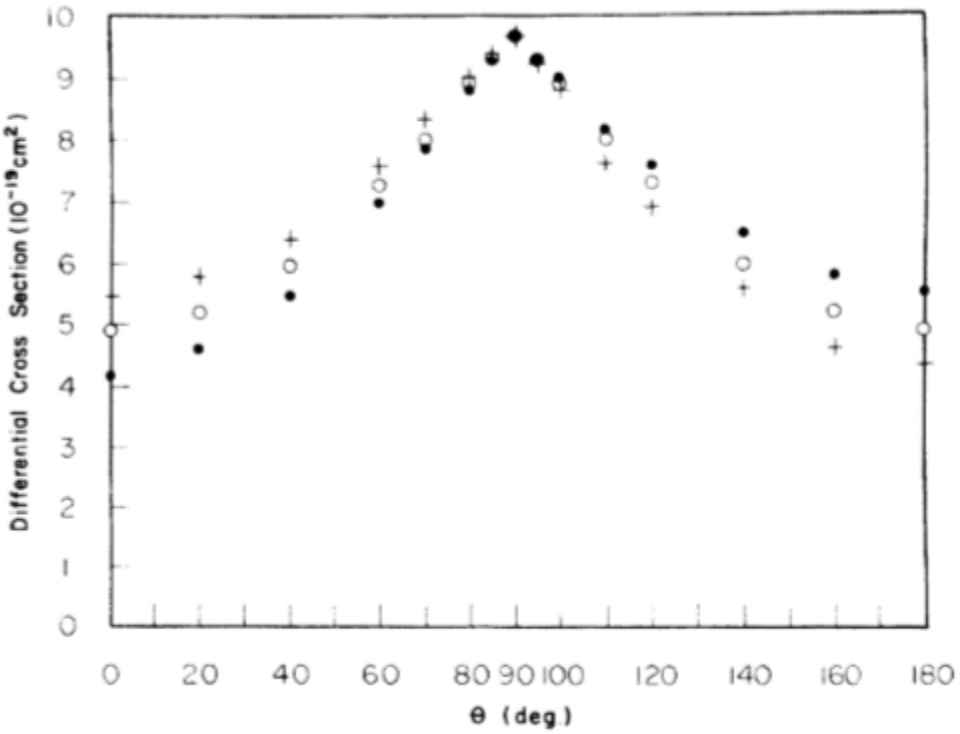

Figure 2. Angular distribution of photoelectrons as calculated from Ritchie for different polarizations of light.[8]

Based on the previous analysis PECD asymmetry factors were obtained. One of them defined by using equation 2 is the difference between the angular distribution of photoelectrons when using left and right circularly polarized light for a given enantiomer[7]:

$$\Gamma(\theta) = I_L(\theta) - I_R(\theta) = 2b_1^{\{+1\}}\cos(\theta) \text{ (Eq. 3)}$$

Another factor for describing PECD for a specific enantiomer is the difference in the photoelectrons passing through equal area elements on the unit sphere in directions 0° and 180° and average over the sphere[7] and is equal to:

$$G_{AD} = |2b_1^p| \text{ (Eq. 4)}$$

With p the helicity of light. Another way to describe the above parameter is having fixed light helicity and measuring the angular distribution at several different angles.

The most common method for probing PECD is measuring the angular distribution of photoelectrons at different angles for either LCP or RCP light. In that way, possible instrumental errors are reduced.

In the case of single-photon ionization, most experiments express PECD in one of the two follow ways[11]:

1. Equation 3 for $\theta = 0$ or

2. $\mathrm{PECD} = \frac{I_{+1f} - I_{-1f}}{(I_{tot})/2} - \frac{I_{+1b} - I_{-1b}}{(I_{tot})/2}$ (Eq. 5)

where I_{pf} is the forward and I_{pb} backward integrated hemisphere intensities defined as: $I_{pf} = \int_0^{2\pi} \int_0^{\pi/2} I_p(\theta) \sin(\theta)\, d\theta d\varphi$ and $I_{pb} = \int_0^{2\pi} \int_{\pi/2}^{\pi} I_p(\theta) \sin(\theta)\, d\theta d\varphi$ and $I_p(\theta) = [1 + b_1^p P_1 \cos\theta + b_2^p P_2 \cos\theta]$ (Eq. 7)

The second way of describing PECD is similar to the one for describing PECD resulting from multi-photon ionization. Only the odd coefficients $b_1^{\{+1\}}$, $b_3^{\{+1\}}$ up to $b_{2n-1}^{\{+1\}}$ contribute to PECD for ionization with 2n photons.

Experiments on PECD are performed in vacuum conditions and the molecules each time under investigation are randomly oriented in the gas phase in a gas cell or in an effusive jet, or in the form of a supersonic molecular beam.[7] Multiple molecules have been examined and experiments on PECD are still carried on with the same molecules for extracting further details or with different molecules and complexes.[12]

The most common samples are camphor and fenchone ($C_{10}H_{16}O$), the enantiomers of methyloxirane (C_3H_6O), trifluoromethyloxirane ($C_3H_3F_3O$) and limonene ($C_{10}H_{16}$). PECD has been probed with synchrotron radiaton, femtosecond laser pulses and in 2019 with nanosecond laser pulses. [13] The first experiment on PECD was made in 2001 by Böwering et al.[14] using synchrotron radiation and will be described later.

1.2 Common experimental methods

The most common experimental methods to probe PECD and record photoelectrons are mentioned here.

In PECD experiments, the molecules are in the form of an effusive gas or supersonic molecular beams. A molecular beam is consisted of cold molecules with approximately same velocities and negligible collisions. The creation of molecular beams will be described in chapter 2.

The propagation axis of the radiation used for ionization (synchrotron, femtosecond or nanosecond laser pulses) is perpendicular to the one of the molecular beam. The proper wavelength for each type of ionization (single-ionization, multi-photon ionization) is selected. The molecules are ionized and emit electrons in different directions and with different velocities. Different types of detectors or set-ups are used to record electrons.

One way to record electrons in the synchrotron case is with Concentric Hemispherical Analyzers (CHAs). Usually, two analyzers are mounted in opposite positions (180°). Such an analyzer consists of two metal hemispheres with their centers of curvature coincident. Different voltages are applied to each of the hemisphere, creating an electric field between them. The photoelectrons insert into the gap between the two hemispheres and depending on their velocity they follow different trajectories. Fast photoelectrons impinge on the outer hemisphere and slow ones are attracted towards the inner hemisphere. As a result, only photoelectrons with a narrow energy region, called pass region, are collected from an electron detector placed at the exit of CHA. At the entrance of CHA, a series of lenses is mounted, capable of retarding the photoelectrons and defining the pass energy. An example of a CHA is shown in Figure 3.

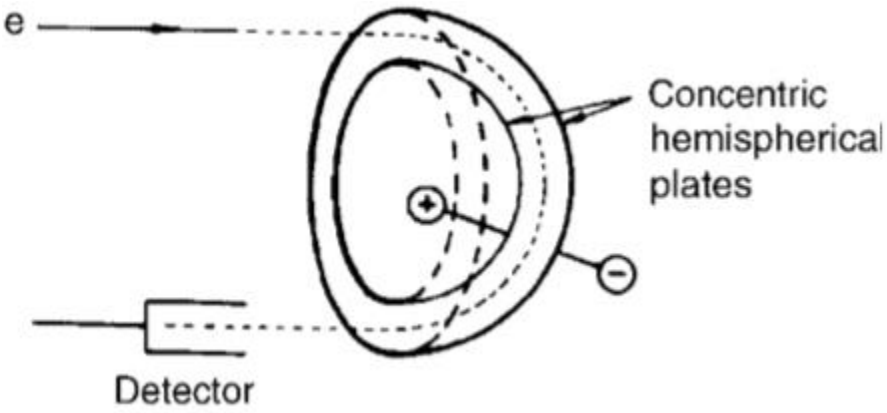

Figure 3. Concentric Hemispherical Analyzer (taken from reference [Error! Bookmark not defined.**] page 295).**

The most common technique utilized in PECD experiments is Velocity Map Imaging (VMI), sometimes combined with Time-of-Flight (ToF) spectrometry or VMI of the corresponding cations. [22,28,30,41,42]

With the VMI method, one can obtain a map of the velocities of the ejected electrons (or ions).[15] A typical set-up used in this method includes three parallel electrodes: repeller, extractor and ground. The radiation interacts with the molecular beam in the region between the repeller and the extractor. Photoelectrons are accelerated due to voltage difference between the repeller and the extractor/ground assembly. The time it takes electrons (or ions) to reach the detector starting from the extractor is called time of flight. Because of the lens, formed by extractor and ground electrodes, the electric field developed is inhomogeneous. Electrons with the same initial velocity originating from different initial positions in the molecular beam-laser interaction volume are focus in a single spot onto a two-dimensional position-sensitive detector.

The 2D image obtained by the VMI method in PECD experiments is the raw data. It can be considered as a discrete representation of the Abel forward transform of the 3D velocity distribution. [16,17] In order to obtain the 3D distribution, an inverse-Abel transformation is applied. Abel inversion is a method for calculating the reconstruction of a circularly symmetric, two-dimensional function from its projection.[18]

One example of the VMI method is shown in Figure 4. In this experiment, two lasers were used: one for photolysis and one for ionization. Ions were recorded instead of photoelectrons. The radius of the Newton sphere expands linearly with time.

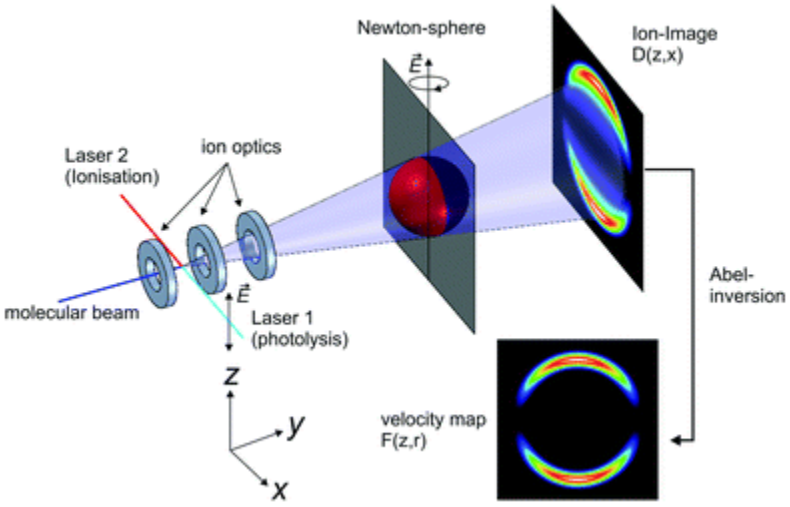

Figure 4. VMI method set up, taken from reference [17].

As mentioned before, the electrons are recorded by a position-sensitive detector. A position-sensitive detector includes an assembly of microchannel plates (MCPs) that amplifies the initial electron event, a phosphor screen as a converter of electrons to photons and a CCD/CMOS camera as a detector of the photon signal. When an electron hit the assembly of MCPs, multiple secondary electrons are emitted. A MCP plate (Figure 5) consists a two-dimensional periodic array of glass capillaries fused together. Across the ends of the MCP voltage difference is applied. The secondary electrons are accelerated by the electric field created. Then, the electrons travel along parabolic trajectories and hit the channel surface, producing more electrons.

This process is repeated multiple times along the channel and the result is a cloud of about a thousand (10^3) electrons. The electrons collide into phosphor and photons are emitted and detected by the CCD camera. [19]

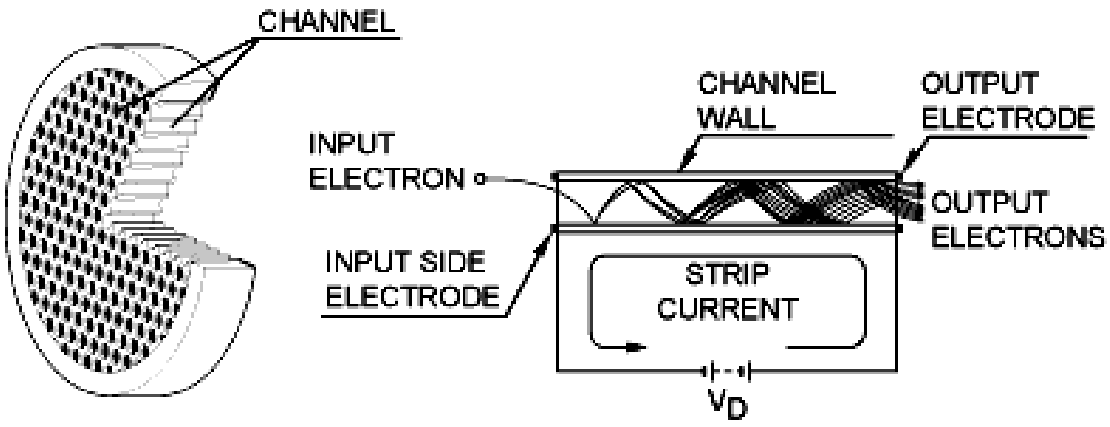

Figure 5. A MPC plate taken from reference [19].

The most commonly used time-of-flight spectrometers consist of an ion source (in PECD experiments it is the molecular beam-laser interaction region) and a collector at the end of an evacuated tube. The formed ions are accelerated towards the collector by an applied electric field. Ions are separated in different branches at the collector. Using a time-of-flight spectrometer, one can obtain the entire mass spectrum, too.[20]

1.3 Synchrotron work

The first time PECD was experimentally observed was with synchrotron radiation, as mentioned before.[14] Bowering et al. in 2001 used VUV light at the Berlin storage ring to ionize bromocamphor molecules. Their experimental set up included two channeltron detectors each mounted on a spectrometer. The spectrometers were facing each other and could rotate around the light propagation axis. The ejected photoelectrons were recorder at multiple angles θ with respect to the light propagation. The experimental set up is shown in Figure 6. The enantiomers were switched sequentially without changing the helicity of light in order eliminate instrumental errors. The electron angular distribution is given by:

$$I(\theta) = \frac{\sigma(\omega)}{4\pi}\left[1 - \frac{\beta}{2}\left(\frac{3}{2}\cos^2(\theta) - \frac{1}{2}\right) + mD\cos(\theta)\right] \text{ (Eq. 7)}$$

The term $\left(\frac{3}{2}\cos^2(\theta) - \frac{1}{2}\right)$ is the 2nd-order Legendre polynomial, m the helicity of the light and $\sigma(\omega)$ the cross section. The parameter β is the magnitude of the non-isotropic contribution to the

PAD due to the 2nd-order Legendre polynomial. The coefficients of order one and two depend upon the polarization and the dynamics of the considered orbital and include both angular momentum coupling terms and electric-dipole photoionization matrix elements. When using linear polarized light $b_1^0 = 0$ and $b_2^0 = \beta$: the anisotropy parameter. Its values range between -1 and +2. [21]

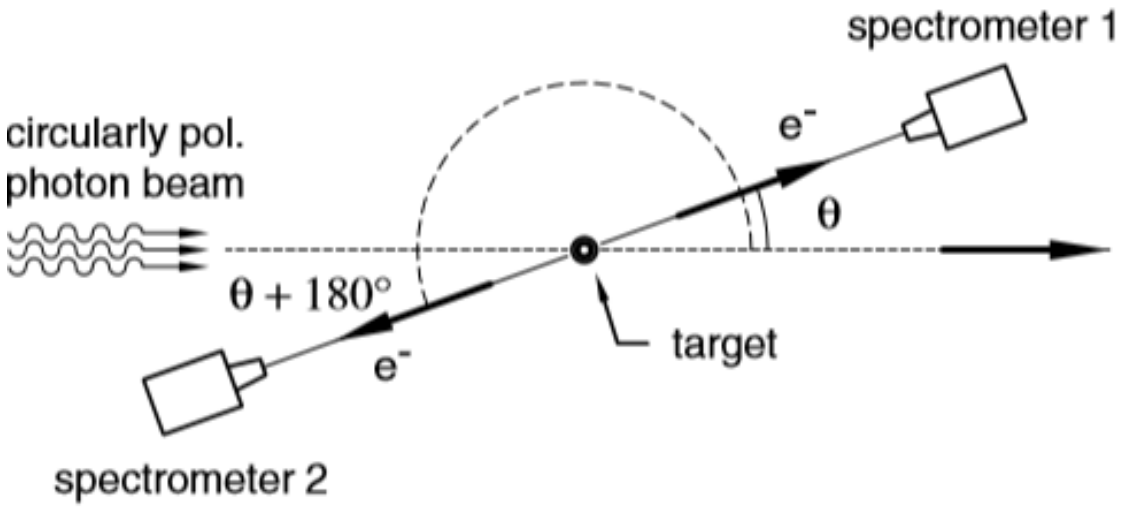

Figure 6. Schematic of the experimental set up used in the first PECD experiment by Bowering et al.[12]

First, the authors recorded the photoelectron spectrum for R-(+)-bromocamphor at the angle of 55°, mentioned as the "magic angle". They chose to take measurements at this angle, because the second Legendre polynomial is zero. In order to express the circular dichroism in the angular distribution (CDAD), the authors inserted the follow parameters:

- $A_{CDAD}(\theta) = \frac{I(\theta) - I(\theta+180°)}{I(\theta)+I(\theta+180°)}$ (Eq. 8)
- $A_{CDAD}^{\pm} = \frac{1}{2}[A_{CDAD}^{+} - A_{CDAD}^{-}]$ (Eq. 9) and
- $D = \sqrt{3}A_{CDAD}(\theta)$ (Eq. 10)

Figure 7 show the above parameters as functions of the binding energy. Figure 5b concerns equation 8. The samples were switched sequentially to eliminate instrumental errors and the results for RCP and LCP light at the magic angle are shown. The R enantiomer was ionized with LCP light (σ^-) and the S enantiomer with RCP (σ^+) light.

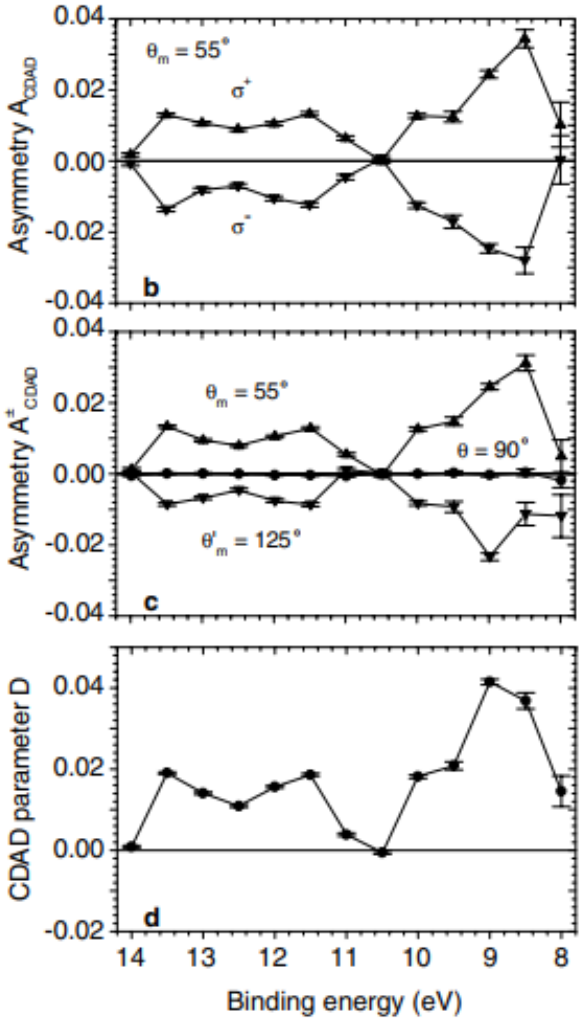

Figure 7. The parameter of asymmetry CDAD as a function of the binding energy.[12]

The magnitude of the asymmetry in figure 5b is of the order of 3%. The sign of the parameter in equation 8 changes with the change in light's helicity.

Equation 9 takes into consideration the change in sign. Figure 5c shows $A^{\pm}_{CDAD}$ calculated in different angles again for RCP and LCP light. It is zero when measured at 90° because of the dependence of light's intensity on cosθ and it reverses its sign from 55° to 125° as expected. As cosθ at 55° and 125° is $\pm 1/\sqrt{3}$ the authors introduced the parameter in equation 10. Figure 7d shows this parameter as derived by averaging the results for the ionization of R-(+)-bromocamphor with RCP and LCP light at both the angles 55° and 125°. The parameter D is positive for all binding energies in contrast with the other two parameters.

The authors mentioned that the dichroism in Figure 7d is due to several orbitals with delocalized electron density over large regions of bromocamphor. For binding energy of 9 eV the corresponding dichroism peak is due to a single orbital with delocalized electron density spread

onto several atoms. This suggests that CDAD arises due to the chirality of electron distribution in this fairly localized region.

The following years more experiments took place using different molecules as samples, providing thus more information about PECD. Two years after the first experiment, Garcia et al. fully measured the PECD asymmetries from a selected valence orbital of pure enantiomers of camphor.[22]

The experiment occurred at the Super-ACO storage ring. As far as the radiation is concerned, the beamline operated between 5 eV and 40 eV energy. In this experiment, first the enantiomer was fixed and the helicity of light was changed and then the opposite occurred. The ions and the ejected electrons were detected by different position sensitive detectors. The selected valence orbital of ionization was the outermost of camphor, with vertical ionization energy at 8.6 eV. Their results are shown in Figure 8 and Figure 9.

Figure 8 shows the 2D projection images of PECD at an energy of 9.2 eV using RCP and LCP light. The upper images show the difference between RCP and LCP light for the two enantiomers and the bottom images show the difference between the two enantiomers for a certain helicity. PECD is described by the difference in intensities with RCP and LCP light:

$$A_{CDAD}(\theta) = 2\, b_1^{-1} = I_{RCP}(\theta) - I_{LCP}(\theta).$$

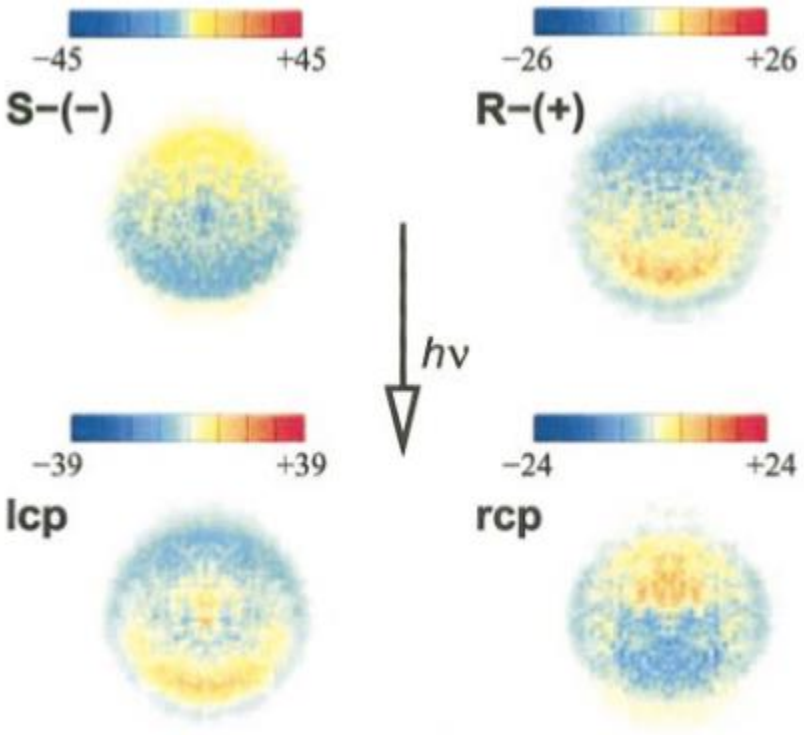

Figure 8. 2D projection images of PECD at an energy of 9.2 eV using RCP and LCP light.[22]

Figure 7 shows the CDAD measurements for the two enantiomers at energy of 9.2 eV. The lines are the best fit functions $A_{CDAD} * \cos\theta$, with $A_{CDAD} = -0.027$ and $A_{CDAD} = +0.026$ for the S-(-) and R-(+) enantiomer, respectively.

The chiral angular distribution parameter for camphor was found $|b_1^{-1}=0.013\pm0.003|$ at 9.2 eV corresponding to an asymmetry of 2.65% in PADs between 0° and 180°.

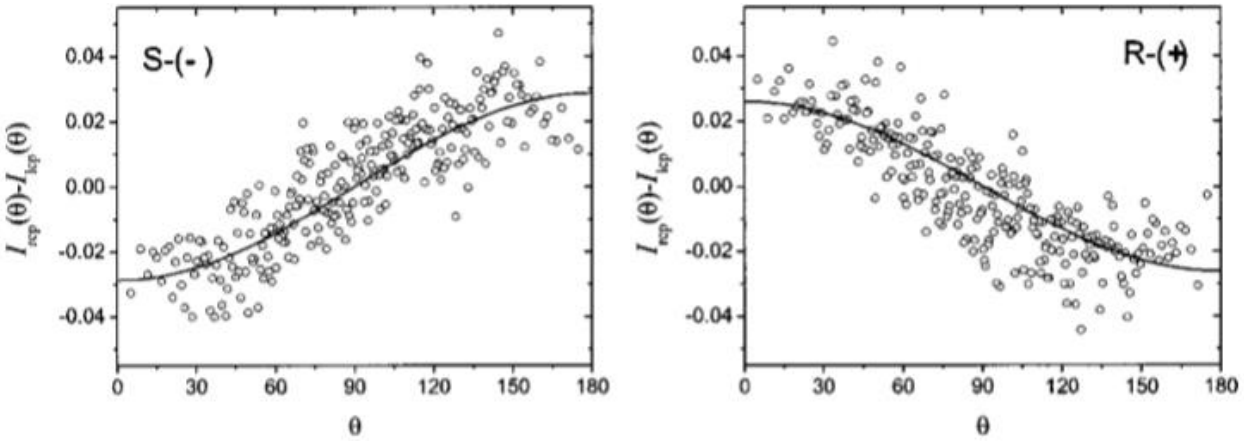

Figure 9. The PECD observed for the two enantiomers of camphor at the energy of 9.2 eV.[22]

The research of Garcia et al. demonstrated that indeed there is asymmetry of the chiral distribution parameter and confirmed the theoretical expectations.

In 2006 Nahon et al. probed CD of valence photoelectrons produced by the enantiomers of camphor.[23] They used synchrotron radiation and the samples were in the form of supersonic molecular beams. The authors used a modified velocity map imaging (VMI) electron/ion spectrometer, named "DELICIOUS".

Figure 10 shows PECD plotted as a function of the ionization energy for fixed photon energy of 20 eV. The magnitude of PECD peaks at around 20% in the region of the highest occupied molecular orbital (HOMO). This magnitude is many orders larger than those extracted with absorption CD.

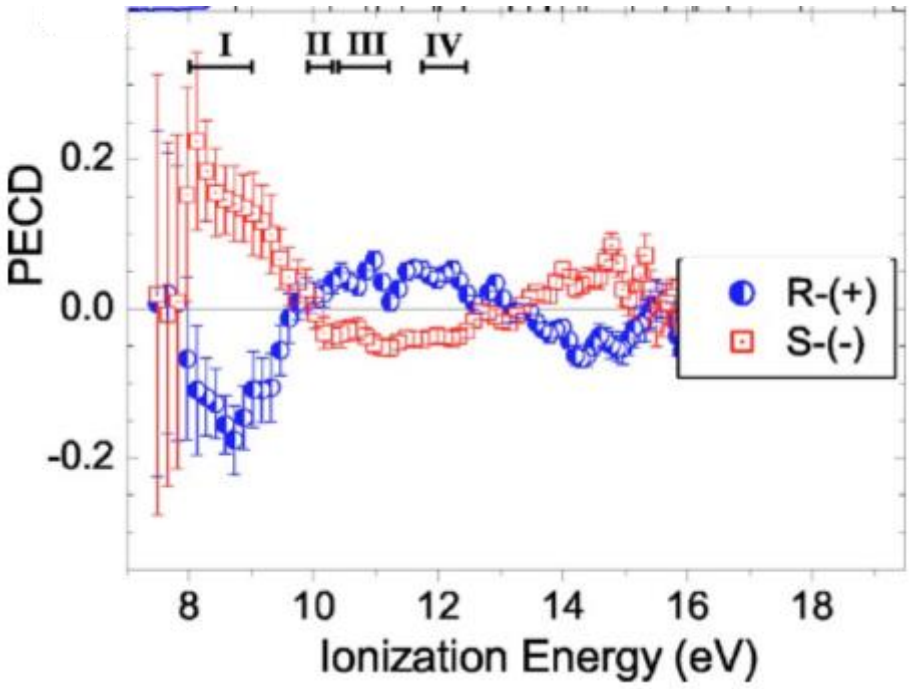

Figure 10. PECD as a function of ionization energy at a fixed photon energy 20 eV.[23]

Figure 11a shows a typical detector image of photoelectrons at an energy of 10.3 eV and Figure 11b and Figure 11c show the dichroism at the same energy. More precisely, Figure 11b and c show the subtraction for different light helicities between R-camphor and S-camphor images, respectively. PECD has opposite sign for the HOMO and HOMO-1 and recrosses zero at 13.5 eV suggesting a correlation with changes in the electronic structure.

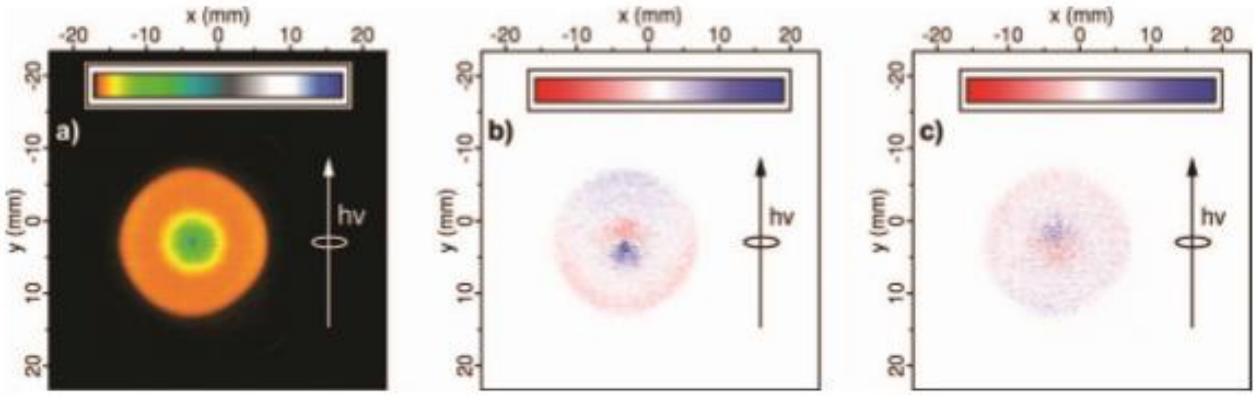

Figure 11. Raw picture of camphor photoelectron at 10.3 eV (a) and the corresponding dichroism (b,c).[23]

In Figure 11a the outer ring corresponds to ionization of the HOMO and the next ring to ionization of the HOMO-1. As far as images b and c are concerned, the asymmetry in intensity and the change in sign are clearly shown. From those figures a 3D image of PECD was extracted as a function of the initial kinetic energy and ejection angle, shown in Figure 12.

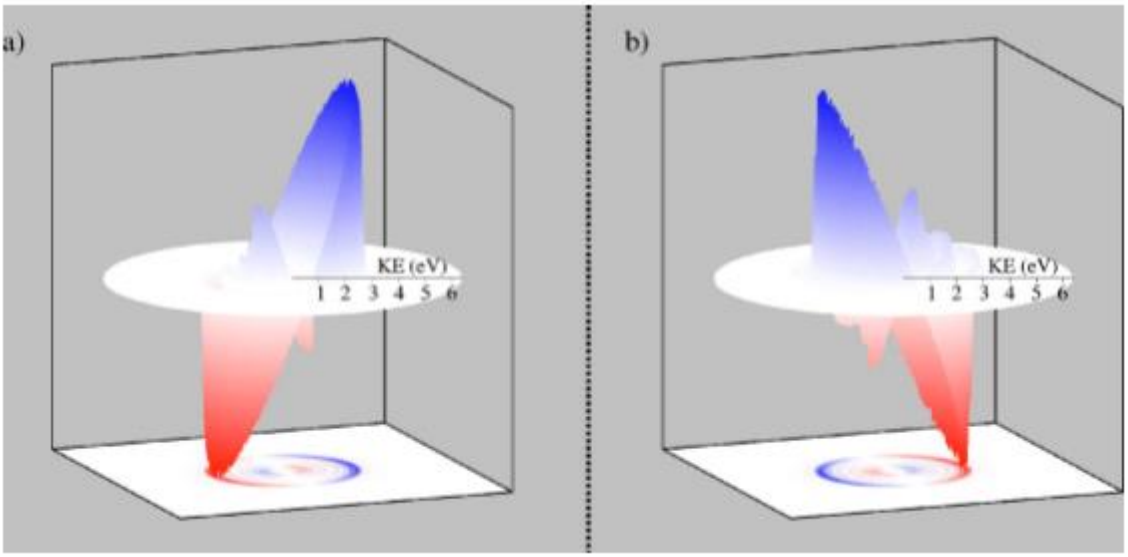

Figure 12. 3D PECD as a function of the initial kinetic energy and ejection angle for a) R-camphor and b) S-camphor.[23]

The cosine dependence of PECD is clear and the peak of the asymmetry is in the forward-backward direction. Furthermore, the corresponding asymmetries for the R enantiomer and the S enantiomer are mirror of each other.

Stener et al. in 2005 used two calculation models, the B-spline linear combination of atomic orbital (LCAO) DFT and CMS-Xα to study the PECD effect of R-(+)-camphor and compared the results with experimental data.[24]

For the B-spline LCAO DFT method an LCAO calculation with the ADF program is made to express the initial ground-state density. The LB94 exchange-correlation potential was chosen. It is suitable for small molecules but it gets too attractive for larger ones and provides inaccurate results. Its high attractiveness, results in a shift to lower energies for the cross section, asymmetry and dichroic parameters. To solve this problem, the authors shifted all the profiles made with the current method by 3 eV.

The potential that the photoelectrons understand is the same for each ionic state and therefore the cross section and the scattering wave function are the same no matter the ionic state. The difference lies in the asymmetry and the dichroic parameters. The orbitals of the molecule under investigation are expanded in a basis made from B-spline radial basis functions.

The CMS-Xα method expresses the molecule into overlapping spherical regions around each atomic center enclosed with outer spherically region. The electron wave functions are then expressed with spherical harmonic function with radial terms. There are two choices between sets of radii for the atomic spheres of the CMS-Xα calculations:

- Fixed and optimized radii for C, H and O and
- The Norman procedure which determines each radius with 0.88 scaling factor.

The authors chose the second option because it provides more stable dichroic parameters.

The continuum wave functions were calculated using as basis the ground-state potential of the neutral molecule and modulated with the suitable asymptotic Coulombic form. This modification can only be adjusted in the outer sphere region and as a result the bound initial wave functions do not change much. However, the initial wave functions were recalculated after the modification and before the calculation of the photoionization matrix elements. The calculations on the latter were within a frozen-core approximation.

Figure 13 and Figure 14 show the calculations made with the B-spline LCAO and CMS-Xα for different ionizations of the molecule R-(+)-camphor.

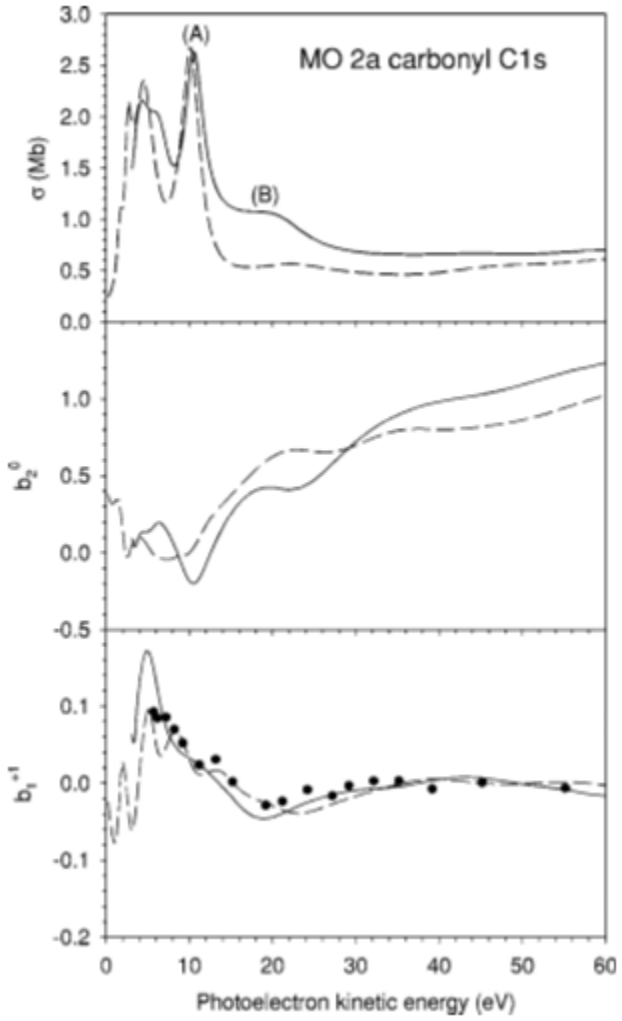

Figure 13. Cross section, asymmetry parameter and dichroic parameter for ionization of the carbonyl C 1s orbital. The solid line is the results with the B-spline LCAO method and the dashed line the corresponding results with the CMS-Xα method.[24]

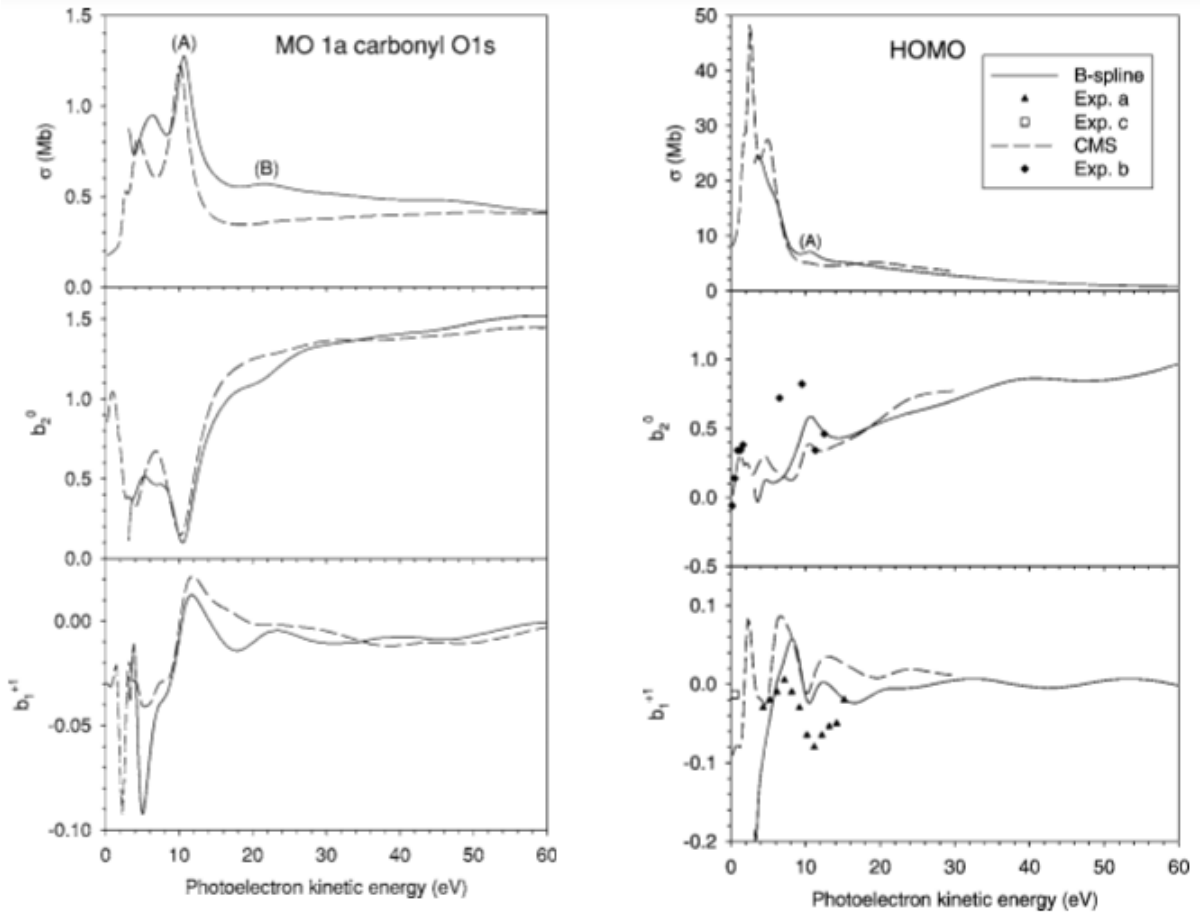

Figure 14. Cross section, asymmetry parameter and dichroic parameter for ionization from the carbonyl O 1s (left) and HOMO (right).[24]

In Figure 13 and Figure 14 (A) and (B) are two discrete maxima at 10.6 eV and 21.5 eV. The shift of 3 eV did not made data available for the region up to 3 eV above threshold.

The theoretical results for the C 1s ionization and HOMO ionization were found in great agreement with the available at the time experimental data. However, there were not available experimental results for the ionization of the carbonyl O 1s and a comparison was not possible. The two methods were found in agreement with each other.

In 2008 similar research with the one described in reference [23] took place by Powis et al. on fenchone.[25] The authors recorded the PES of fenchone, the corresponding PECD asymmetries and the coefficients $b_1^{\{p\}}$.

They compared their results with those found in reference [23] mainly because camphor and fenchone are two molecules with similar structure and their only difference is the site of attachment of two methyl groups, as shown in Figure 15.

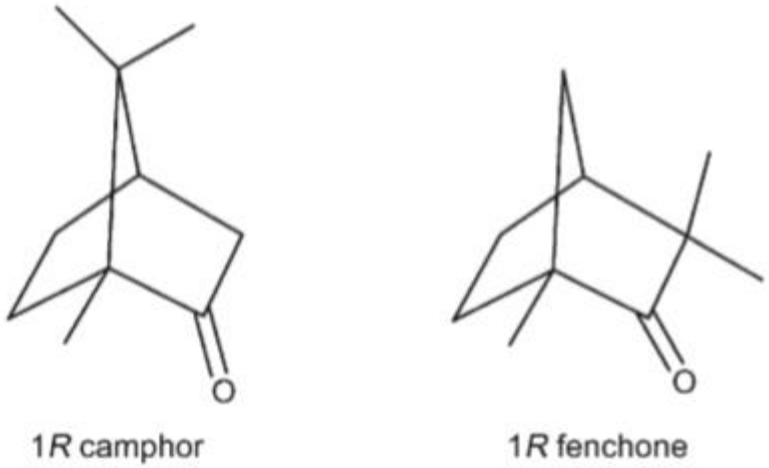

Figure 15. Camphor and fenchone. [25]

For this experiment as the one described in reference [23], synchrotron radiation was used. Furthermore the DELICIOUS spectrometer was used to obtain PAD images for different photon energies.

The PECD asymmetries recorded at photon energy of 19.3 eV are shown in Figure 16. At the upper half of the figure is the VMI-PES of fenchone and at the lower half is the higher resolution spectrum of fenchone at 99 eV.

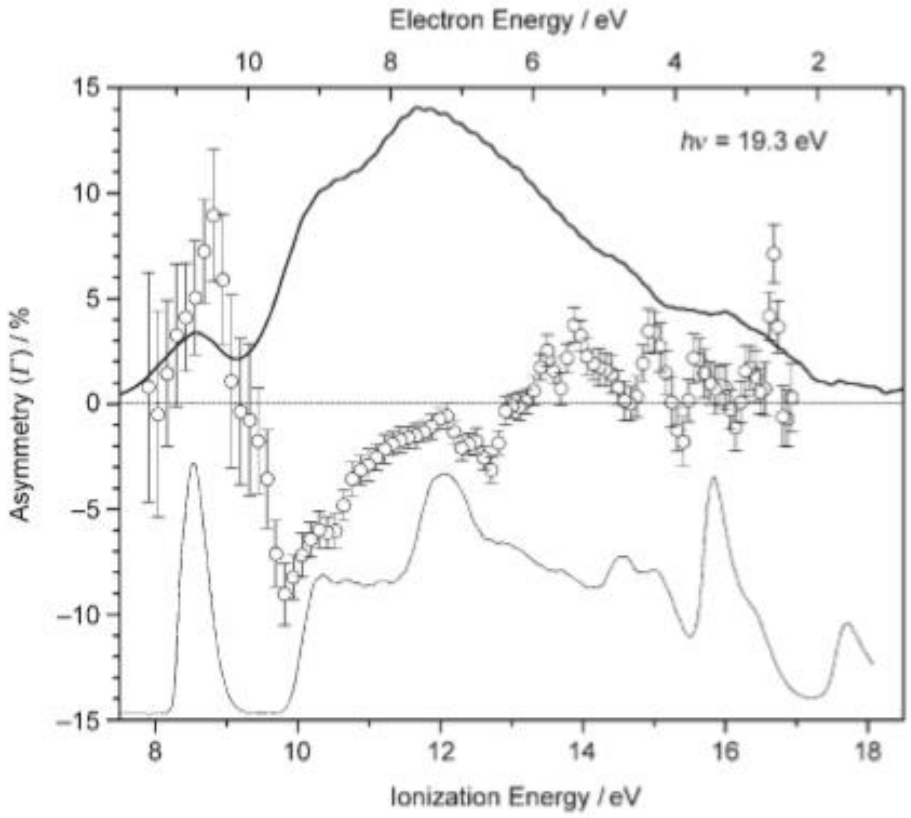

Figure 16. PECD of fenchone at 19.3 eV ionization energy.[25]

At a photon energy of 19.3 eV there is an approximately 8% asymmetry of the HOMO ionization (≈ vertical ionization energy 8.6 eV) band that reverses in the next bands. The magnitude of the asymmetry changes with the energy, which is a sign of dependence between PECD and the orbital of ionization.

Moreover, the comparison of the coefficients for the HOMO ionization and ionization from the region A of the two enantiomers of fenchone is shown in Figure 17.

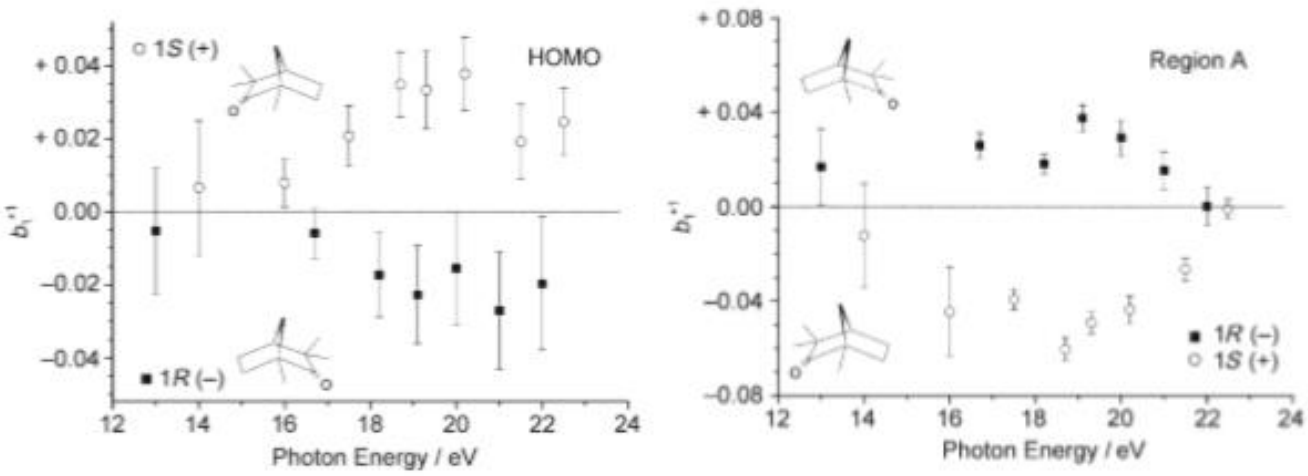

Figure 17. PECD for 1R-fenchone.[25]

The results concerning the left figure have similar trend but opposite sign. The comparison of the results for the HOMO ionization and from the region A ionization, shows sign reversal of the asymmetry for a given enantiomer. This shows the sensitivity of PECD on the ionization orbital. The comparison of the coefficients for camphor and fenchone is shown in Figure 18.

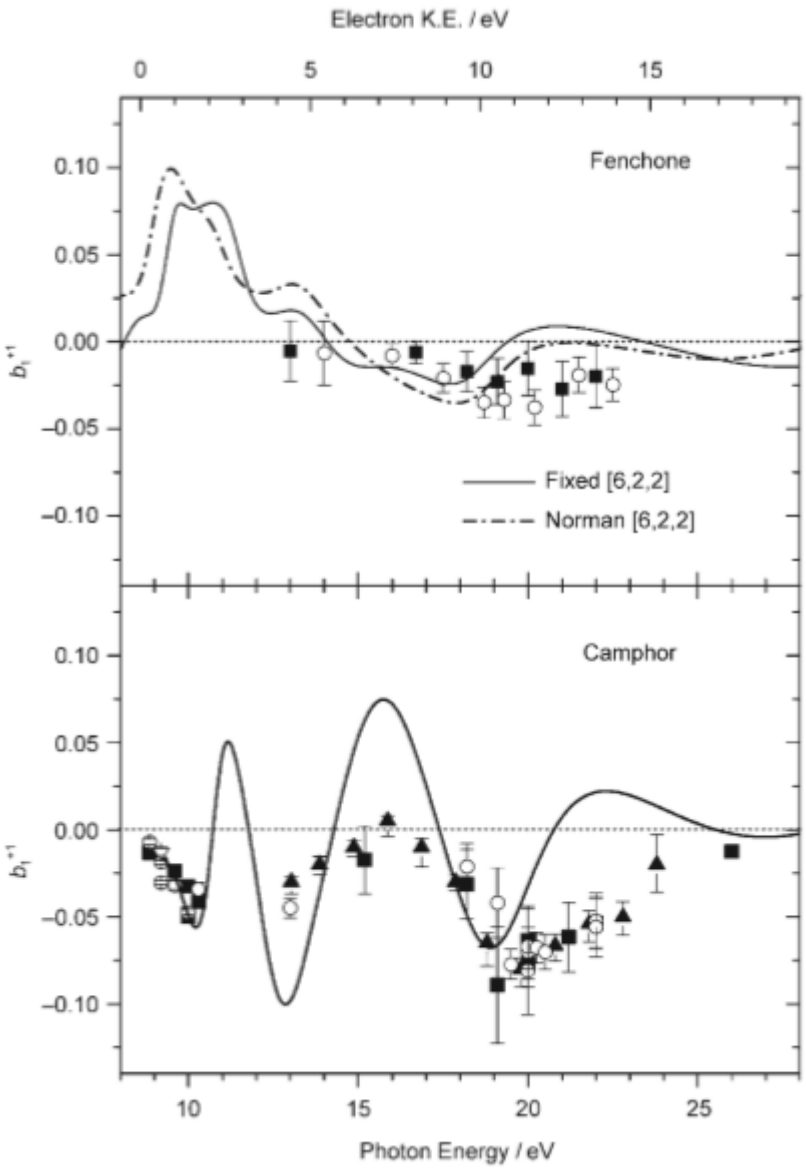

Figure 18. PECD for 1R-fenchone and 1R-camphor.[25] The data for camphor are taken from reference [23]. Filled symbols are for R-enantiomers, open symbols for S-enantiomers. The triangles symbols are from reference [22] and the upside triangle from reference [26].

The two molecules in comparison show similar behavior above photon energy of 16 eV, in the sense that there is a negative peak in both molecules. However, the magnitude of the negative peak in fenchone is less than the half of the corresponding for camphor.

The authors mentioned that the differences between theoretical and experimental data in the region 10-15 eV above threshold are due to shape resonance effects. The differences in the PECD values of fenchone and camphor show the sensitivity of PECD on the molecular structure.

The same experimental set-up and procedure were reproduced for the investigation of the photoionization of glycidol with VUV synchrotron radiation (13–24.4 eV) and the corresponding PECD by Garcia et al.[27] Figure 19 shows the five of the nine conformations of R-glycidol with the lowest energy structures. From them the C1,C2 and C3 are the most stable conformations.

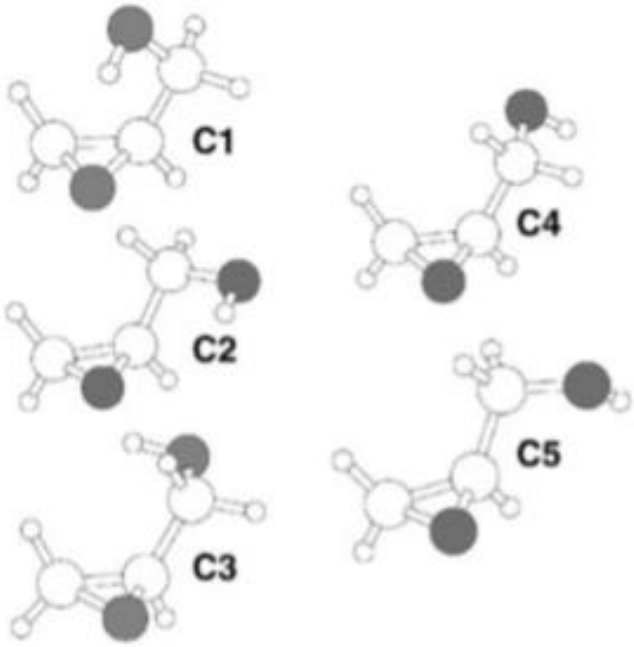

Figure 19. Conformers of R-glydicol.[27]

The authors recorded the valence PES of glucidol and the PECD asymmetries at different photon energies as functions of the electron kinetic energy and the ionization energy. Figure 20 shows PECD asymmetries at a photon energy of 21.2 eV for the two enantiomers of glycidol, the valence PES and the PES for He.

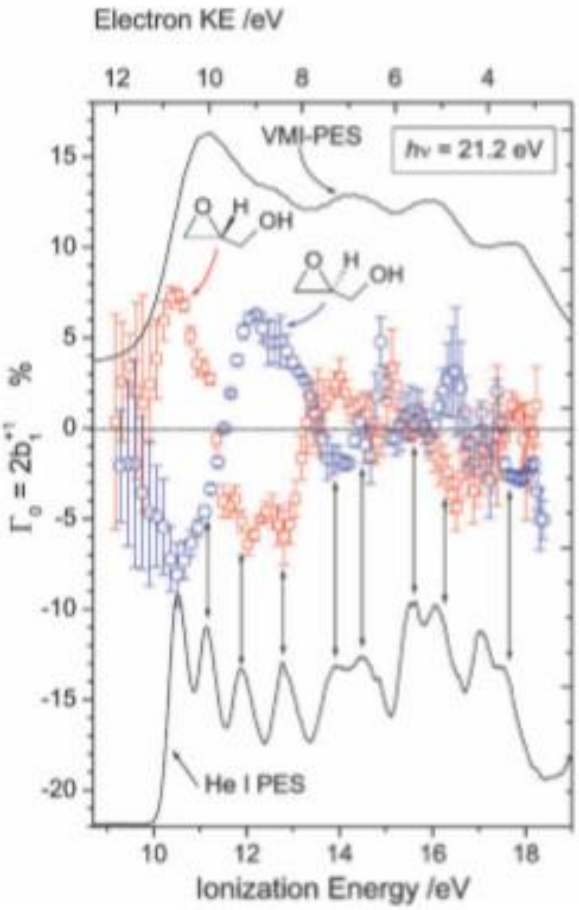

Figure 20. PECD for the two enantiomers of glycidol at 21.2 eV (blue: S-enantiomer and red: R-enantiomer).[27]

The asymmetries are up to 7% and the theoretical expectations of sign reversal with the change of enantiomer are in agreement with the experimental results.

Figure 21 shows the PECD curve for the R-enantiomer at a photon energy of 20.7 eV, the VMI-PES and the He(I) PES.

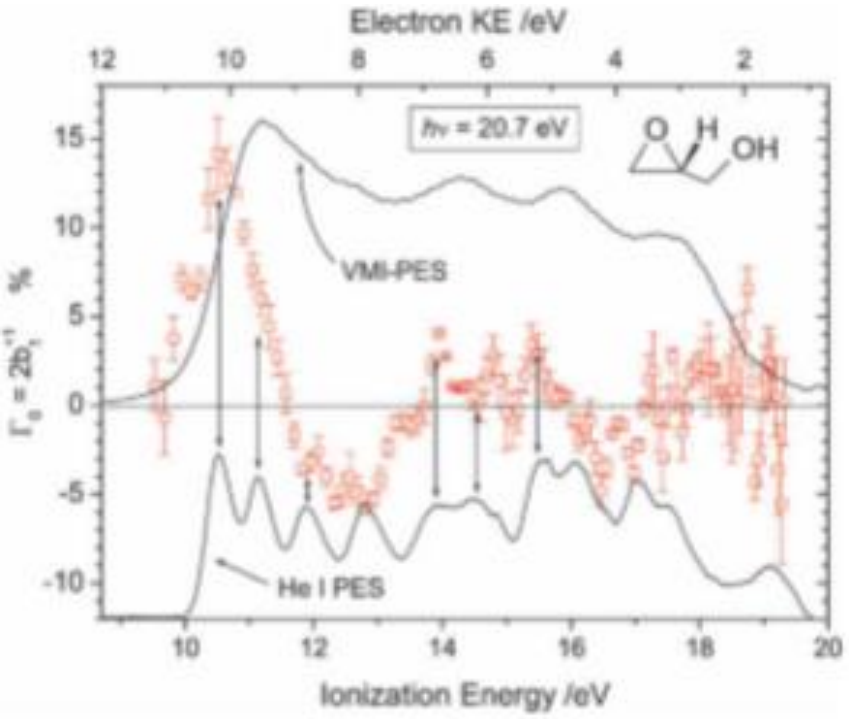

Figure 21. PECD asymmetries for R-glycidol, VMI-PES and He(I) PES. [27]

The PECD curve for photon energy 20.7 eV has significant differences with the one for 21.2 eV. PECD values are up to 15%. The PECD curves relate with the PES curve and thus with the initial orbitals ionized. PECD is sensitive to molecular conformation and therefore it is possible to determine the dominant conformer which in this case is C1.

The authors as previously done in reference [23] calculated the corresponding coefficients $b_1^{\{p\}}$and pointed out that their values vary with small changes in the molecular structure. Last but not least, the authors concluded that the intramolecular H-bond orbital polarization plays a significant role in determining the chiral asymmetry in the electron angular distribution.

Another molecule that has been examined with synchrotron radiation is S-carvone. An S-carvone enantiomer has six different conformations, shown in Figure 22. It has 3 equatorial positions and 3 axial positions for the isopropenyl group with three rotational conformers in each case. The atoms with the black color are oxygens and the asymmetric carbon is drawn with dark grey.[7]

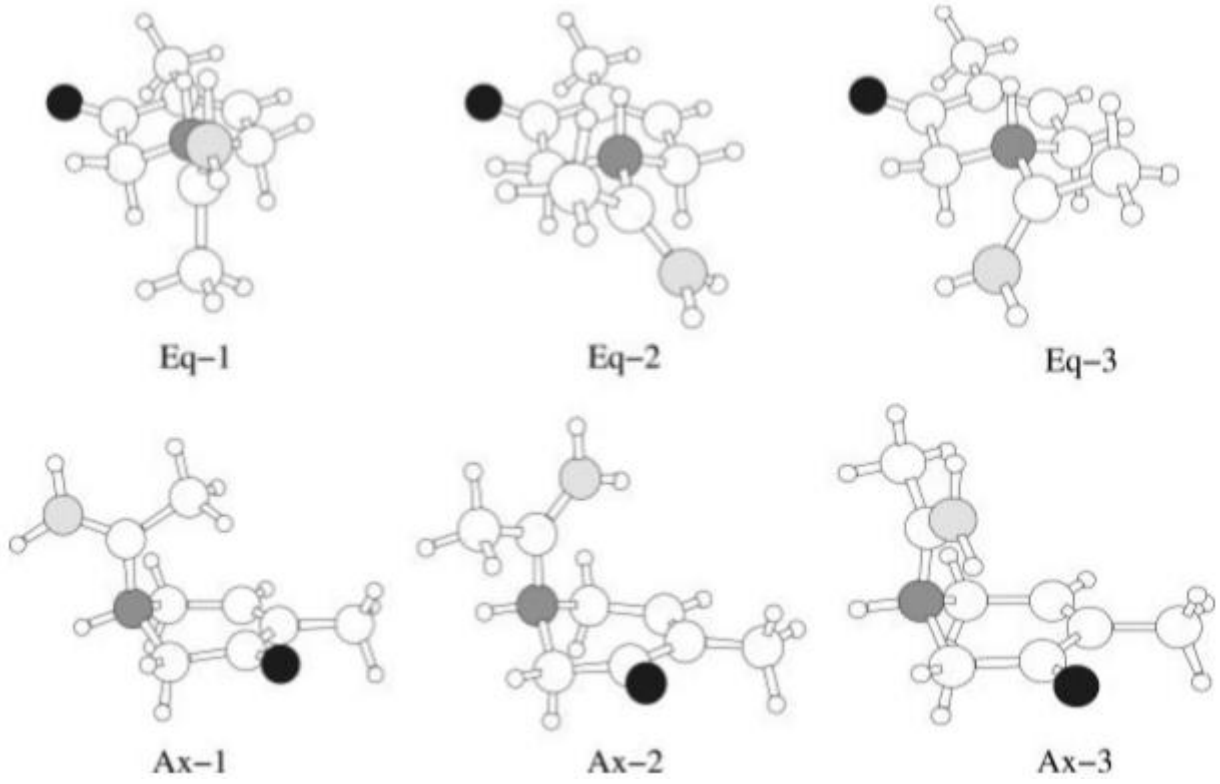

Figure 22. Conformations of S-carvone.[6]

Powis in 2008 examined the (+)-S-Carvone enantiomer in terms of PECD and expressed the results with equations 3 and 4.[7] The experiments were made at the UE56/2 beamline at the BESSY II synchrotron radiation facility, at the soft x-ray regime. Powis used a bettered continuum multiple scattering model for computational purposes using Xα local-exchange potential (CMS-Xα).

Moreover, Powis extracted the X-ray photoelectron spectra (XPS) in the carbon K-edge region for carvone, as shown in Figure 23. Three distinct peaks exist, as shown in the figure. The peak corresponding to the carbonyl group has a value of Γ(54.7°)=6%, thus a forward-backward angular asymmetry G_{AD} of over 10% exists. The values of Γ(54.7°) are obtained from the difference spectrum S_L-S_R and are calculated with equation 11 and are presented point by point in figure 19 wherever they are important.

$$\Gamma(\theta) = 2\frac{N_{+1}I_{+1}(\theta) - N_{-1}I_{-1}(\theta)}{N_{+1}I_{+1}(\theta) + N_{-1}I_{-1}(\theta)} \text{ (Eq. 11)}$$

In equation 11 N are the counts of photoelectrons at θ=54.7° with respect to the light propagation direction. The author chose θ=54.7° because at that angle $P_2(cos\theta) = 0$ as mentioned before and thus the coefficient b_2 is zero and b_1 can be directly determined for either left or right circularly polarized light.

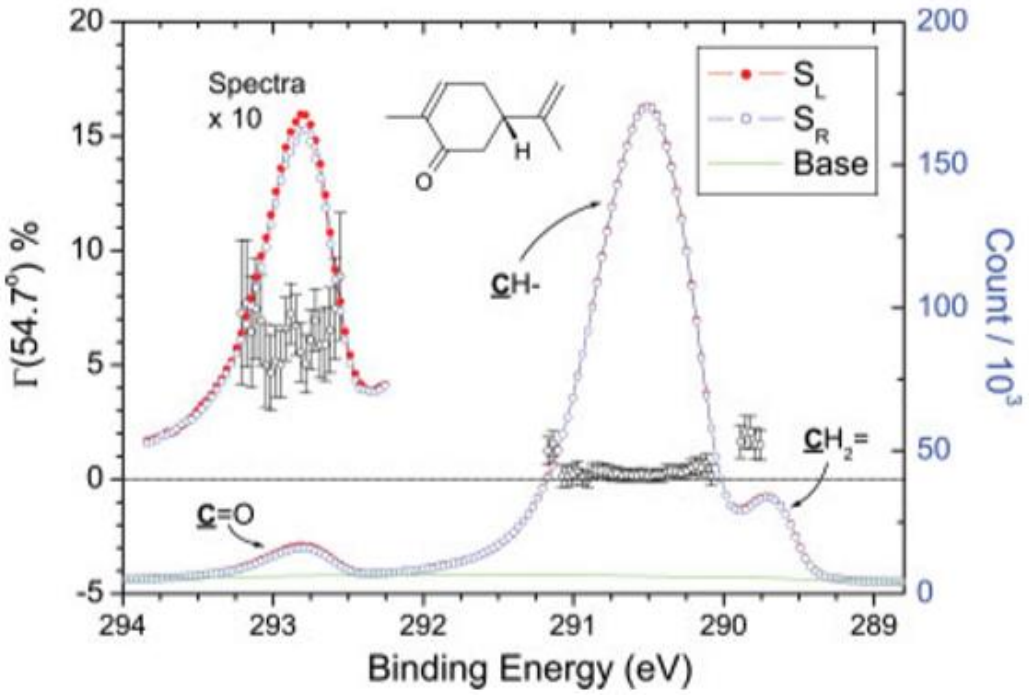

Figure 23. XPS (hv=300 eV) for (+)-S-carvone. SL and SR are recording with LCP and RCP, respectively. The error bars in the left show the normalized asymmetry.[6]

Apart from the above, the author compared the improved and extended CMS-Xα results for the photoionization of the carvonyl groups 1s orbital of each conformer. The results for the three equatorial conformers are similar to each other and the corresponding results for Ax-2 and Ax-3 are not exactly similar with each other and differ a little bit with Ax-1, too. These small differences mean that changing the conformer does not affect the binding energy shift. However, the b_2 coefficients are similar for all conformations apart from Ax-1 and Eq-2 and the b_1 coefficients have different values for axial and equatorial conformations and for each conformer of these group. That means that the chiral part of the angular distribution, that is b_1, is more sensitive to the molecular conformation than b_2. Last but not least, the author mentioned that the dominant contributions to the PECD results are coming from the equatorial conformers.

In 2010 Garcia et al. investigated endoborneol, a molecule similar to camphor but with an important difference.[28] Endoborneol has a C-OH group instead of the C=O group of camphor. This difference leads to a featureless photoelectron spectrum (PES) in endoborneol. Most molecules that had been examined until 2010 had structured PES and thus the authors wished to expand PECD studies to molecules with featureless character and see whether it is possible or not to extract information on photoionization dynamics, conformer population and the absolute configuration using PECD.

The experiments on endoborneol were carried out at the Soleil on the DESIRS VUV beamline. The authors obtained their PECD results by recording multiple images for different helicities of

light and then subtracted them to obtain a difference image. Later on, the pBasex inversion algorithm was used in order to recreate the angular distribution of the difference.

PECD for the enantiomers of endoborneol at an energy of 20 eV and the corresponding featureless PES are shown in Figure 24.

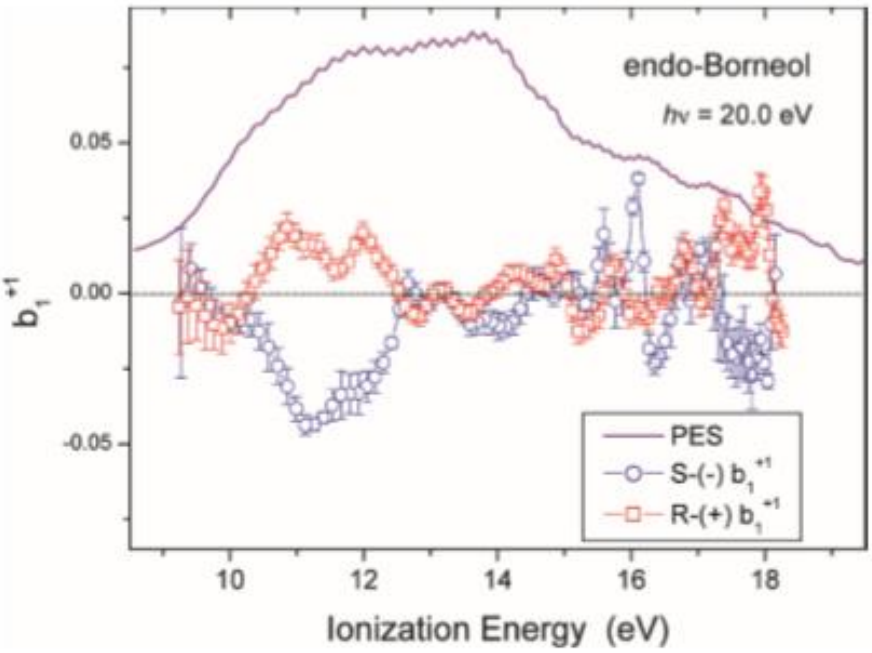

Figure 24. PECD for the enantiomers of endoborneol at photon energy of 20 eV and the corresponding PES.[28]

The lines corresponding to the S-(-) and R-(+) enantiomer respectively show similar behavior but with a sign reversal, as expected. This behavior confirms the molecular origin of the asymmetry. The PECD provides more information in contrast to the featureless PES. The series of minima hints at the underlying changes in orbital contribution to the overall ionization.

Figure 25 shows the calculated (CMS-Xα method) and experimental PECD curves for the S-enantiomer. At energies close to the threshold (18 eV) the vibrational envelope dominates the instrumental contribution, producing uncertainties in the calculations with the CMS-Xα method, because this method does not take into consideration vibrations.

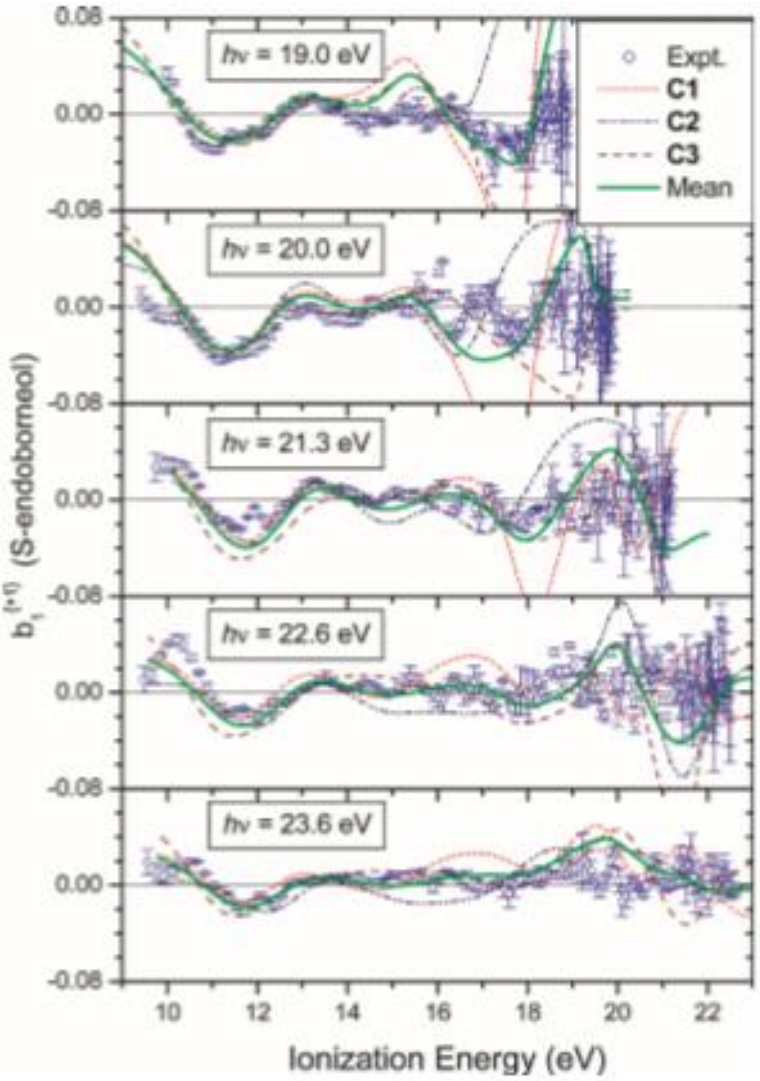

Figure 25. Calculated and experimental PECD spectra for S-endoborneol.[28]

For ionization energies above the threshold it is possible to match the PECD spectra with the simulated one and determine from which conformer the molecular sample is comprised. For kinetic energies above 8 eV the three conformers show similar behavior.. The molecular sample in this experiment had equal populations of each conformer, because the equally weighted average over the three conformers provides better agreement with the experiment than any individual conformer.

In 2013 Garcia et al. showed that PECD depends on the ion vibrational mode excited.[29] They used VUV synchrotron radiation to ionize methyloxirane molecules. When probing vibronic transitions in molecules the corresponding calculations are usually within the Franck-Condon (FC) approximation.

Within this approximation when an electronic transition occurs, the position of the nuclei remains constant and the corresponding transition matrix elements does not depend on the

nuclear geometry during the vibrational excitation. Franck based his approximation on the fact than an electronic transition in a molecule takes place much more rapidly than a vibrational transition. Therefore, in a vibronic transition the nuclei have the same position before and after.[29] As a consequence the parameters describing the electron angular distribution should be the same for different vibrational modes.

The authors showed that the FC approximation breaks down with molecular photoionization. More precisely, they probed the PECD effect on methyloxirane with the analysis of Abel-inverted electron images.

The authors extracted from the Abel-inverted images the LCP-RCP difference images and the dichroic parameter b_1 from the radial distribution in the total image. Figure 26 shows the a) raw and b) Abel-inverted difference images obtained with a VMI spectrometer, c) the VMI-PES superimposed with the threshold photoelectron spectrum (TPES) and d) the b_1 curve at 10.4 eV for the HOMO of S-methyloxirane.

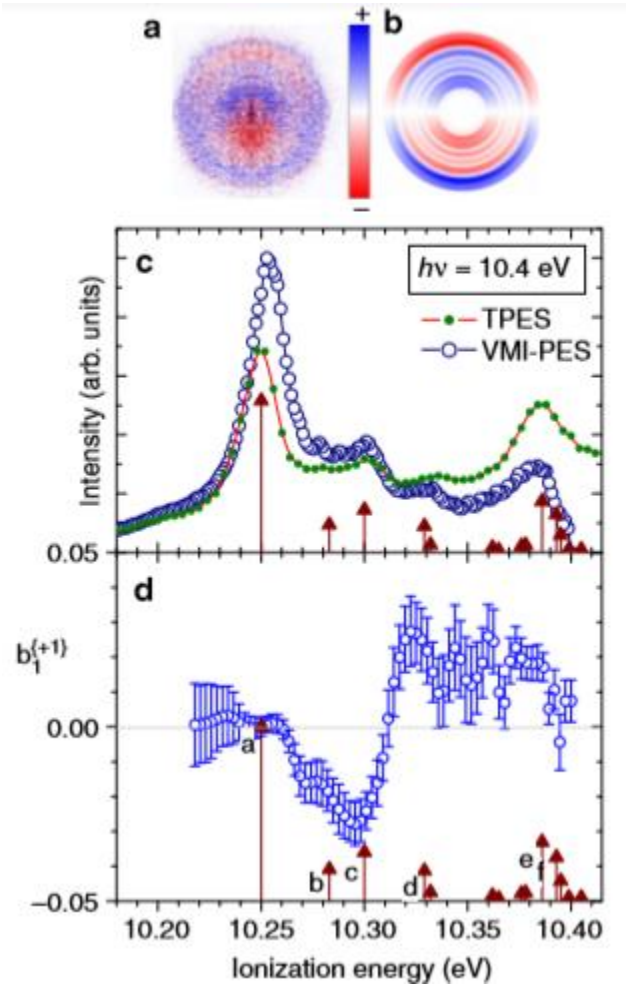

Figure 26. a) raw and b) Abel-inverted difference images, c) PES superimposed with TPES and d) b1 curve for S-methyloxirane.[29]

Figure 26a and Figure 26b reveal a vibrational structure in the radial distribution associated with the forward-backward asymmetries in the angular distribution. The parameter b_1 changes it sign as shown in Figure 26d, suggesting that the forward/backward asymmetry changes its direction for consecutive discrete vibrational modes. This dependence that PECD shows on the vibrational energy is what breaks the FC approximation.

The authors also recorded the PECD asymmetries at 10.7 eV for the HOMO of S-methyloxirane and found the values of b_1 to vary depending on the final vibrational level. Furthermore, b_1 becomes more negative with increasing electron kinetic energy for all vibrational energies.

Later on in 2014 Garcia et al. studied the valence shell gas phase photoionization of trifluoromethyloxirane (TFMOX) and methyloxirane (MOX) and compared the results of the two molecules.[30] For the ionization the authors chose synchrotron radiation. They recorded the PES and PECD curves for different photon energies. In Figure 27 the corresponding results are shown at a photon energy of 17 eV.

The PECD effect is described as $2b_1^{\pm 1}$ .The sign of the coefficient b_1 changes a few times across the PES, indicating the dependence on the ionized orbital. The PECD curve has an additional structure due to individual excitations.

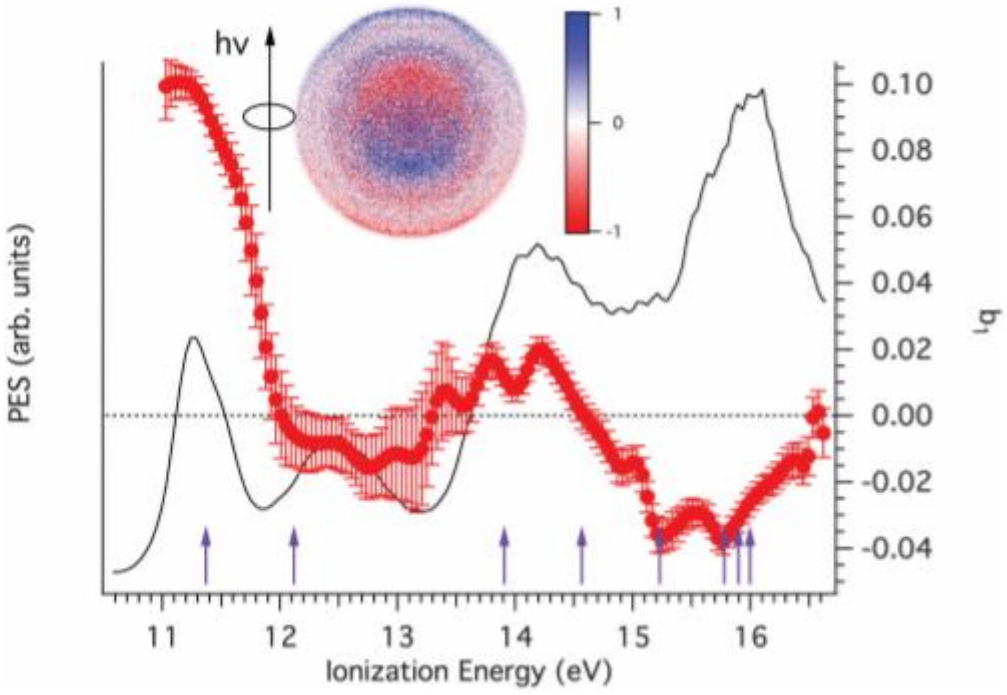

Figure 27. PES (solid line) and PECD (red points) for S-TFMOX for a photon energy of 17 eV. The propagation of the light is shown with the arrow.[30]

For the comparison of the molecules in terms of the parameter $b_1^{\pm 1}$, the authors measured these coefficients as function of the electron kinetic energy for the two outer electronic bands (HOMO

and HOMO-1) of S-MOX and R-TFMOX. Figure 28 presents their results. The filled red circles represent R-TFMOX and the black triangles the S-MOX. The not-colored triangles represent the results from the research of Stranges et al. [31]

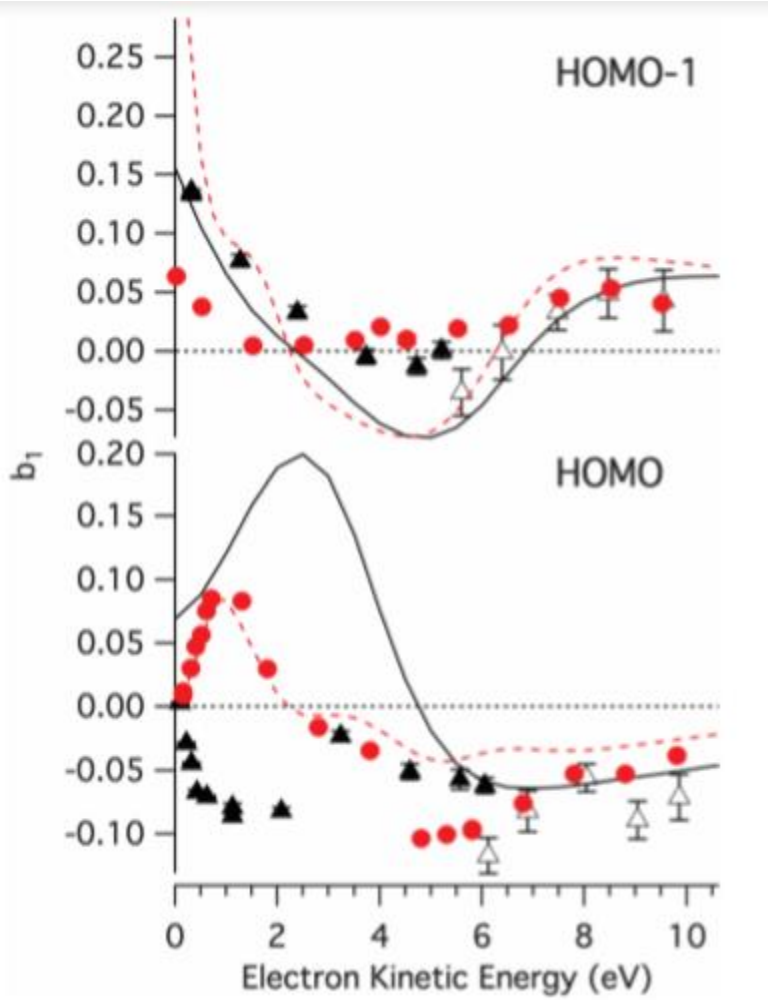

Figure 28. b1 parameter for S-MOX and R-TFMOX as a function of the electron kinetic energy. [30]

For photoelectron kinetic energies above 3 eV the two molecules show similar PECD values for the ionization of HOMO-1. The ionization of HOMO of the two molecules also results in similar PECD with a small diverge around 5-6 eV.

In contrast, for ionization of HOMO or HOMO-1 with kinetic energies below 3 eV the PECD values for S-MOX and R-TFMOX are not similar. This effect can be explained by considering the scattering of photoelectrons which is more sensitive to the molecular potential at low energies. Thus, PECD is sensitive to the effective potential of the molecule and not only to the nature of the initial state.

In 2017 Catone et al. experimentally and theoretical probed PECD arised by the ionization of the outer valence and C 1s core states of 1-amino-2-propanol with synchrotron radiation, compared

their results with the theoretical calculations and compared the dichroic D_{exp} parameter of alaninol and isopropanolamine defined as equation 12.[32] The values for analinol were taken from reference [63]. Figure 29 shows the conformers of the lowest energy of S-(+)-isopropanolamine.

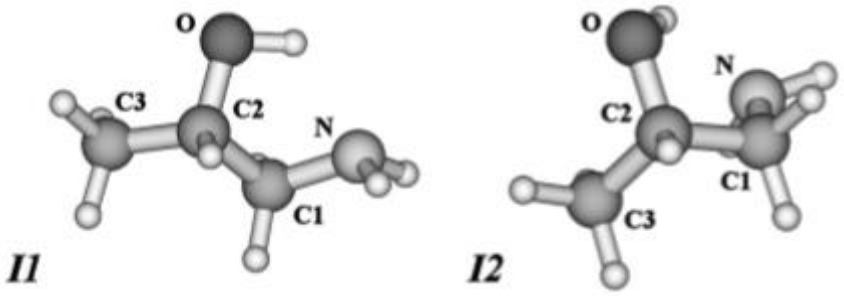

Figure 29. The lowest energy conformers of S-(+)-isopropanolamine.[32]

The authors calculated the valence D_{exp} for the two conformers and compared them with the corresponding theoretical D_B considering only the two conformers of Figure 29. Their results are shown in Figure 30.

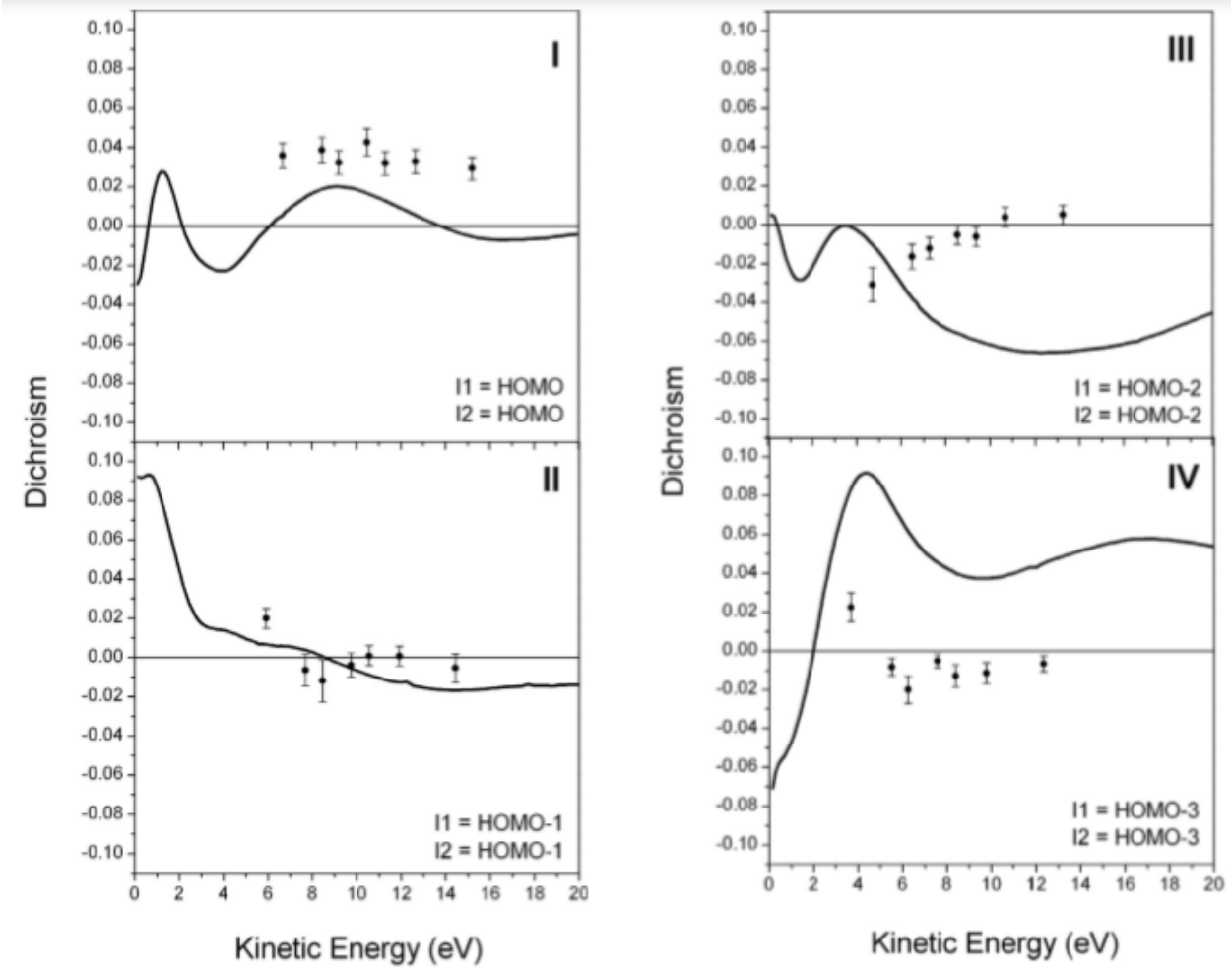

Figure 30. Valence Dexp (dots) and the related DB (solid curve) as a function of the kinetic energy. [32]

The latin numbers in Figure 28 correspond to peaks in the unpolarized PES of the sample measured at a photon energy of 22.5 eV. The comparison showed great agreement in terms of sign and order of magnitude for the HOMO ionization, the one for the HOMO-4 showed agreement in sign and shape but the one for the HOMO-2 and HOMO-3 ionization showed differences in the curve's shape and in sign, respectively.

The comparison of D_{exp} for isopropanolamine and alaninol are shown in Figure 31. The HOMO and HOMO-1 D_{exp} of isopropanolamine and alaninol, respectively show great resemblance in shape but not in energy position.

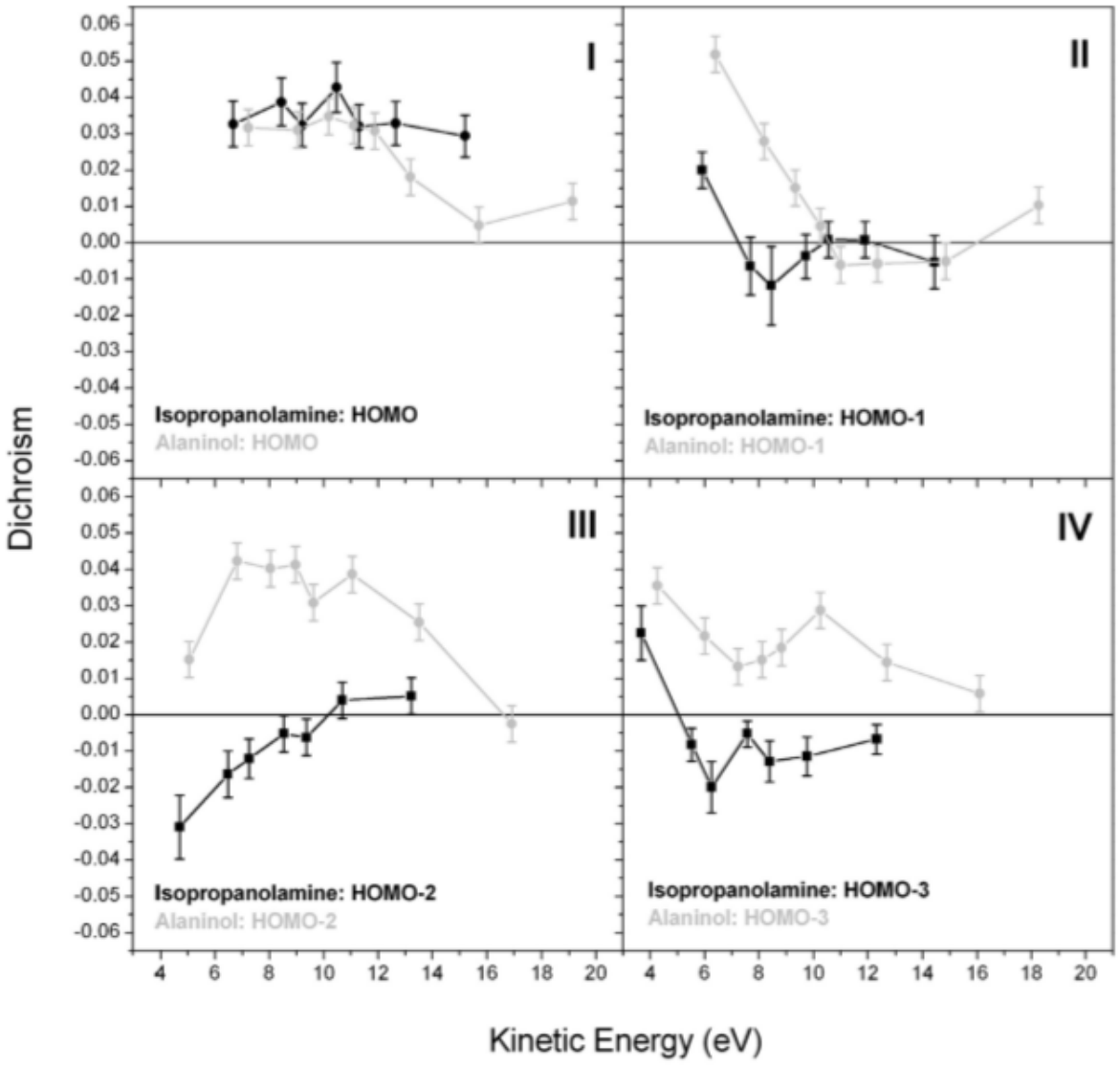

Figure 31. Dexp as a function of kinetic energy of S-(+)-isopropanolamine and S-(+)-alanino.[32]

This suggests that there is N 2p majority contribution in the alaninol HOMO as theoretically expected, confirming the sensitivity of PECD to the character of the orbitals and structure of molecules.

Tia et al. in 2017 calculated and demonstrated as shown in Figure 32 that PECD for certain fixed molecular orientations is larger from the corresponding PECD for randomly oriented molecules and that the PECD asymmetries can theoretically reach 100%.[33]

One way to do this experimentally is to either fix the orientation of the molecule or measure the orientation of the molecule the moment of the photoemission. The authors chose uniaxially oriented methyloxirane molecules ionized with synchrotron radiation of 550 eV.

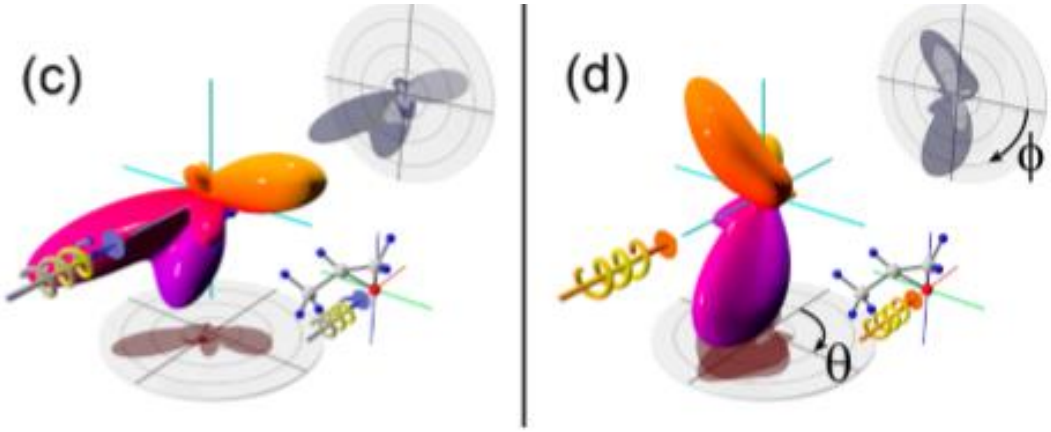

Figure 32. Theoretical PECD for the O 1s-ionization of (+)-R-methyloxirane by LCP (c) and RCP (d) light.[33]

They compared the PECD asymmetries for randomly oriented molecules with those for molecules with fixed-in-space fragmentation axis, as shown in Figure 33.

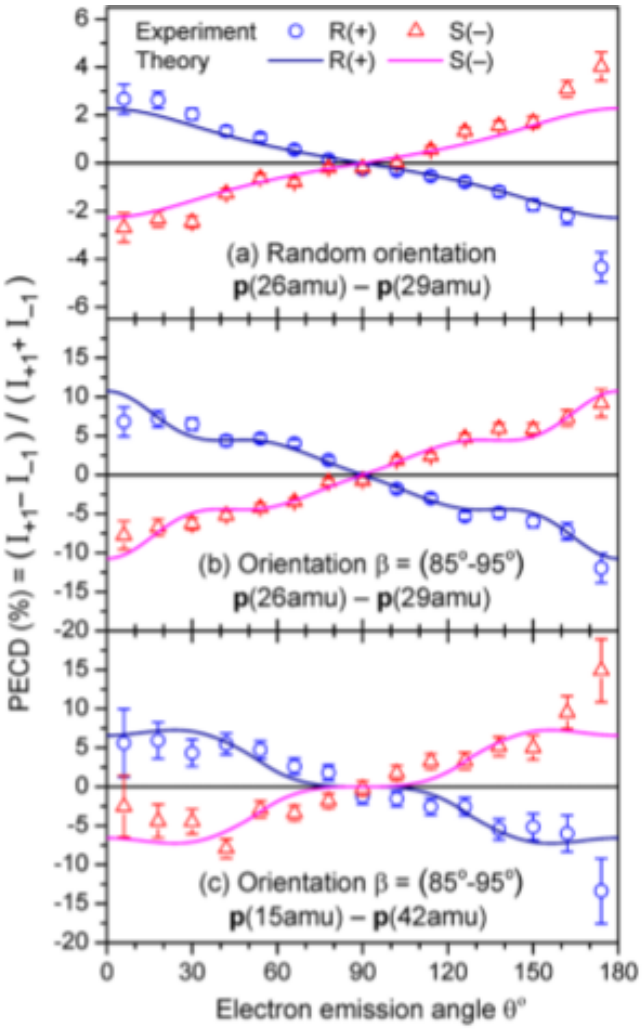

Figure 33. PECD for the ionization of O 1s of the two enantiomers of methyloxirane for a) random oriented molecules, b) and c) fixed-in-space at an angle of 90 with respect to the light propagation axis for different fragmentation channel.[33]

Figure 33 shows a PECD effect about 3-4% for randomly oriented molecules. Concentrating in one specific fragmentation channel can give rise to the PECD effect up to 12%, as shown in Figure 33b.

The authors investigated this effect in more detail and came to the conclusion that choosing a specific orientation of the molecule in space rather than averaging in all orientations does not lead to cancelations and makes PECD an even more sensitive phenomenon for enantiomeric excess determination.

In 2018 Ganjitabar et al. examined the vibrationally-resolved slow photoelectron spectra (SPES) and PECD of α-pinene, β-pinene, 3-carene and sabine with synchrotron radiation and compared their results with available experimental data on limonene.[34] The four molecular samples are shown in Figure 34.

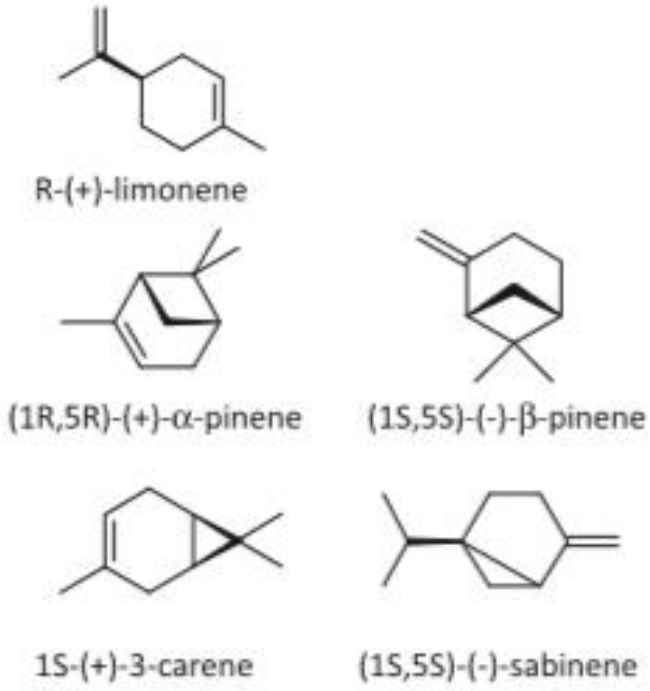

Figure 34. The enantiomers of C10H16 used in reference [34].

Figure 35 shows the PECD results and the corresponding VMI-PES of each molecule. The electrons in the data had been filtered by mass-tagging with the coincidence parent ion with a ratio m/z=136 to diminish background.

The PECD curve of limonene follows the PES curve and changes its sign from valley to peak, as shown in the upper left panel of Figure 35. This feature leads to the conclusion that the preferable direction of the asymmetry flips in step with the vibrational excitation of the molecule. The PECD asymmetries of limonene were up to 5%. Similarly, the PECD of 3-carene also is modulated due to the vibrational features of PES and it was found around 17%. PECD for α-pinene was found about 37%, the largest one observed yet for non-interacting randomly oriented chiral molecules.

The PECD of β-pinene is modulated even though the corresponding SPES and PES do not have strong vibrational features, signing the existence of hidden structures in the SPES and PES.

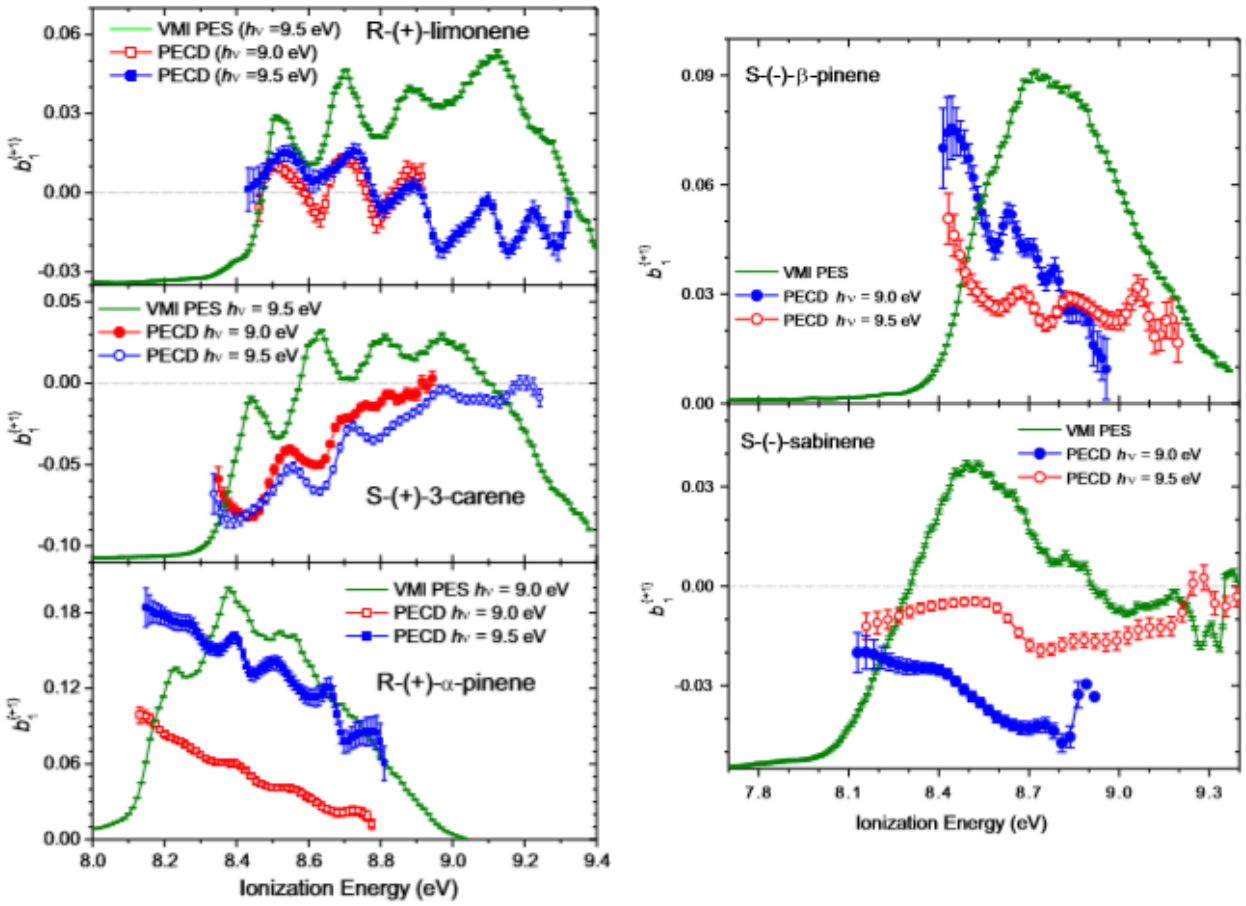

Figure 35. Parent mass-tagged VMI-PES and PECD for C10H16 enantiomers.[34]

In 2012 for the first PECD became accessible with femtosecond laser pulses. However, experiments that use synchrotron radiation are still carried out with promising results. In the next subsection the investigation of PECD with femtosecond laser pulses will be described.

1.4 Femtosecond work

In 2012 Lux et al. successfully observed and probed multi-photon PECD by (2+1) resonance-enchased multiphoton ionization (REMPI) of the HOMO of camphor and fenchone to femtosecond laser pulses.[35] In the (n+m) REMPI process n photons are used to excite electrons to a resonant intermediate state and then m photons ionize the molecule. Therefore, this process gives access to intermediate states; something that single-ionization does not. In contrast with previous experiments with synchrotron radiation, this time asymmetries in all odd Legendre polynomials up to the seventh order were shown.

Their experimental set up included a spectrometer, a quarter wave plate (QWP) for changing the polarization of light and a VMI set up. The PAD images for camphor and fenchone are shown in figure 31.The PECD effect was obtained by subtracting of the RCP image the LCP one of a specific enantiomer.

In Figure 36 the PAD images resulted from the ionization with LIN, LCP and RCP light are depicted. The light propagation is indicated with an arrow. For ionization with LIN laser, there are not asymmetries, as expected. For ionization with LCP laser, an asymmetry arises with respect to the light propagation and for RCP light the same asymmetry exists with reverse sign. The asymmetries are in the range of ±10% for camphor and slightly larger for fenchone.

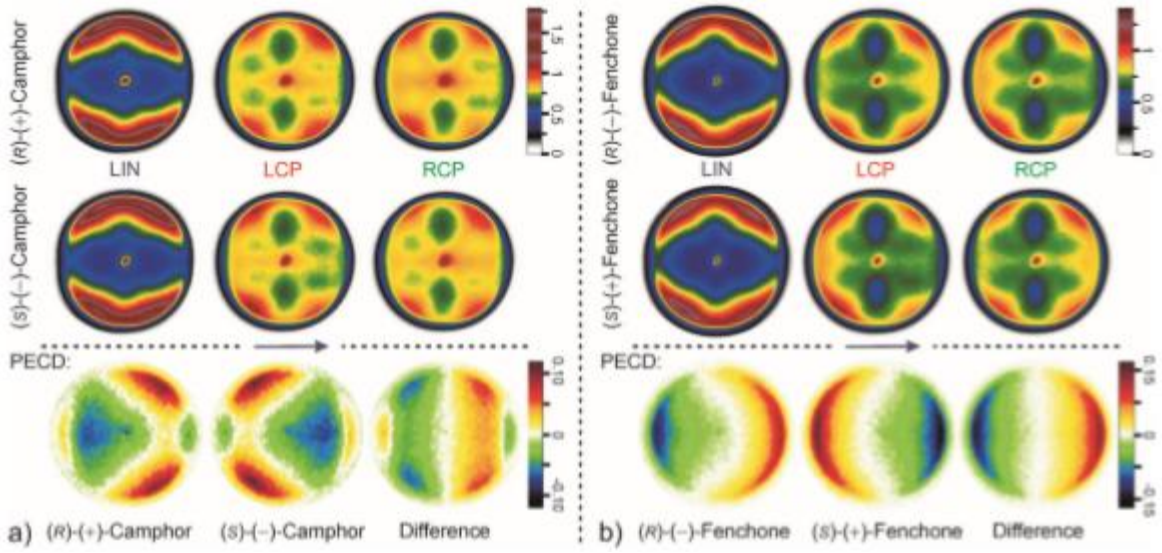

Figure 36. PAD images result from the ionization with LIN, LCP and RCP light of the two enantiomers and PECD.[35]

In 2013 Bhargava Ram et al. used a table top setup with a femtosecond laser and a single image detector for both electrons and ions instead of two different detectors, as done in previous

experiments.[36] They authors used camphor as their sample. The laser was at 398 nm with a duration of 150 fs.

The detection set up included a coincidence imaging set up for eletrons and ions using the VMI method. The detector was a MCP delay-line detector. The experiments were performed with changing the helicity of light. The results are shown in Figure 37.

On both rows the first two images from left are for LCP and RCP light, respectively. The right image in each row is the subtraction of the RCP image from the LCP one, in order for the asymmetry to arise.

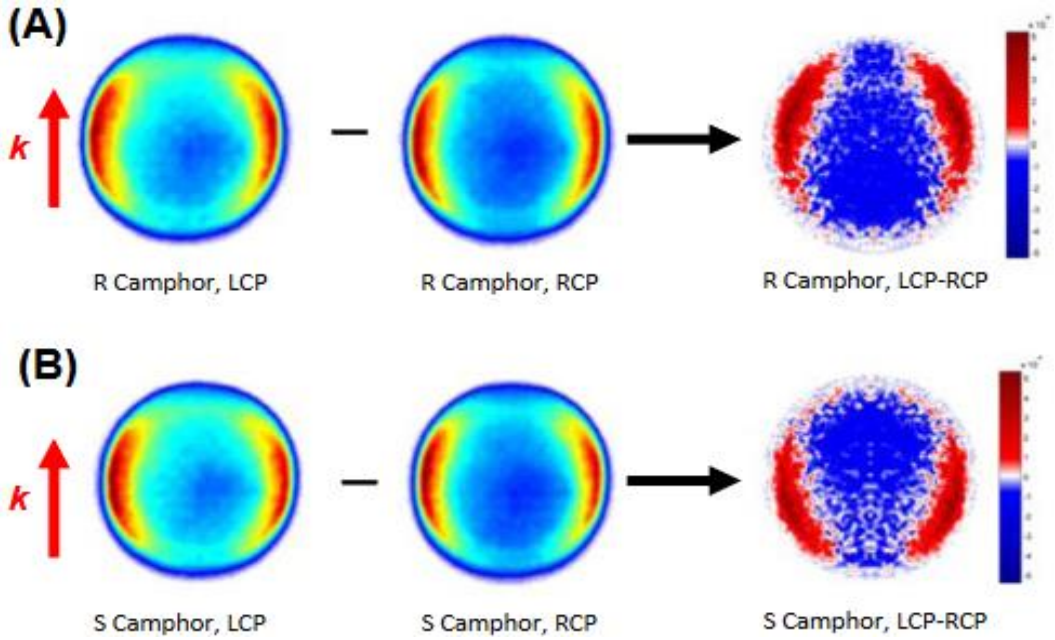

Figure 37. Photoelectron images from (A) R-Camphor and (B) S-Camphor obtained from 3-photon ionization using LCP and RCP femtosecond pulses. The red arrow indicates the laser propagation direction.[36]

The multi-photon PECD was 7.8%, 3 times larger from the one measured in one photon ionization using synchrotron radiation at the same energies.

One year later, in 2014 Rafiee Fanood et al. observed MP-PECD with four-photon ionization of methyloxirane with femtosecond laser pulses of 420 nm wavelength and 150fs duration.[37] Molecules of methyloxirane were ionized in an electro-ion coincidence spectrometer and a time-of-flight (ToF) spectrum of the ions was obtained.

The authors were able to identify the fragments based on their m/z ratio and the parent ions. The ToF spectrum was dominated by the parent monomer with m/z=58. Moreover, the photoelectron kinetic energy (PEKE) distributions were measured and two broad bands were observed that correspond to ionization of the highest and second highest occupied orbitals, HOMO and SHOMO.

The MP-PECD was calculated for 1.3±0.2 eV electrons coincident with m/z=58 parent ions using two quantification methods. The results obtained were compared to each other.

The first method is based on the integrated counts in forward and backward hemispheres (F/B):

$$MP-PECD = \frac{I_{+1f}-I_{+1b}}{(I_{+1f}+I_{+1b})/2} - \frac{I_{-1f}-I_{-1b}}{(I_{-1f}+I_{-1b})/2} \text{ (Eq. 12)}$$

In equation 13, I_{pf}, I_{pb} are the integrated counts in the forward and backward hemispheres, respectively.

The second method in an expression of MP-PECD in terms of the Legendre polynomials (LP) odd coefficients as follow:

$$MP-PECD = 2b_1^{\{+1\}} - \frac{1}{2}b_3^{\{+1\}} + \frac{1}{4}b_5^{\{+1\}} - \frac{5}{32}b_7^{\{+1\}} \text{ (Eq. 13)}$$

The results are shown in Figure 38. The values obtained for the two enantiomers with the two above equations are in agreement.

	MP-PECD^a (LP)	MP-PECD^b (F/B)
S-methyloxirane	0.047 ± 0.012	0.044 ± 0.011
R-methyloxirane	−0.048 ± 0.011	−0.048 ± 0.011
mean magnitude	0.048 ± 0.008	0.046 ± 0.008

Figure 38. MP-PECD for 1.3±0.2 eV electrons coincident with m/z=58 parent ions.[37]

The Legendre coefficients of order 3 and 5 are close to zero, suggesting that the chiral behavior of the molecule is due to the first odd coefficient just as in one-photon ionization. However, the coefficient of the second order is relatively large and those of the fourth and fifth order are non-zero, too. This indicates the involvement of at least three photons.

Lux et al. in 2015 measured the PECD effect and calculated the Legendre coefficients for three chiral molecules with similar absorption spectra: camphor, fenchone and norcamphor by ionizing them with femtosecond laser pulses at 398 nm and full width at half maximum (FWHM) pulse duration of 25 fs. [38]

The authors measured the PAD of threshold electrons ejected by three-photon ionization and compared their results with those obtained for the above threshold ionization (ATI) electrons resulting from four-photon ionization. ATI electrons are called the electrons emitted by molecules that absorb more photons that the necessary number for ionization.[39] The effect occurs in laser pulses short enough to eliminate the influence of collisions. [40]

Figure 39 shows images of PECD for LCP and RCP light. In the central part of each image the asymmetries expected for each molecule appear. For each enantiomer a second energy channel at a larger radius exists which exhibits a PECD effect in the 10% range.

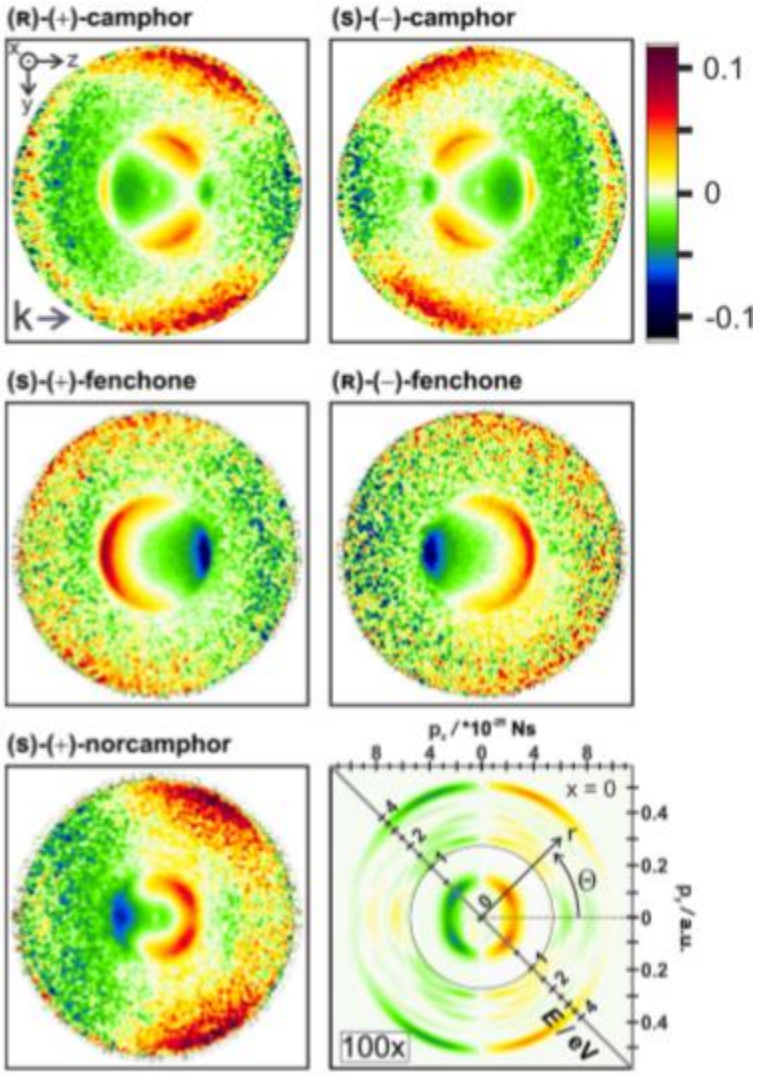

Figure 39. Images of PECD asymmetries in an energy range up to 4 eV excess energy. In the right row the lowest image is the Abel-inverted antisymmetric part of the PECD-image for the (S)-(+)-norcamphor. Θ is the emission angle and r the radius. Signals at excess energies higher than 1 eV are increased by a factor of 100.[38]

In the center of each image the discreet asymmetries of the threshold electrons are shown. Regarding the (S)-(+)-norcamphor the threshold electrons have non-zero PECD along the z-axis in contrast to the ATI electrons which have almost zero PECD. Thus, it seems that the fourth photon adds angular momentum and pushes away the minima and maxima from the z-axis.

For all molecules under investigation the ATI-signal is maximum (3.4 eV for norcamphor, 3.7 eV for camphor and 3.8 eV for fenchone) at such energy corresponding to the absorption of a 384 nm photon.

Furthermore, the authors calculated the Legendre coefficients for the three molecules. Their results are shown in Figure 40. The odd coefficients change their sign as their order increases for both the threshold ionization and above-threshold ionization. The coefficients corresponding to ATI show change of sign in the even coefficients, too.

The almost racemic norcamphor ((+/-)-norcamphor) shows weak amplitudes in the odd coefficients compared to those of the almost pure enantiomeric (S)-(+)-norcamphor.

The even coefficients of all molecules show an increase as the order increases and the odd coefficients are larger for higher photon number. That shows that apart from the threshold electrons, the ATI ones carry the chirality signature, too. Last but not least, even though the molecules under investigation have similar structure, they exhibit different coefficients.

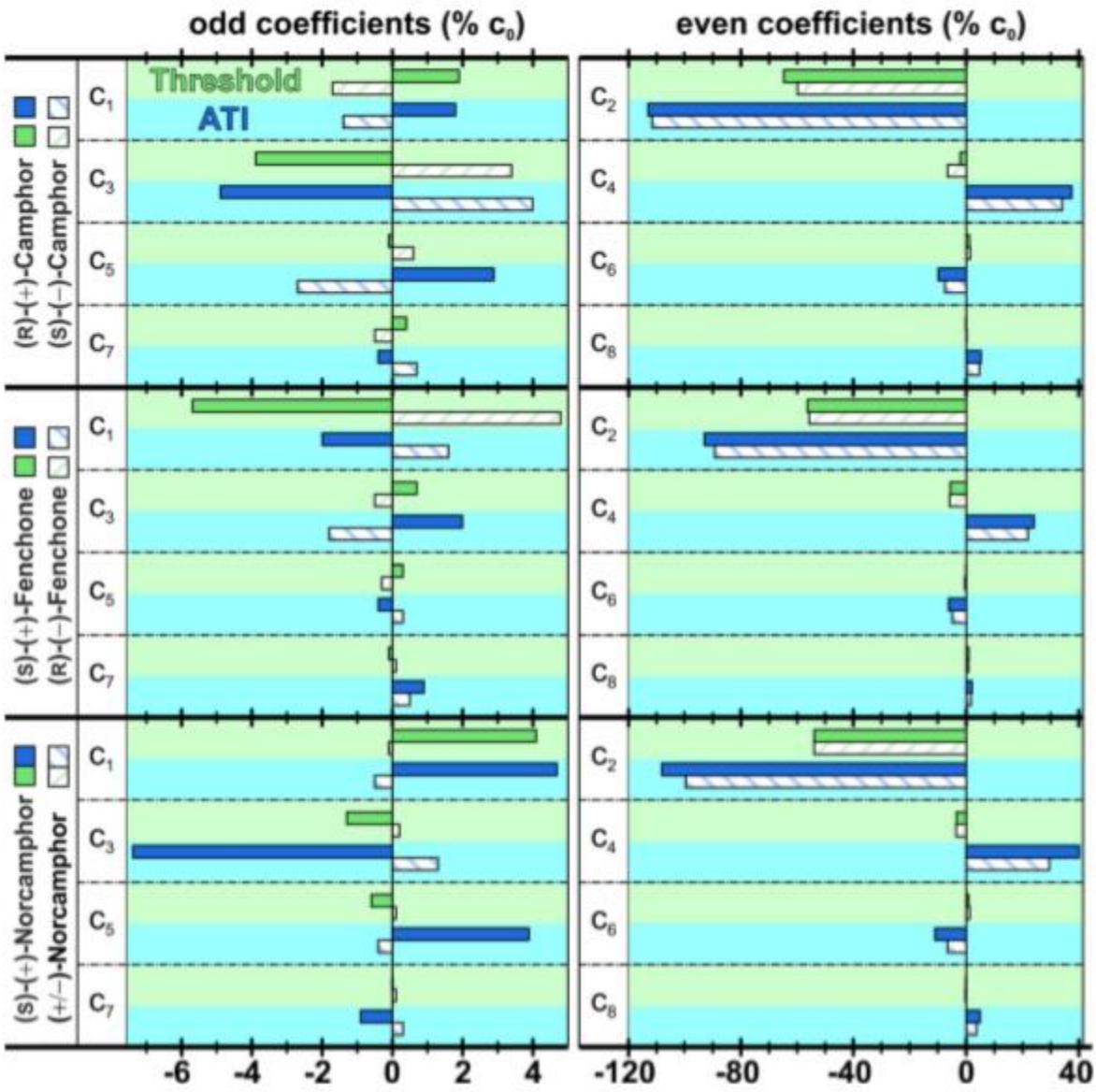

Figure 40. Legendre coefficients for camphor, fenchone and norcamphor for threshold ionization and ATI. [38]

Rafiee Fanood et al. in 2015 probed the PECD effect of limonene using 420 nm 150 femtosecond laser pulses.[41] A single detector spectrometer was used equipped with VMI charge particle optics to record ions and electrons. The authors also recorded the ToF mass spectrum and concluded that the ionization of limonene required three 420 nm photons. The ejected electrons had a kinetic energy of 0.34 eV. For the two enantiomers of limonene the electrons released to the forward (F) and backward (B) hemisphere were recorded.

The PECD effect was expressed as:

$$G = 4\left(\frac{F-G}{F+G}\right) \text{ (Eq. 14)}$$

The MP-PECD is shown in Figure 41 as a function of the electron kinetic energy. At low energies the magnitude of the MP-PECD peaks and as the kinetic energy rises, it reduces. As expected, the results for R-enantiomer have the opposite sign from those for S-limonene.

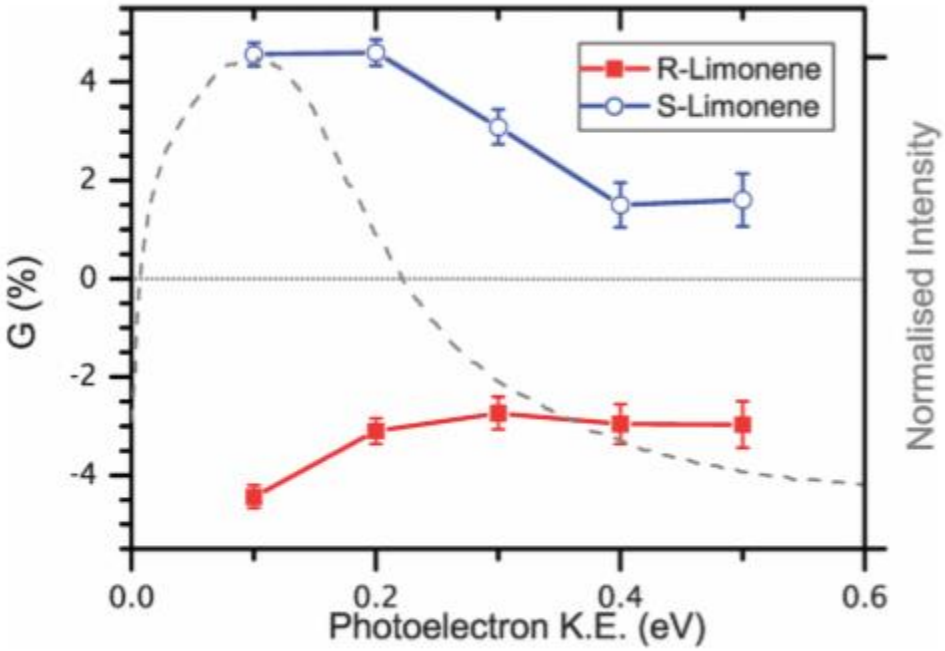

Figure 41. MP-PECD of limonene at 420 nm.[41]

For low energies between 0.0 eV to 0.2 eV the asymmetry factor G has a value of -0.044±0.002 for the R-enantiomer and +0.046±0.002 for the S-enantiomer, magnitudes 30 times larger than the corresponding asymmetries found earlier with absorption and ionization methods.

The authors conclude that since the MP-PECD of limonene gave large asymmetry factors, the identification of enantiomers can be better in means of sensitivity with laser ionization mass spectrometry.

Many studies on PECD concentrated on the dependence of PECD on the molecular structure and the electronic states. Kastner et al. in 2017 experimentally showed that PECD depends on the intermediate state, too.[42] They used fenchone as their molecular sample. The laser pulses had duration of 25 fs. Different excitation wavelengths were used (375-420 nm), in order for different intermediate states to be accessible. They observed 2+1 REMPI.

First, the authors compared previous single-photon absorption measurements on bicyclic ketones at room temperature with their 2+1 REMPI results. The curve of 2+1 REMPI has similar trend with the curve for single-photon ionization but in extent it reveals more information on the intermediate states. The authors attributed the peaks starting at 5.95 eV to the 3s state and those starting at 6.37 eV mainly to the 3p state.

Two definitions were used in order to describe PECD: LPCED and QPECD. The linear PECD (LPECD)[43] values were obtained by weighting the odd order coefficients and linearly summing them. The quadratic PECD (QPECD) is a useful definition to avoid cancellations of individual contributions of Legendre coefficients and can be described as:

$$QPECD = \frac{\sqrt{12}}{c_0}\sqrt{\frac{1}{3}c_1^2 + \frac{1}{7}c_3^2 + \frac{1}{11}c_5^2 + \frac{1}{15}c_7^2} \quad \text{(Eq. 15)}$$

In Figure 42 the antisymmetric part of the PECD, the corresponding profiles of the total signal c_0 and the weighted PECD metric c_0*LPECD are shown. On the top row the top half of each image is the raw PECD and the other half is a cut through the inverse Abel transformation. At the lower panel at top of each figure is the profile of the total signal and at the bottom of each image is the weighted PECD.

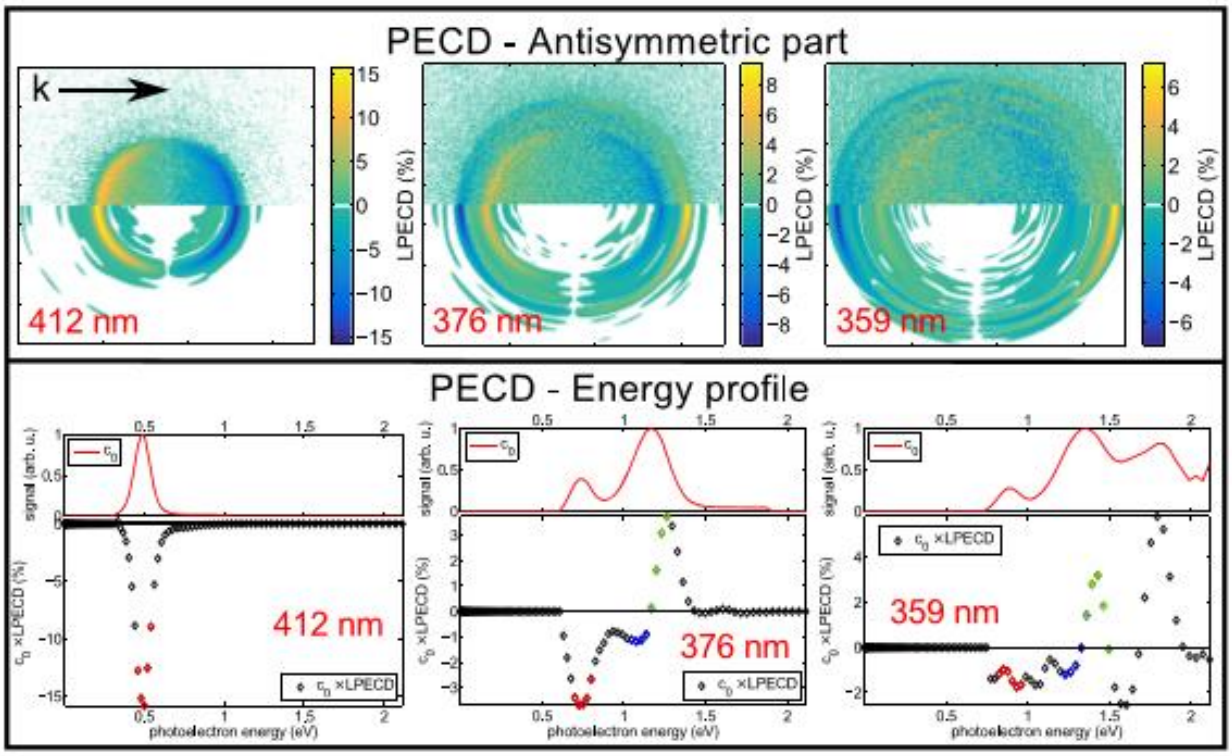

Figure 42. Antisymmetric part of the PECD (raw and after Abel transformation), the corresponding profiles of the total signal c0 and the weighted PECD metric c0*LPECD.[42]

The different contributions in the energy profiles arise from excitation to the B band ($3s \leftarrow n$) at 412 nm, B- and C- band ($3p \leftarrow n$) at 378 nm and B-, C- and $\pi^* \leftarrow \sigma$ at 359 nm.

The LPECD curve underneath the c_0 peak of the $3p \leftarrow n$ state has two contributions with opposite sign, which were identified by fitting two Gaussians onto the c_0 spectrum. These were indicated as $3p_1$ and $3p_2$ were attributed to different electronic excitations in the C-band.

In Figure 43 the authors plotted the LPECD (open diamonds), QPECD (filled diamonds) asymmetries as function of the electron kinetic energy and the results of single-photon LPECD due to ionization of the HOMO of fenchone. The first two show similar behavior. The results for single-photon ionization are alike the other two for energies close to the threshold ionization.

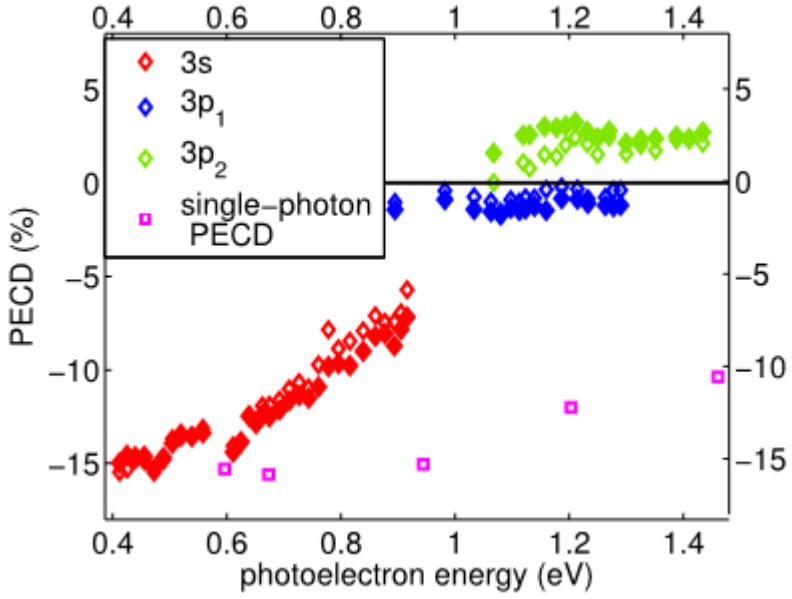

Figure 43. LPECD, QPECD and single-ionization LPECD for different intermediate states as functions of the electron kinetic energy.[42]

For intermediate state 3s the slope is different comparing to the one of the line corresponding to single-ionization. The mean PECD magnitude were found about -13% in the 0.5-0.6 eV region.

The preferred ejection directions of electrons emitted by ionization via the $3p_1$ and 3s are the same. However, the PECD effect due to the $3p_1$ state has smaller magnitude that the one due to the 3s state. Therefore, PECD shows distinct magnitudes for electrons ejected with the same kinetic energy. Moreover, between the two contributions $3p_1$ and $3p_2$ there is an inversion of the forward-backward asymmetry. The authors concluded that the intermediate resonance influences PECD.

Another experiment concentrated on the dependence of PECD on the molecular structure, was the one carried by Beaulieu et al in 2018.[44] The photoionization of the (+)-limonene enantiomer with two-color laser fields with different polarization combinations, confirmed that the bound-bound transitions do not need to be driven with circularly polarized light in order for PECD to be observed.

Most studies on PECD described here used the linear combination of Legendre polynomials to present and analyze their results. Miles et al. introduced a new stereo detection set up that made possible probing PECD without Legendre polynomials.[45] Their experimental set up is shown in Figure 44.

Femtosecond laser pulses (250 fs, 394 nm) were focused into the interaction region which is between two grounded rectangular plates. A magnetic field of 30-40 gauss was applied along the light propagation. The ejected electrons spiral along the field lines either parallel or anti-parallel to the laser direction depending on the emission angle. If the angle is larger than 90°, then the electrons spiral anti-parallel to the light propagation. As soon as the electrons exit the interaction region they accelerate into deflection plates. The purpose of the deflection plates was to direct the electron to channel electron multipliers.

One main difference that this set up has in comparison with others, is that all electrons are collected independent of their initial energy or angle. The authors used this experimental set up and for experiments on camphor and fenchone.

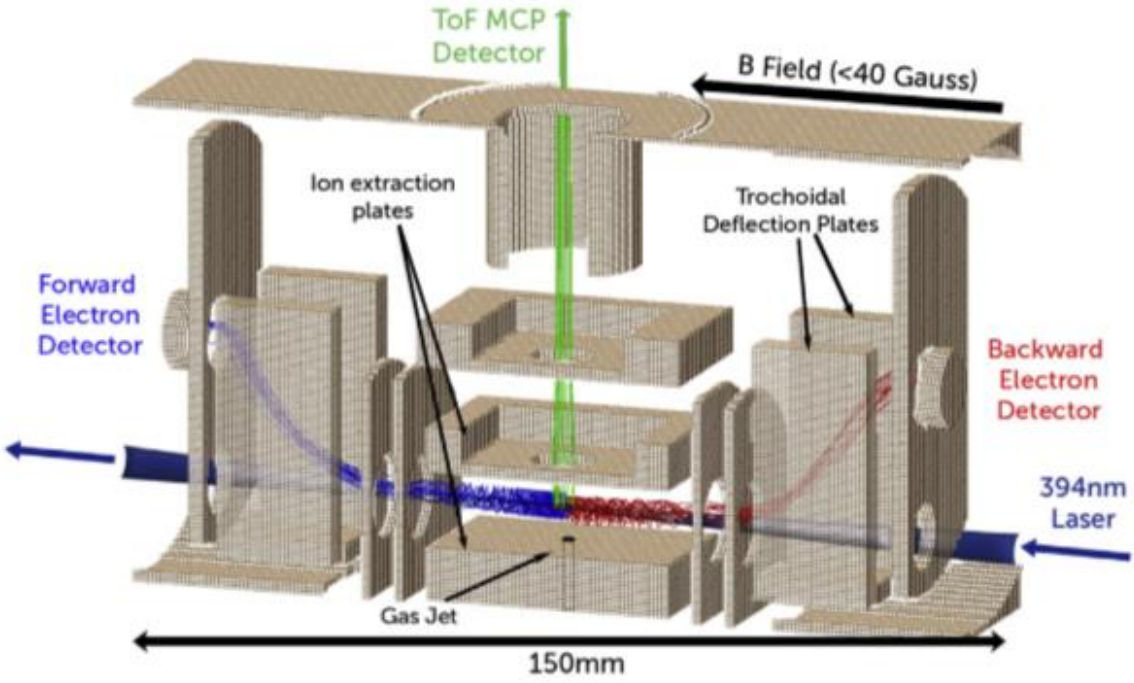

Figure 44. The new stereo detection Miles et al. introduced.[45]

The following parameter was used in order to describe the PECD asymmetries:

$$G = \frac{F_L - F_R}{(F_L + F_R)/2} - \frac{B_L - B_R}{(B_L + B_R)/2} \text{ (Eq. 16)}$$

Where F is the forward emission (0° to 90° to the laser propagation) and B is the backward emission (90° to 180°) obtained from the integrated electron yields. L stands for left polarization and R for right.

The authors calculated the G factors for camphor and fenchone and compared their results with those found in previous experiments using the VMI technique. Their comparison showed great agreement. They found an enantiomeric excess of 66±5% of R-fenchone.

Furthermore, they plotted the parameter G as a function of the enantiomer excess and found a linearly dependence. In order to determine the relation between G and polarization degree, the authors plotted G for the (2+1)-REMPI ionization of S-camphor for different degrees of polarization as a function of the magnitude of the Stokes S_3 parameter. S_3 is a parameter that represents the difference in the intensity of LCP and RCP. Their results are shown in Figure 45.

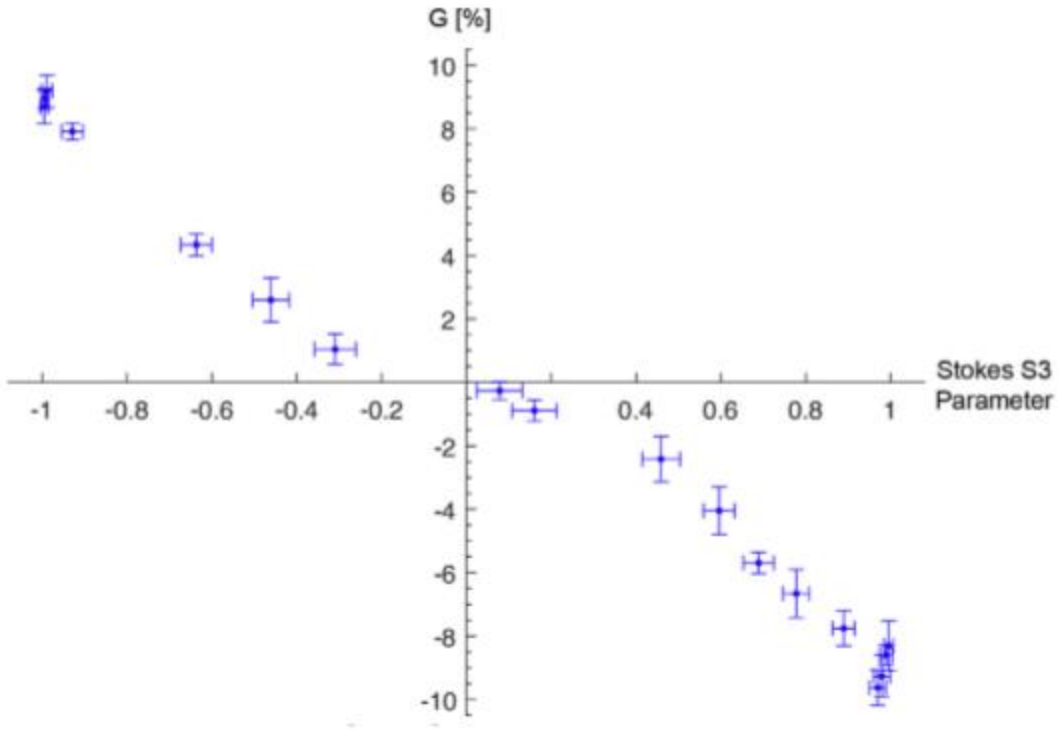

Figure 45. G as a function of the Stokes S3 parameter for S-camphor and for different degree of circular polarization.[45]

A linear dependence was expected, however in figure 40 it seems that for |S3| > 0.4 G increases more rapidly. This nonlinearity may occur due to selective excitation of certain molecular orientations in the ensemble.

Powis et al. probed with 30 fs pulses at 396.52 nm, 371.02 nm and 200.66nm the MP-PECD of R-α-pinene.[46] The raw VMI images they obtained were processed with the pBasex algorithm to claim the Legendre polynomials parameters and the angle integrated PES. Figure 46 and Figure 47 show the VMI-PES and PECD coefficients of the sample at 396.52 nm and 200.66 nm, respectively. The PECD asymmetries are up to 10%.

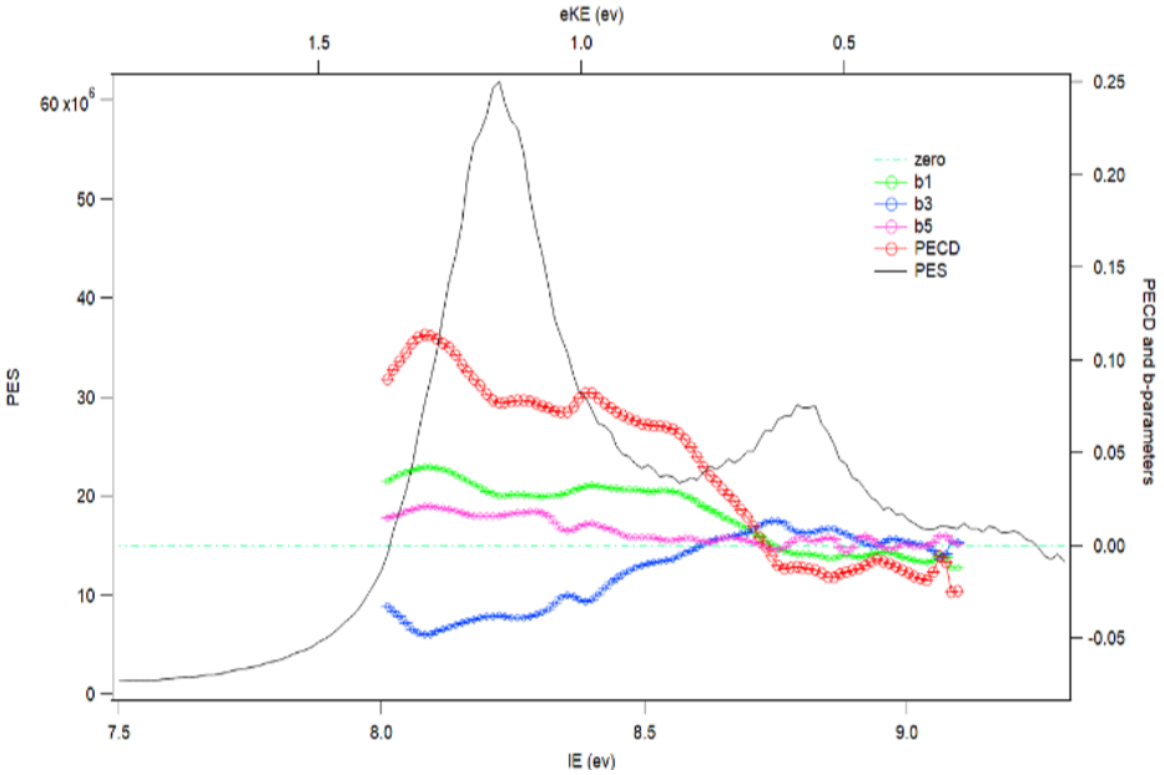

Figure 46. VMI-PES, PECD coefficients of R-α-pinene at 396.52 nm.[46]

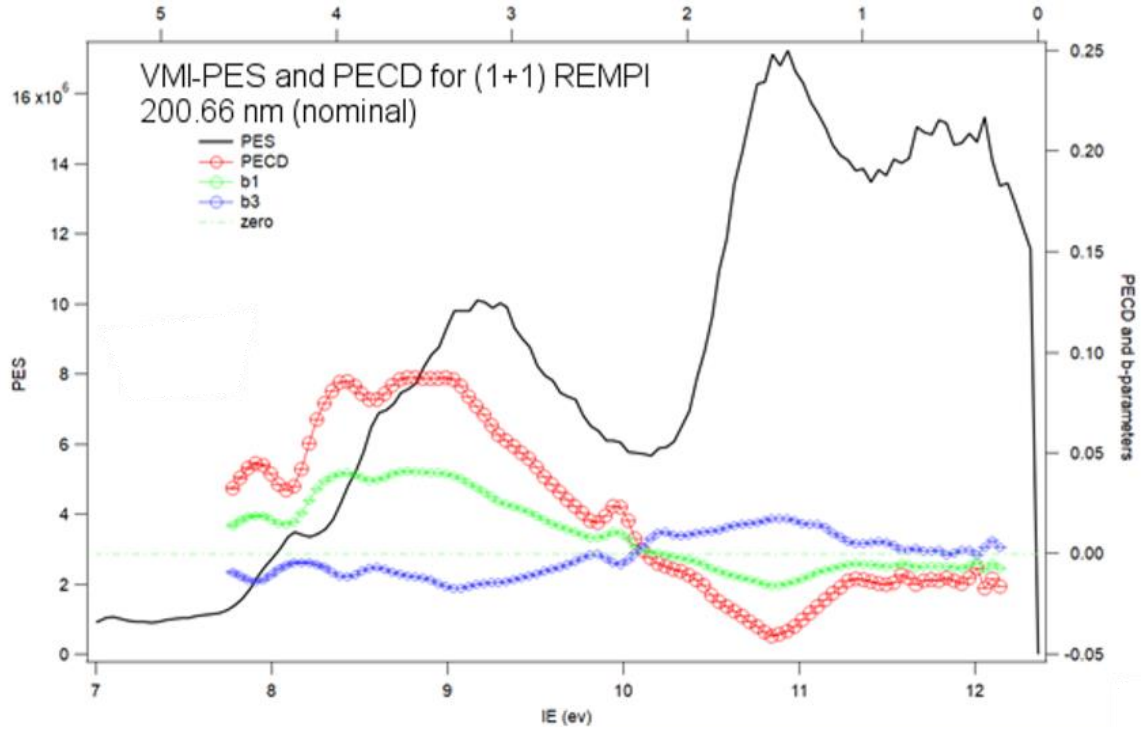

Figure 47. VMI-PES and PECD results of R-α-pinene at 200.66 nm.[46]The terms b_3 and b_5 are non-zero only in 3-photon ionization, however they should not be of larger magnitude of b_1. In this experiment, the coefficient b_3 is greater than b_1, suggesting a contribution to the asymmetry due to optical pumping to the resonant intermediate state.

In 2019, Greenwood and Bond used the stereo-detection setup introduced by Miles et al. in 2017 in order to probe PECD for the aromatic molecule (R)-phenylethanol with femtosecond laser pulses at 260 nm and duration 300 fs.[47] The nonlinear dependence found in reference [34] between the G factor and the Stokes parameter S3, suggests that molecular orientation is a big factor in measuring PECD.

The excitation or absorption of light can be viewed as the phenomenon where the electric (or magnetic) field pushes the electron density from one state to another with higher energy lever or to the continuum. The direction of the net linear displacement of charge is called polarization of transition. The polarization and the intensity can be described by the transition moment.

It has a well-defined direction within a molecule and length. It can be seen as the antenna by which the molecule absorbs light.[5] The maximum probability of absorbing light is achieved when the transition moment is aligned along the electric field oscillation plane. In this experiment the relation between G and S3 for the (1+1)-REMPI ionization of (R)-phenylethanon was found linear, as shown in Figure 48.

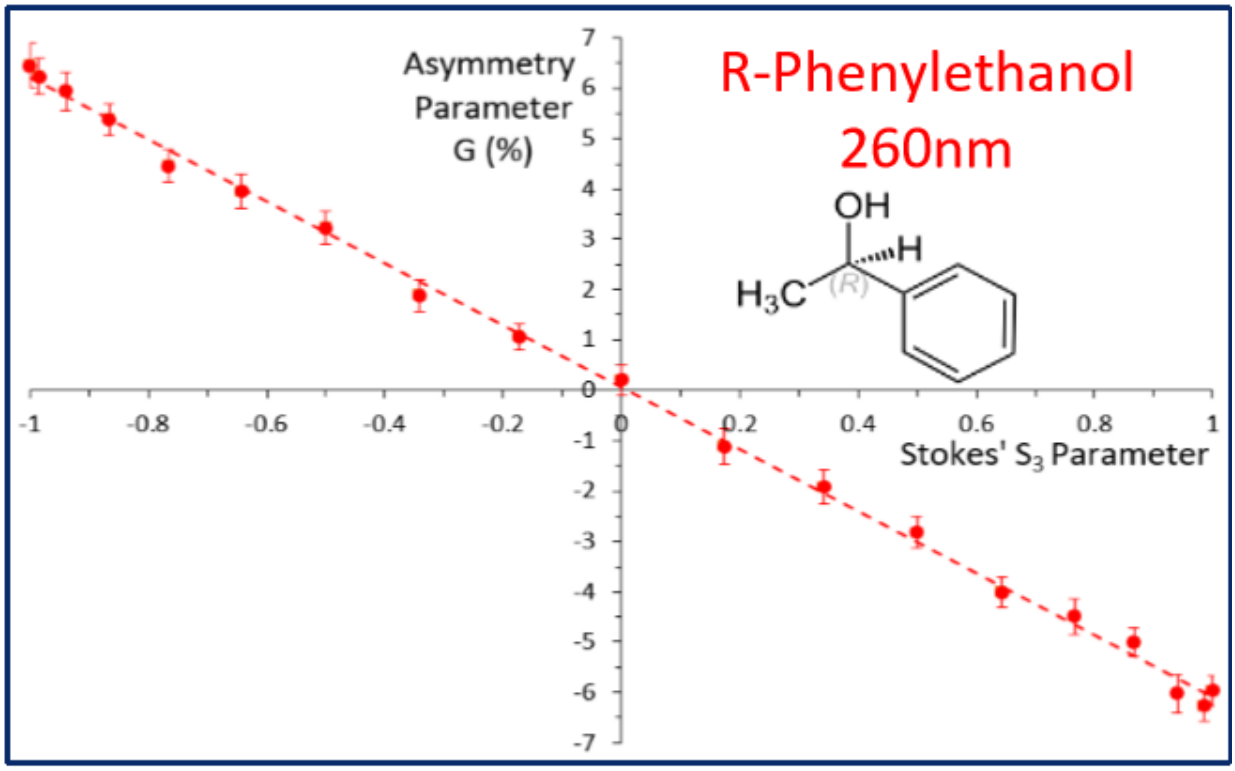

Figure 48. The G factor as a function of Stoke's parameter S3 for (R)-phenylethanol.[47]

The linear dependance of the G parameter on the Stoke's parameter suggests that molecules with specific orientation are not preferred in terms of excitation from other molecules.

However, the authors mention that the process of (1-1)-REMPI is simpler than the one of (2+1)-REMPI in reference [34] and therefore the excitation step in this experiment may not depend much on the molecular orientation.

The same year Fehre et al. investigated the link between PECD and fragmentation channel in the strong field regime.[48] In the strong field regime the laser fields are very intense compared to the molecular (or atomic) potential. The potential is significantly distorted and perturbative calculations are not valid.[49] The molecule used as sample was methyloxirane (MOX). The pulses had 40 fs duration and central wavelength 800 nm and $6.9 \times 10^{13}\, W/cm^2$ intensity. The coincident detection of fragment ions and the electron momentum vector was achieved with symmetric cold target recoil ion momentum spectroscopy (COLTRIMS).

If p_{ex} is the electron momentum parallel to the laser propagation and $p_{et} = \sqrt{{p_{ey}}^2 + {p_{ez}}^2}$ is transversal momentum in the plane of polarization, then PECD can be described as:

$$PECD(p_{ex}, p_{et}) = 0.5\,\frac{R_{LCP}(p_{ex},p_{et}) - S_{LCP}(p_{ex},p_{et})}{R_{LCP}(p_{ex},p_{et}) + S_{LCP}(p_{ex},p_{et})} - 0.5\,\frac{R_{RCP}(p_{ex},p_{et}) - S_{RCP}(p_{ex},p_{et})}{R_{RCP}(p_{ex},p_{et}) + S_{RCP}(p_{ex},p_{et})} \quad \text{(Eq. 17)}$$

$R_{LCP}(p_{ex}, p_{et})$ is the number of counts with LCP light and R-MOX and $S_{RCP}(p_{ex}, p_{et})$ the corresponding number of counts with RCP light and S-MOX.

The TOF spectrum was measured in coincidence with the photoelectron and is shown in Figure 49 with the corresponding PECD asymmetries of each fragment region.

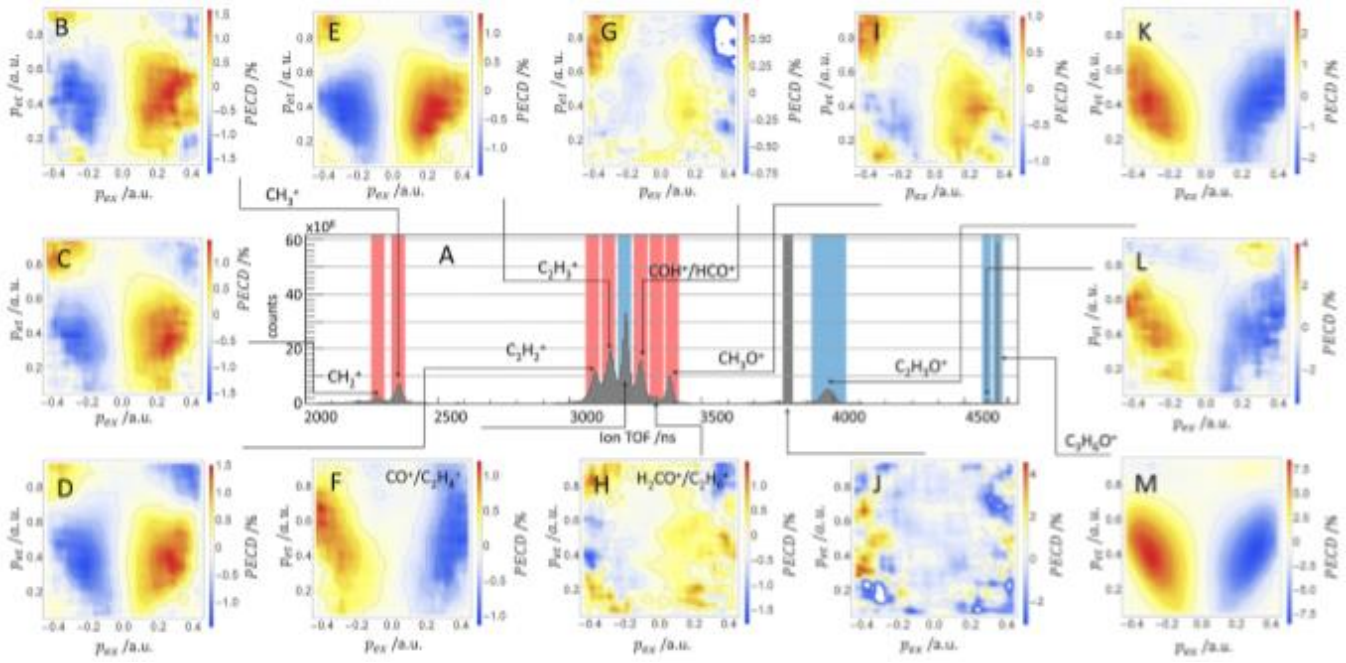

Figure 49. Time of flight spectrum and PECD asymmetries for methyloxirane.[48]

The arrows in Figure 49 connect the fragment region with the associated PECD asymmetries. The blue color in the TOF spectrum represents the negative slope of PECD, and the red color the positive PECD slope. There is strong dependence of PECD on the p_{et} and is different for different fragment channels. The authors considered dependence of PECD on the ionized molecular orbital and molecular orientation with respect to the polarization plane and concluded that selecting a fragment ion channel selects a molecular subsample of specific orientation in space. Thus, PECD is that of oriented molecules and depends on the fragment channel.

1.5 Nanosecond work

In 2019 Kastner et al. investigated fenchone with nanosecond laser pulses (25 ns) for the first time.[50] A third harmonic (355 nm) of an ND:YAG laser was used and the polarization of the light was being changed with a quarter wave plate. The VMI images were analyzed by expansion into Legendre polynomials and the odd-order coefficients were weighted and linearly summed to obtain a PECD metric characterized by only one number (LPECD). The LPECD values were found similar for nanosecond and femtosecond laser. Three intermediate states were accessed.

As shown in a previous fs experiment (see reference 42) 2-hv absorption in this region accesses three intermediate electronic states: at longer wavelengths between 359 nm and 431 nm only ionization via the 3s intermediate state is visible in the PES. The 3p state appears in addition for wavelength below 393 nm. Below 363 nm the third intermediate state appears corresponding to a $\pi^* \leftarrow \sigma$ excitation.

The PES using nanosecond pulses and femtosecond pulses of the S enantiomer are shown in Figure 50. The PES with femtosecond laser pulses was taken from reference [43]. The main differences of the two PESs are the relative heights of each contribution. Considering the peaks obtained with nanosecond laser pulses, the shorter lifetime of the 3p intermediate state compared to the 3s reduces its relative contribution to the PES.

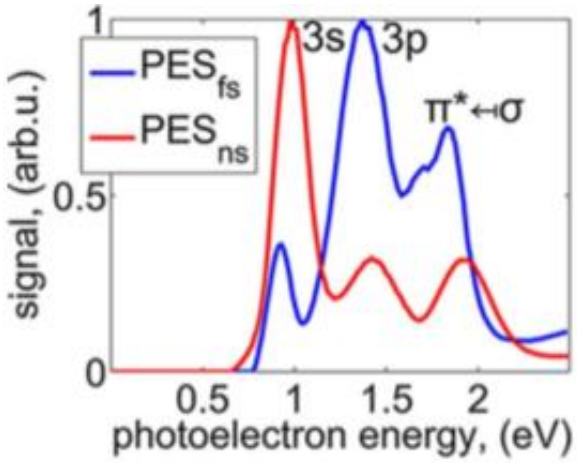

Figure 50. PES with femtosecond and nanosecond pulses.[50]

In Figure 51 the anti-symmetrized PECD image for (S)-(+)-fenchone and (R)-(-)-fenchone are shown. The upper half of each image shows the raw results and the lower half shows the derived contribution of the odd-order Legendre polynomials. The light propagation is from left to right. The LPECD values are obtained from the equation below:

$$LPECD = \frac{1}{c_0}(2c_1 - \frac{1}{2}c_3 + \frac{1}{4}c_5) \text{ (Eq. 18)}$$

As c_i are defined the odd Legendre polynomial coefficients, with i=0 for the total signal.

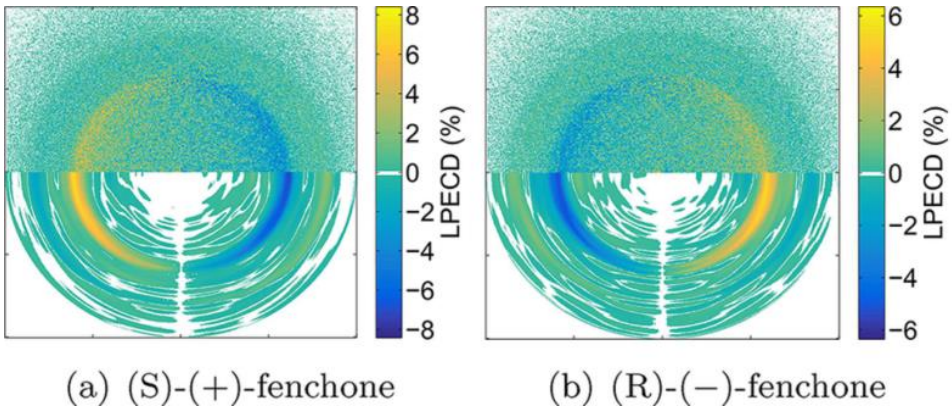

Figure 51. PECD images for (S)-(+)-fenchone and (R)-(-)-fenchone with the linear sum of the odd-order coefficients (LPECD).[50]

The authors then compared the LPECD values obtained in this experiment with those of reference [43] and found agreement in sign and magnitude for the $\pi^* \leftarrow \sigma$ contribution. The value for the 3p state has the same sign as the 3p1 in the femtosecond experiment. Furthermore, the authors point out that in the femtosecond case the LPECD value for the 3p2 state is higher and has opposite sign to the 3p1. This suggests that during the excitation of the 3p manifold

several intra-molecular dynamics are launched. The authors mention that further experimental and theoretical investigations are necessary.

In 2020 Kasnter et al. recorded wavelength-dependent PECD signal in the REMPI spectrum (375-420 nm) of fenchone with nanosecond lasers.[51] The REMPI spectrum was recorded with linearly polarized light. The authors also obtained the wave-dependent PES of (S)-(+)-fenchone by Abel-inversion of the LIN PADs.

In this experiment Rydberg intermediate states were involved. Rydberg states of molecules (and atoms) are very slightly bound quantum states of an electron and a positively charged ion.[52] In atoms the Rydberg states can be described as those states in which one electron is excited to an atomic orbital relatively large in size compared to a typical singly-charged "core".[53] This description can be extended to molecules, too. Rydberg states have greater principle quantum number (n) than the valence state. For organic systems, that means n>2.

They extracted the LPECD values[43] (equation 19) of (S)-(+)-fenchone after 2+1 REMPI via the 3s and 3p Rydberg states with nanosecond laser pulses of 25 ns. At 416.57 nm the density of the vibrational states is low, thus the 3s eigenstate is excited. At 380.2 nm both states the 3s and 3p are excited.

Sample results are shown in Figure 52. The LPECD values were found larger in magnitude that those recorded previously with femtosecond laser pulses. The authors mentioned that the recording of the values in this experiment were performed with a pulsed molecular beam, whereas those of the experiment in comparison were recorded by an effusive beam source. Thus, the vibrational excitation was greater in the experiment with femtosecond pulses and the comparison cannot be considered accurate.

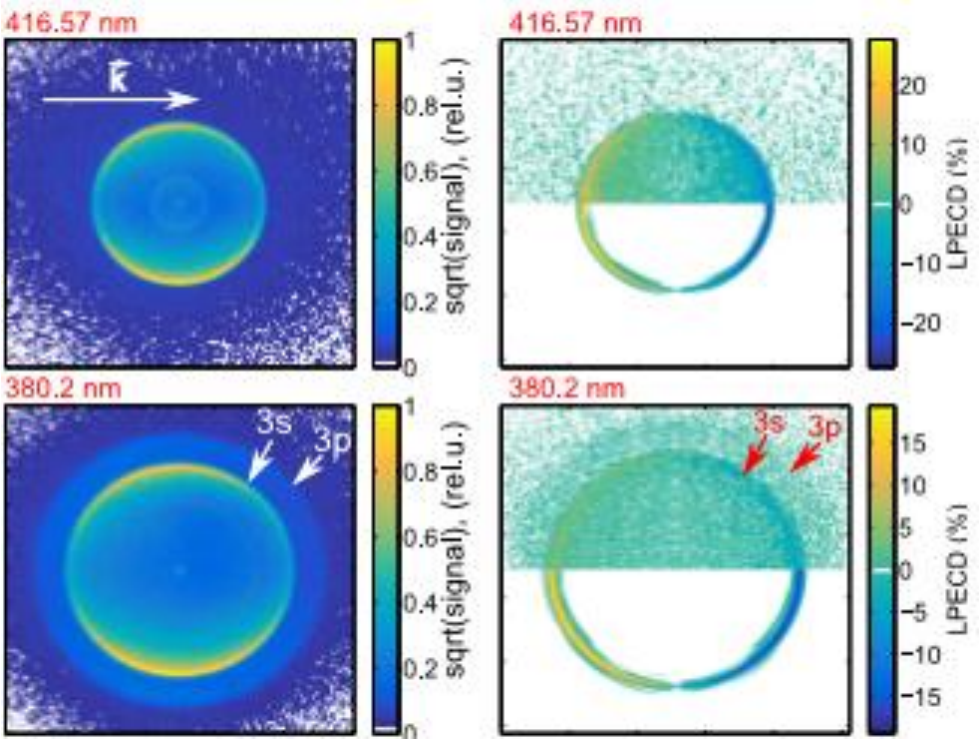

Figure 52. VMI images for the 2+1 REMPI ionization of (S)-(-)-fenchone. The left row shows the results with LIN and the right row the antisymmetrized PECD images.[51]

Within the experimental error of ±3%, the LPECD values of both enantiomers have same magnitude and opposite sign. Moreover, features in the LPECD that correspond to vibrational bands were not found and the authors concluded that the vibrational energy of the intermediate 3s state does not influence the LPECD values for the 2+1 REMPI of fenchone.

1.6 Computational MPECD and PECD theoretical work

In this section we discuss theoretical work related to PECD.

One year before the first experiment on PECD, in 2000 Ivan Powis was the first one to introduce quantitative calculations of PECD for randomly oriented molecules.[54] Considering the molecule $C_3H_6O_3$ which has two enantiomers, lactic acid and glyceraldehyde, Powis used computational methods with electron-ion scattering calculations to find the electric dipole matrix elements and examined the relation between the electron anisotropy and the geometric conformation considering a low-lying H-bonded isomer of glyceraldehyde.

First, he expressed the differential cross section for electron emission and then wrote the corresponding full matrix element M_p in the lab frame, squared it and integrated over all molecular orientations, R. The result is a sum in Legendre polynomials:

$$\int (M_p)^2 dR = \sum_j \overline{b_j^p}\, P_j cos\theta \text{ (Eq.19)}$$

With p the polarization and θ the lab-frame polar angle. The differential cross section can be written as:

$$\frac{d\sigma}{d\Omega} = \frac{\sigma}{4\pi} I_p(\theta) \text{ (Eq. 20)}$$

with $I_p(\theta) = [1 + b_1^p P_1 cos\theta + b_2^p P_2 cos\theta]$ the angular distribution function for single-ionization

For linearly polarized light $b_1^0 = 0$ and:

$$b_2^{\pm 1} = -\frac{1}{2} b_2^0 \text{ and } b_1^{+1} = -b_1^{-1} \text{ (Eq.21)}$$

Circular dichroism in the angular distribution can be written as the difference in the angular distribution functions for right and left circularly polarized light and the result is as equation 3.

Powis used the CMS-Xα method[55,56] to calculate the matrix elements necessary for the computation of the Legendre coefficients and used an outer-valence Green's function (OVGF) method to calculate the ionization potential, as experimental data did not exist at the time. He later found the structures of the most stable conformers of the enantiomers, and symbolized them for simplicity the numbers (1), (2) for the glyceraldehyde and (3) for the lactic acid. He also plotted the integrated cross section, eigenphase sum and Legendre coefficients as functions of the kinetic energy of the ejected electrons for the ionization of the outermost orbital of D-glyceraldehyde for each conformer.

The magnitude of the b_1^{+1} parameter is comparable to the one of b_2^{+1}, confirming previous predictions that the orientation term b_1^p arising from pure electric dipole interferences contributes to the differential cross section and suggesting that it is possible to observe PECD in randomly oriented chiral molecules.

Figure 53 shows the photoelectron angular distributions (PADs) and CDAD for angles between 0° and 360° and for kinetic energies from 0 eV to 20 eV for the (1) conformer of D-glyceraldehyde. The left column is the results with LCP, the middle column with RCP light and the right column is the CDAD. The numbers in each row show the orbital of ionization.

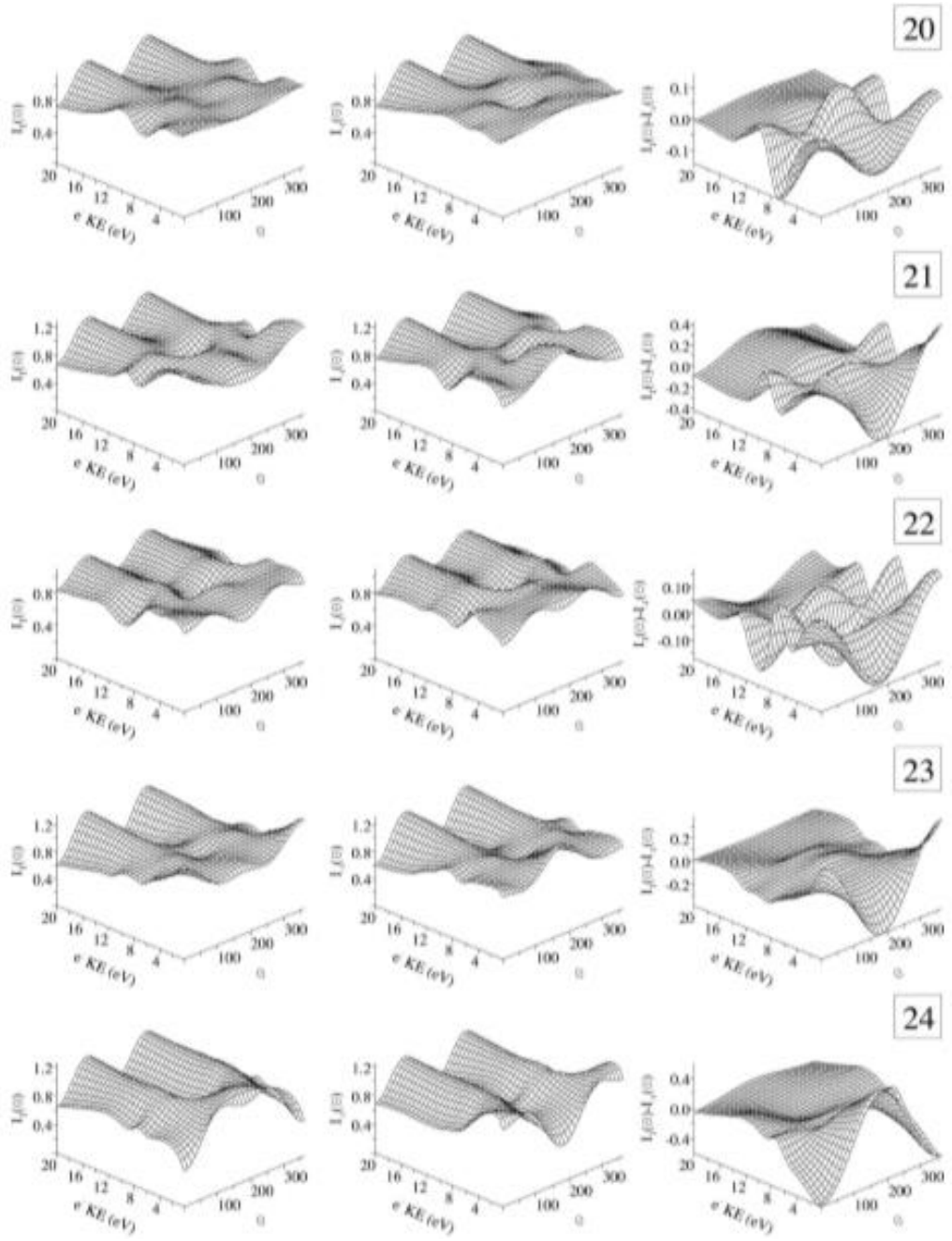

Figure 53. PADs for the (1) conformer for LCP light (left column), RCP light (middle column) and their difference, CDAD (right column) as a function of the kinetic energy and the angle with respect to the light propagation.[13]

At low kinetic energies the results with LCP and RCP light are similar. The angular distributions peak at 90° and 270°, as the $b_2^{\pm 1}$ coefficients move towards the classical limit of -1 and the $b_1^{\pm 1}$ parameters towards zero.

Calculations were performed for the other conformers, too. The CDAD is sensitive only to the coefficients $b_1^{\pm 1}$. Powis showed that it is possible to identify enantiomers via PECD and calculated the ratio of the likely experimental sensitivity (CDAD asymmetries). The ratio was

found for the (1) conformer around 20% with a maximum at 40% at some cases and for the (3) conformer between 10% and 35%.

Artemyev et al. in 2015 theoretically studied the angle-resolved multiphoton ionization of polyatomic molecules, tested their theory with one and two-photon ionization of a model methan-like system with short high-frequency pulses and analyzed PECD in the momentum distribution.[57]

The authors' theoretical study is based on the TDSC method. The authors wrote the time dependent Schrödinger equation for one electron in an effective potential and an electric field created by the laser. Then, they expressed the one-particle wave function and the effective potential as expansions by spherical harmonics, rewrote the Schrödinger equation and projected the results into spherical harmonics. They determined the initial and final electronic state, computed the final electron momentum distribution $\Psi(\vec{k}) = \int \Psi(\vec{r}) e^{-i\vec{k}\cdot\vec{r}}$ and expressed the 3D photoemission probability in terms of spherical harmonics. The numerical approach to solve the time-dependent Schrödinger equation was taken from the finite-element discrete-variable representation (FEDVR) basis set.

To see if the TDSC method is accurate, the authors tested one and two-photon ionization of the chiral model shown in Figure 54. The third bound state of the molecule was ionized with Gaussian-shaped laser pulses. The carrier frequency was of 22.1 eV and the pulse duration 1 fs.

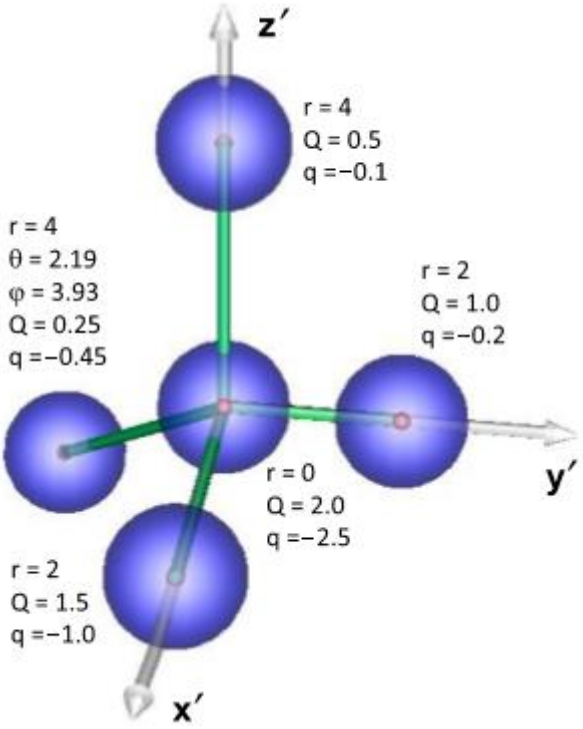

Figure 54. Methane-like chiral molecule. The red dots are the charges Q and the blue clouds are the electron densities with total charges q.[57]

The test was performed for different molecule orientations in the molecular frame with respect to the lab frame. The orientations are given by the three rotational Euler angles α, β, γ and the initial one in for $\alpha = \beta = \gamma = 0$. The PECD integrated over the angle α and as a function of the β, γ angles is shown in Figure 55.

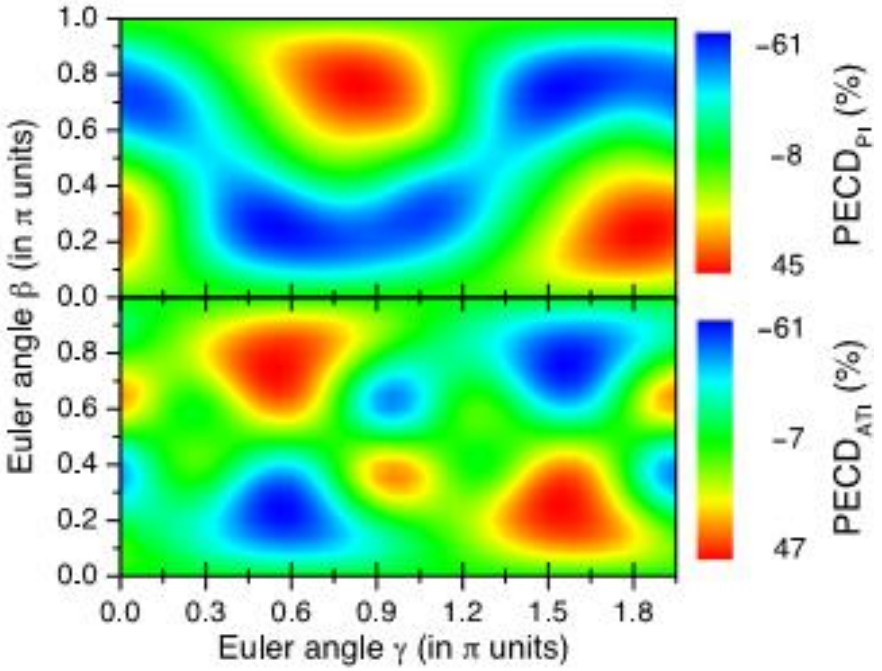

Figure 55. PECD for a methan-like model as a function of the Euler angles β,γ.[57]

The upper panel in Figure 55 corresponds to the first peak of the electron spectrum taken for initial orientation $\alpha = \beta = \gamma = 0$ and with circular polarized Gaussian-shaped pulses ionizing the initial state. The first peak is one-photon ionization (PI).

The lower panel in Figure 55 corresponds to the second peak of the spectrum and is a two-photon ATI. The electron spectrum is shown in Figure 56.

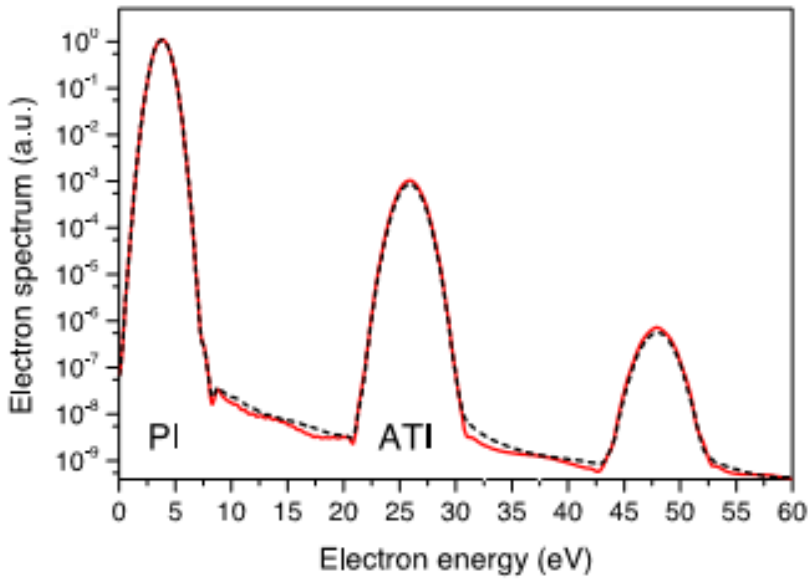

Figure 56. Electron spectrum for the initial molecular orientation with circular polarized light Gaussian-shaped pulses.[57]

The red solid line corresponds to LCP light and the dashed black line to RCP light. The PECD asymmetries in Figure 55 are up to 60% for some molecular orientations.

Muller et al. extended the theoretical investigation studying the three- and four-photon ionization of fenchone and camphor with the same computational method.[58] They computed the PECD asymmetries in the momentum space $(k_{||}, k_{\perp})$ of randomly oriented molecules of fenchone and camphor for wavelengths 400 nm, 380 nm and 360 nm and compared them with the current experimental data. The light propagates from left to right (z-axis in the laboratory frame) and coincides with the $k_{||}$ axis. The pulse duration was about 10 fs FWHM and the emission angle θ was measured with respect to the $k_{||}$ axis. The results for ionization with 400 nm of (R)-(-)-fenchone are shown in Figure 57.

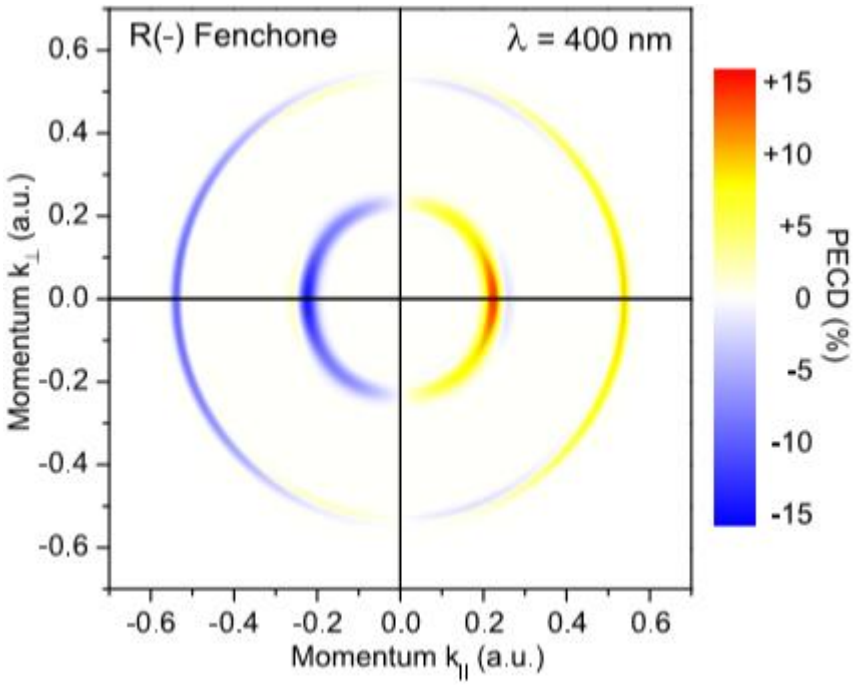

Figure 57. computed PECD in the momentum space for multiphoton ionization of (R)-(-)-fenchone with 400 nm pulses.[58]

The results depicted in Figure 57 are shown in percent of the maximal intensity of each spectrum (outer ring and inner ring). The inner ring corresponds to PI by three photons of energy 3.10 eV and the outer ring corresponds to ATI by four photons. The PECD asymmetries of the PI are of the order of 13% and for the ATI reach the value of 9%. The computed results are in great agreement with several experimental data.

The ionization of R-(-)-fenchone with 380 nm laser pulses are shown in Figure 58. One important feature of Figure 58 is that the PECD asymmetries of the inner ring change sign for shorter wavelength than 388 nm and those for the outer ring do not. The inner ring corresponds to three photon ionization and the outer to four photon ionization.

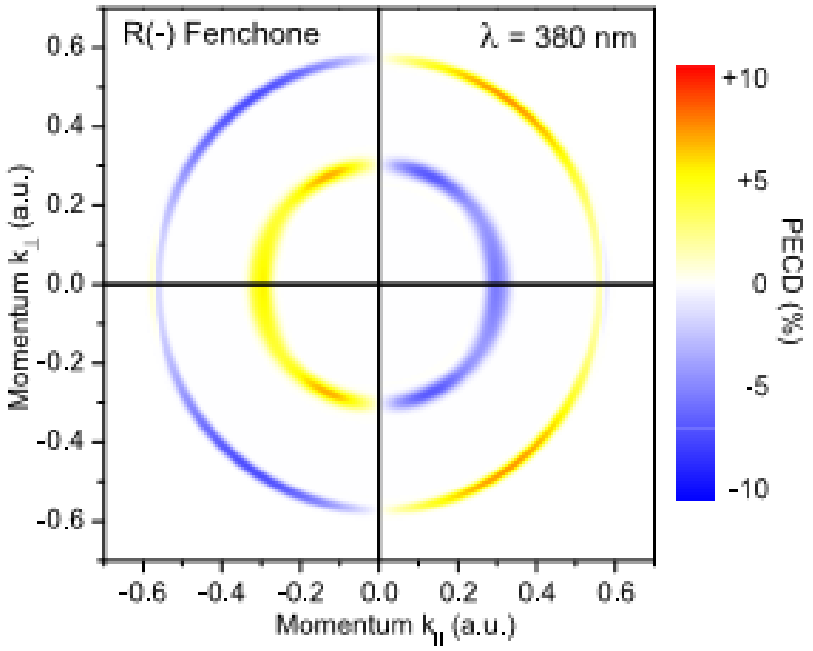

Figure 58. Computed PECD in the momentum space of (R)-(-)-fenchone with 380 nm laser pulses.[58]

The authors compared their computed results with the experimental data taken from reference [41] and found agreement is sign but the computed magnitude of PECD was three times larger than the experimental one.

The PECD in the momentum space of R-(+)-camphor for ionization with 360 nm is shown in Figure 59. The inner ring and the outer ring represent three-photon and four-photon ionization, respectively. PECD is of the order of 5% for the inner ring and 9% for the outer one. These asymmetries were found in great agreement with several experimental data.[35,38,43,59]

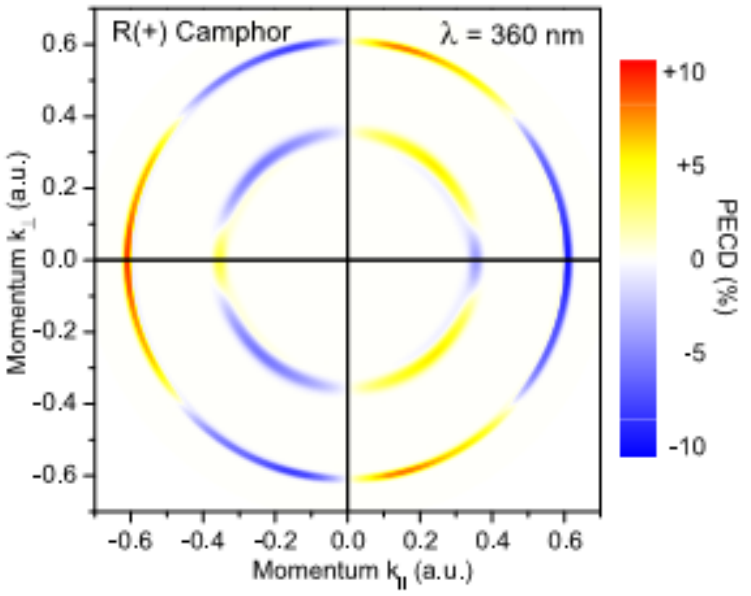

Figure 59. Computed PECD for 360 nm ionization of (R)-(+)-camphor.[58]

The case of uniaxially oriented molecules was investigated, too. The C=O bond of both fenchone and camphor define the z-axis. A PECD of 19.1% was found for the three-photon ionization of fenchone with the C=O bond parallel to the light propagation and -14.9% for the four photon ionization of fenchone with the C=O bond perpendicular to the light propagation. The average over all orientation angles gave a PECD of 4.0%. The corresponding results for the case of camphor were up to 8% for the three photon ionization and up to 33% for the four-photon ionization. The average asymmetry was 7.4%.

In 2020 Muller et al. theoretically probed the PECD asymmetries in the momentum space of fenchone in different regimes of multiphoton ionization, using the same method as in references [57] and [58].[60]

The PI and ATI of fenchone with 400 nm laser pulses of duration 20 fs were first computed. The C=O bond was chosen as the molecular z-axis and the light propagation differs with the orientation Euler angles α and β with steps Δα and Δβ of 0.1 π. The computational results were in agreement with the available experimental data.

Next, the PECD computational results of the PI and ATI of fenchone with 800 nm laser pulses were demonstrated. The carrier frequency of the four-photon ionization was resonant for the absorption of a fifth photon and therefore the authors detuned the wavelength of the pulses to 814 nm. In this case the results were in agreement with the experimental data, too.

The strong-field ionization of fenchone was next in investigation with 1850 nm infrared pulses and an intermediate regime between the multiphoton and the tunnel ionization were considered. In order for the computational errors to be reduced, the steps Δα and Δβ were set at 0.2 π. The

photoelectron spectrum and the corresponding PECD asymmetries in the momentum space are shown in Figure 60.

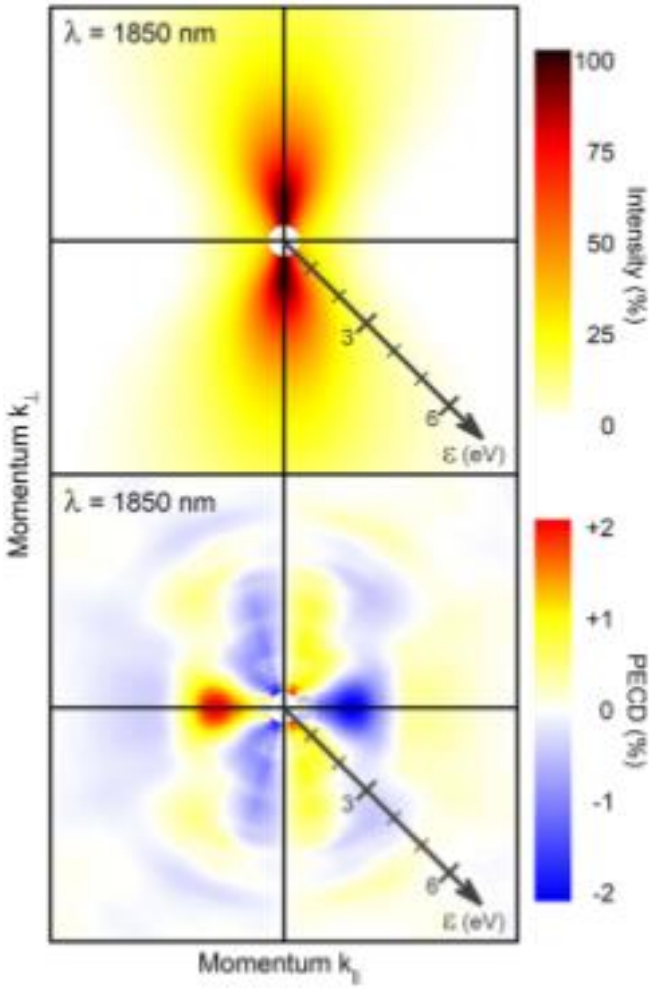

Figure 60. Computed electron spectrum and PECD asymmetries for the strong-field ionization with 185 nm infrared pulses of (R)-(-)-fenchone.[60]

The electron spectrum is considered typical for the tunnel ionization regime and its vertical aligned due to the alignment of photoelectrons with the electric field which rotates in the dipole plane. The PECD asymmetries were up to 2%. The computational PECD changes its sign two times, instead of one like in the experimental data. The inner part of PECD is in agreement with the experimental one.

Next, the broadband ionization of randomly oriented R-(-)-fenchone was investigated. The number of available pathways to ionization was infinite and therefore the transition amplitudes superimposed and interfered.

The time-envelope of the signal is:

$g(t) = \frac{\pi^2}{\pi^2-(\omega_2-\omega_1)^2t^2} cos(\frac{\omega_2-\omega_1}{2}t)$, with $\omega_1 = 1.0\ eV, \omega_2 = 3.0\ eV$ and $\omega_0 = 2.0\ eV$ the carrier frequency.

The steps Δα and Δβ were again 0.2 π to reduce computational errors. The total electron spectrum and the corresponding PECD asymmetries in percent of the maximum in the spectrum are shown in Figure 61.

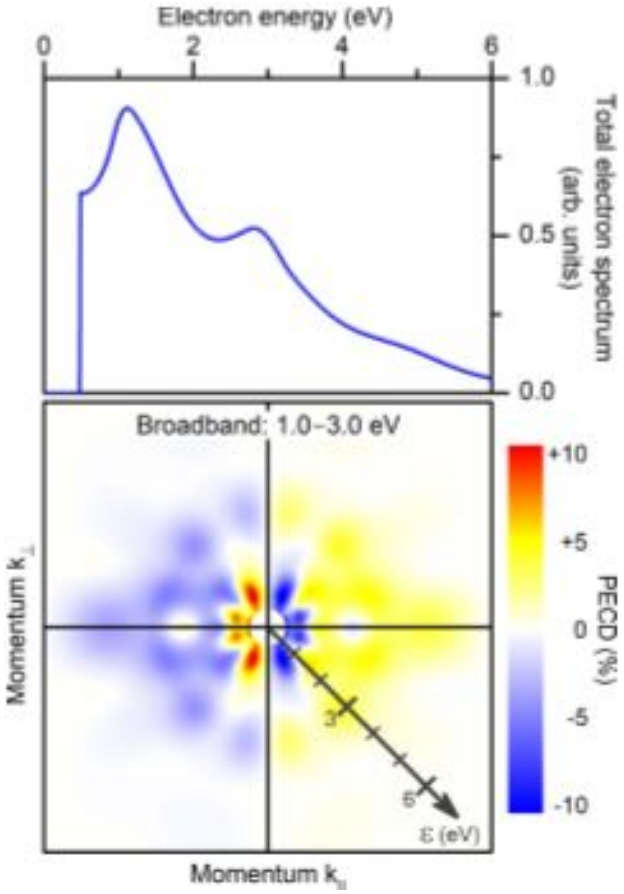

Figure 61. Computational electron spectrum and PECD asymmetries of R-(-)-fenchone with broadband pulses.[60]

In the upper panel, three overlapping peaks (around 1.1 eV, 2.8 eV and 4.6 eV) with decreasing intensity form the electron spectrum are depicted. The corresponding PECD asymmetries are of the order of 10% and change sign around the first maximum of the spectrum. PECD is this case shows an angular structure which is a lead of the interference of multiple pathways.

Last, the authors studied the PECD of R-(-)-fenchone from bichromatic fields. It was the first time multiphoton PECD calculations were made for an existing molecule. PECD of six-red-photon and three-blue-photon ionization was studied with 800 nm and 400 nm pulses respectively with the butterfly field configuration mentioned in references [57] and [41], to maximize the asymmetries. Again, Δα and Δβ were set 0.2 π. The duration of the sinesquared pulses was 22 fs. The results are shown in Figure 62.

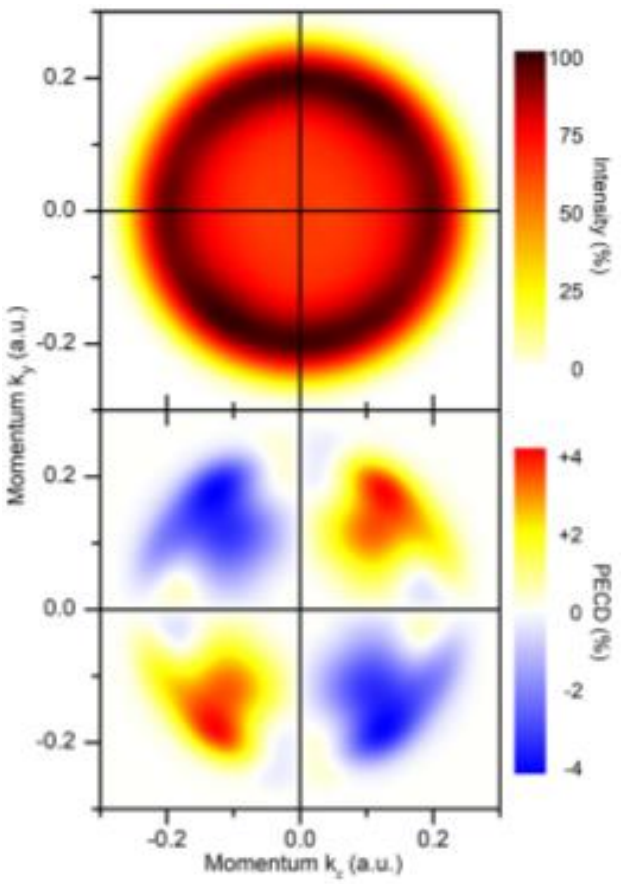

Figure 62. Computed results for six-red-photon and three-blue-photon ionization of R-(-)-fenchone: The PAD projection on the detector's yz surface (upper panel) and PECD asymmetries in the momentum space (lower pannel).[60]

The upper panel shows a forward-backward asymmetry (positive and negative k_z values) which is opposite for positive and negative values of k_y. The PECD asymmetries reach 4% and have opposite sign for negative and positive k_z values. Again, PECD is angular structured, showing the interference between the different ionization pathways.

In 2015 Yoshi-Ichi Suzuki and Toshinori Suzuki theoretically examined if electron correlation is accessible via symmetry breaking in photoelectron angular distribution with a single ionization.[61] The authors considered two-step ionization of cyclopropane via a doubly degenerate state to a double degenerate cation state. They expressed the photoelectron angular distributions as:

$$I(\theta,\varphi) = \sum_{L,M} B_{LM} Y_{LM}(\theta,\varphi) \text{ (Eq. 22)}$$

$Y_{LM}(\theta,\varphi)$ are the spherical harmonics and B_{LM} are the expansion coefficients. If the electron correlation is not taken into account, then B_{LM} is zero.

For fixed-in-space molecules of cyclopropane there are two types of phenomena in which electron correlation can arise. These are linear and circular dichroism in the photoelectron angular distribution. The photoelectron angular distributions are shown in Figure 63.

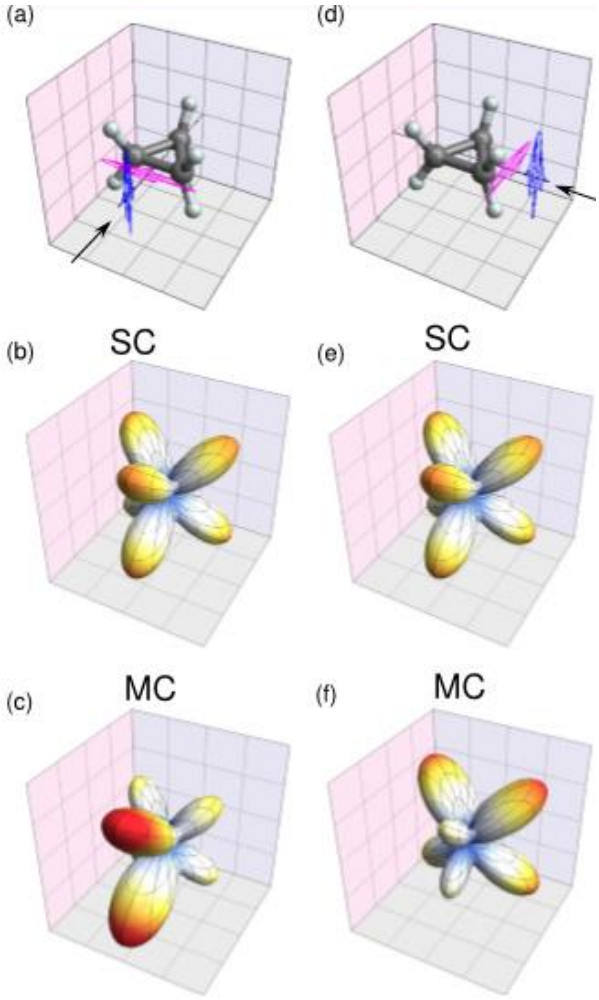

Figure 63. linear dichroism in photoelectron angular distribution of cyclopropane.[61]

In Figure 63a) a cyclopropane molecule is shown and two linearly polarized lasers. The photoelectron angular distributions are shown in Figure 63b) calculated with single-configuration wave function and in Figure 63c) with multiple-configuration of the 3p Rydberg. Figure 63d,e and f are the same as Figure 63a,b and c but with different light propagation.

The effect of electron correlation is shown in c) and f). The symmetry holds for the single-configuration wave function and does not change with the light propagation. In c) and f), the symmetry breaks in the photoelectron angular distributions in the multiple-configuration approximation and the asymmetries are large enough to be detectable experimentally. The degree of asymmetry depends on the photoelectron kinetic energy.

In the case of an isotropic ensemble of molecules, Figure 64 shows the photoelectron angular distributions of cyclopropane with two-step ionization via the 3s and 3p Rydberg states. The circular polarized excitation laser propagated along the z axis and the ionization laser light is linear parallel to the x axis and propagates in the z axis, too.

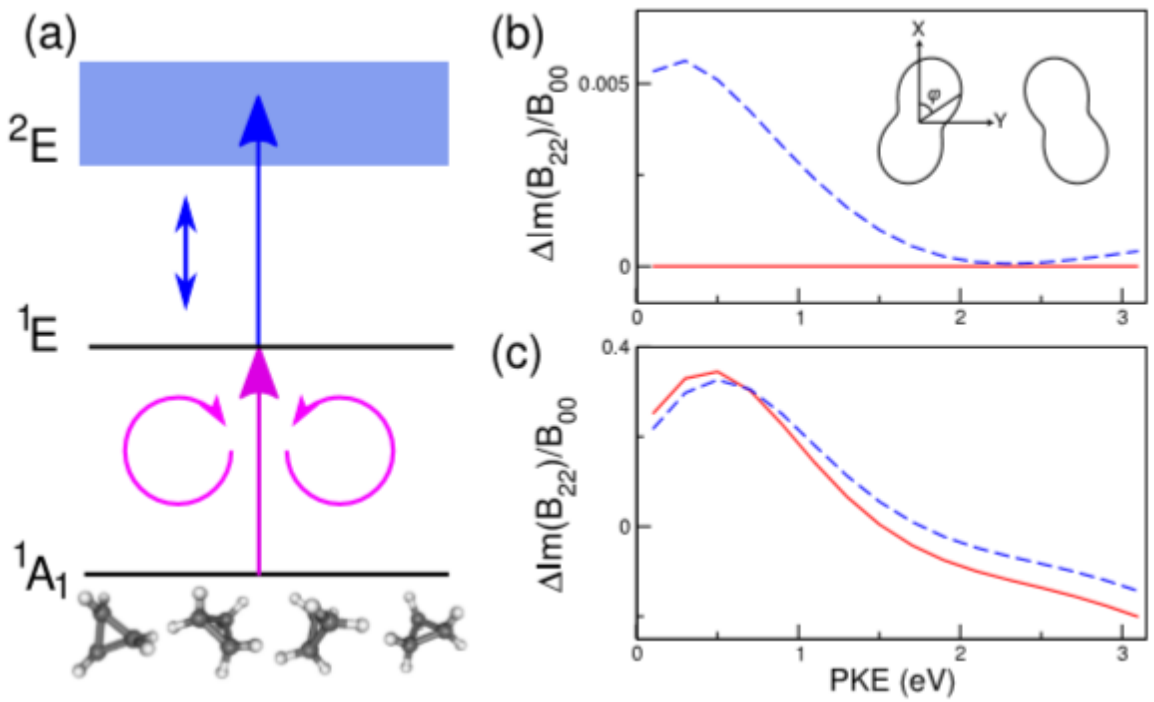

Figure 64. a) Excitation scheme for randomly oriented molecules, difference of anisotropy parameters for b) 3s Rydberg and c) 3p Rydberg.[61]

In Figure 64b and Figure 64c the red solid line represents the results in the single-configuration approximation and the dashed line the corresponding results in the multiple-configuration. In Figure 64b the 3s Rydberg state does not exhibit circular dichroism in the photoelectron angular distributions, however the dashed line in not zero due to electron correlation. The asymmetries in this case for the 3s Rydberg are extremely small.

Demekhin et al. in 2018 used a model methanelike chiral system and theoretically probed the access to PECD with an experiment with two overlapping laser pulses of frequencies ω and 2ω which are linearly polarized in two orthogonal directions.[62] The electric field can be expressed as:

$$\overrightarrow{E(t)} = \widehat{e_x}E_x g(t)cos(2\omega t) + \widehat{e_y}E_y g(t)cos(\omega t + \varphi) \text{ (Eq. 23)}$$

$E_{x,y}$ are the field amplitudes in the x and y direction respectively, $g(t)$ the time-envelope of the pulse and φ is the phase between the x and y components.

When the phase between the two components of the electric field is ±π/4 the field has a "butterfly" form and when the phase is 0 the corresponding form is a "horseshoe".

The proposed experiment is shown in Figure 65 with the forms of the electric field mentioned. Photoelectrons are emitted along the electric field in the up and down hemispheres and projected on the upper and down part of the velocity map imaging detector in the yz plane.

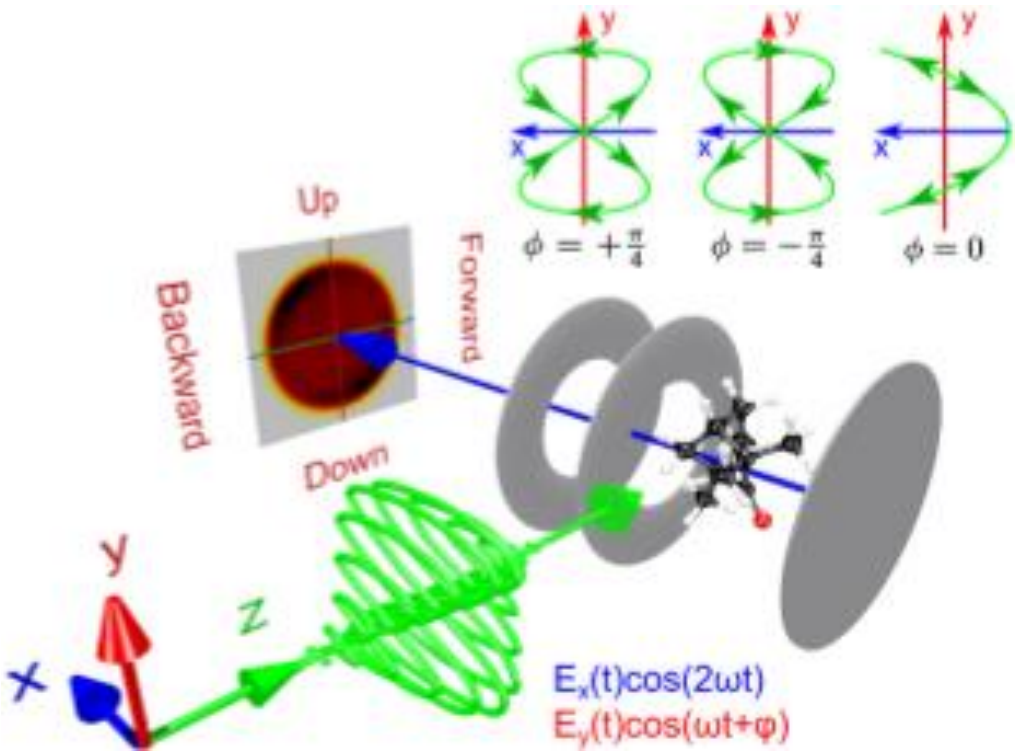

Figure 65. Experiment with bichromatic laser pulses propagating along the z axis and the electric field for different relative phases.[62]

A forward/backward asymmetry with respect to the light propagation axis is expected to be seen as upper/lower asymmetry on the detector. The authors simulated the experiment. The calculations were made with the time-dependent single center (TDSC) method and code for a methanelike chiral model shown in figure 60 considering equal peak intensities of the two laser pulses. Figure 66 shows the electron spectrum for a phase of $+\pi/4$, the individual contributions to the spectrum, the projection of the angular distribution of electrons on the detector and the PECD asymmetries.

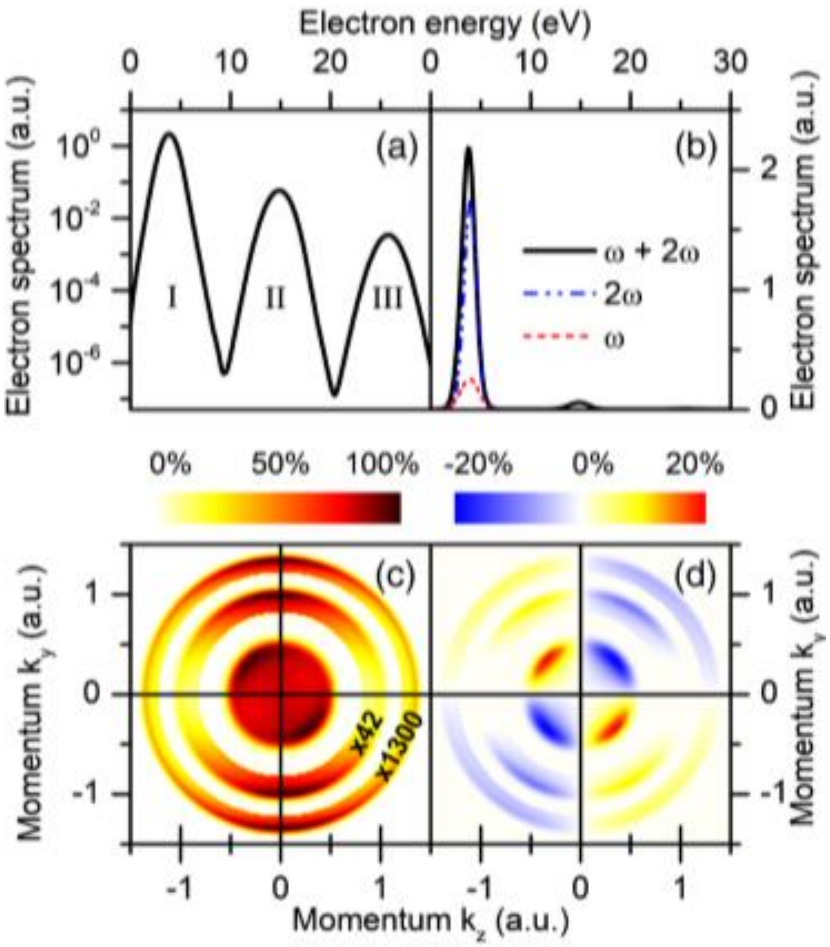

Figure 66. a) Electron spectrum for φ=+π/4, b) the individual contributions to the spectrum, c) the projection of the photoelectron angular distribution and d) the PECD asymmetries.[62]

Peak I in Figure 66a exhibits a PECD of 20% and peak II and III 11% and 6%, respectively. The same simulation technique was repeated for pulses with different peak amplitude. The corresponding computed PECD is larger than the one of Figure 66, suggesting higher sensitivity in enantiomeric excess experiments.

The follow year Demekhin showed that the predicted PECD induced by the interference of two fields in reference [62] has a chiral origin and suggested that a molecule introduces an internal relative phase between the two ionizing fields.[63]

He expressed the electric field using a spherical basis and the corresponding light-matter interaction. He then expressed the wave function of a photoelectron in the continuum as a superposition of spherical waves and the electric-dipole transition matrix elements in the molecular frame. With the Wigner's rotation matrices he wrote the total amplitude of the process D_T as a superposition of the amplitudes for the one photon ionization and the two photon ionization. He used that amplitude to write the differential cross section for the ejected photoelectrons as:

$$\frac{d\sigma}{d\Omega_P} = 2\pi|D_T|^2 = \sum_{LM} B_{LM} Y_{LM}^*(\hat{p})$$ (Eq. 24)

Y_{LM}^* are the spherical functions and $\hat{p} = (\theta_p, \varphi_p)$ is the direction of the emission of photoelectrons in the laboratory frame, with $\varphi_p$the relative phase between the two fields. The expansion in equation 22 has 3 contributions. One from one-photon ionization which concludes terms with L≤2, one from the two-photon ionization that includes terms with L≤4 and the cross product of the one and two-photon ionization amplitudes with L≤3. In this present work there is not only forward-backward asymmetry (z axis) but up and down (y axis), too. The combine asymmetry of these two is named forward-backward up-down (FBUD) asymmetry and can be written as:

$$FBUD(\theta_p, \varphi_p) = Acos(\theta_p)sin(\theta_p)sin(\varphi_p)sin(2\varphi - \delta)$$ (Eq. 25)

In equation 25 $A = A'e^{i\delta}$ and the phase δ depends on the transition amplitudes for the one- and two-photon ionizations.

For L=2, M= +1, J=2 and M_J=1 the coefficient A can be written in terms of three 3J-symbols. Using this expression and the three 3J-symbols the author concluded that only the partial waves of the same parity contribute to the FBUD asymmetry and that the summation of positive and negative angular momentum projections and light helicities cancel out, unless the molecule is chiral.

In 2019 Goetz et al. theoretically showed than quantum interference between two-photon ionization pathways strongly enhances PECD for the chiral molecule CHBrClF.[64] To do so the authors considered the Schrödinger equation with fixed nuclei and neglect relativistic effects and the wave function for one-particle and one-hole excitation as a manifold.

The Schrödinger equatione was solved with second-order perturbation theory, enabling that way the manipulation of quantum interferences between opposite-parity and same-parity pathways. In order to assume randomly oriented molecules, integration took place over all Euler angles γ_R. The result for the differential cross section is:

$$\frac{d^2\sigma}{d\varepsilon_k d\Omega_{k\prime}} \approx \int |\alpha_{i_0}^{k\prime(1)}(t;\gamma_R) + \alpha_{i_0}^{k\prime(2)}(t;\gamma_R)|^2 d^3\gamma_R$$ (Eq. 26)

$\alpha_{i_0}^{k\prime(1.2)}$ are the first and second-order corrections. Second-order terms account for two photon ionization with different orbitals α. The PECD asymmetries are calculated by expanding equation 24 into Legendre polynomials and subtracting the equation obtained with lcp and rcp light. PECD is expressed as percentage of the maximum of the photoelectron intensity. Figure 67 shows the PECD results for a) one-photon ionization b) an optimized bichromatic (ω, 2ω) pulse and c) interference in even-parity two-photon pathways and d), e) and f) the corresponding ionization schemes.

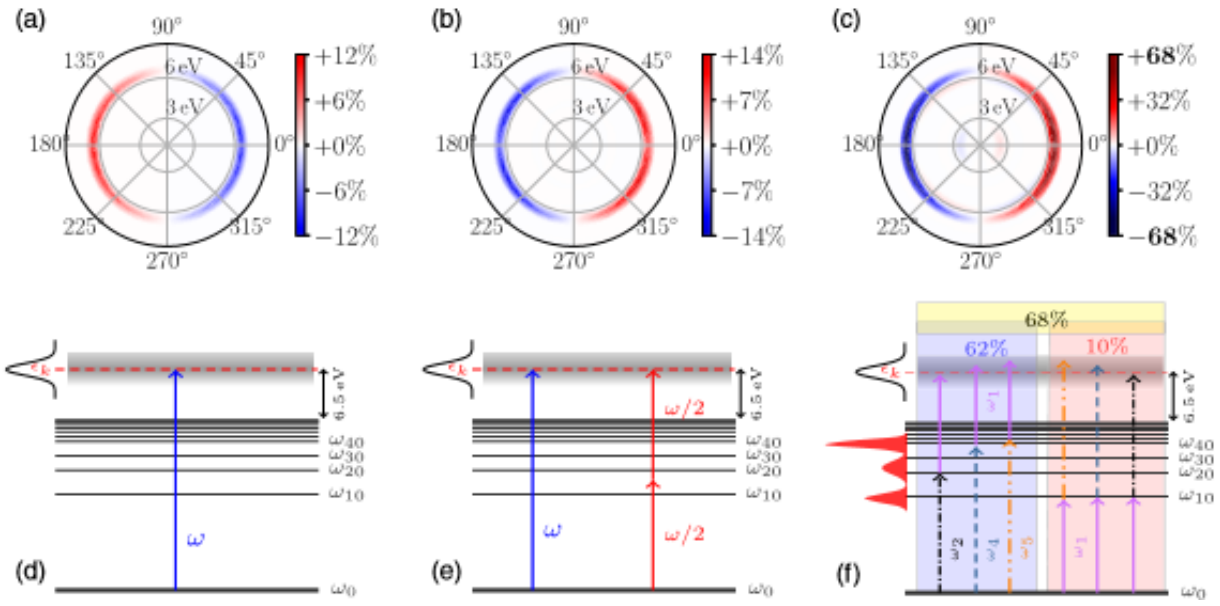

Figure 67. PECD results for a) one-photon ionization b) an optimized bichromatic (ω, 2ω) pulse and c) interference in even-parity two-photon pathways and d), e) and f) the corresponding ionization schemes.[64]

In the one-photon ionization the magnitude of PECD is of order 12%, in the optimized bichromatic pulse PECD reaches 20% and in the case of interference between two-photon ionization pathways PECD reaches 68%. Clearly, PECD is enhanced in the case of (1+1') REMPI with various photon pathways through different intermediate states to the same final state.

Chapter 2. 3D design of a PECD nozzle

1. Introduction

In this chapter the design of a PECD nozzle source will be described in detail. Section 2.2 explains the vacuum system in use and section 2.3 summarizes the basics on the creation of molecular beams. Section 2.4 describes the nozzle source.

2. Vacuum system

The PECD experiments are carried out in vacuum in order to avoid collisions which would disturb measurements of electron kinetic energy or spatial distribution. The molecular beam that is used a source for the chiral molecules under study, is produced inside a vacuum chamber. The vacuum chamber is equipped with appropriate windows, allowing the interaction between one or more laser beams and the molecular beam. The chiral molecules are ionized and the ejected electrons are guided by a system of electro-optics towards a position-sensitive detector.

The vacuum system used in this experiment is called “Diamante” and is shown in Figure 68. It consists of two chambers: the source chamber (A) and the detection chamber (B). The nozzle is placed in chamber A connected to an ISO (KF) 160 flange.

Chamber A is pumped by a 3000 L/sec diffusion pump (Leybold DI 3000) which is backed by a 65 m^3/h oil mechanical pump (Leybold Trivac D65B). A skimmer separates it from chamber B (detection chamber). In chamber B of Diamante the electro-optics setup and the position-sensitive detector are hosted. This section is pumped by a 340 $L*s^{-1}$ turbomolecular pump (Turbovac 361) which is backed by a 25.7 m^3/h mechanical pump (Leybold Trivac D25B).

The pressure in the source chamber is at 10^{-6} mbar (approximately 10^{-6} torr) and the foreline pressure between the diffusion pump and its back up mechanical pump is approximately 10^{-3} mbar. The detector chamber’s pressure is 10^{-7} mbar and the foreline pressure between the turbo pump and its back up mechanical pump is 10^{-3} mbar.

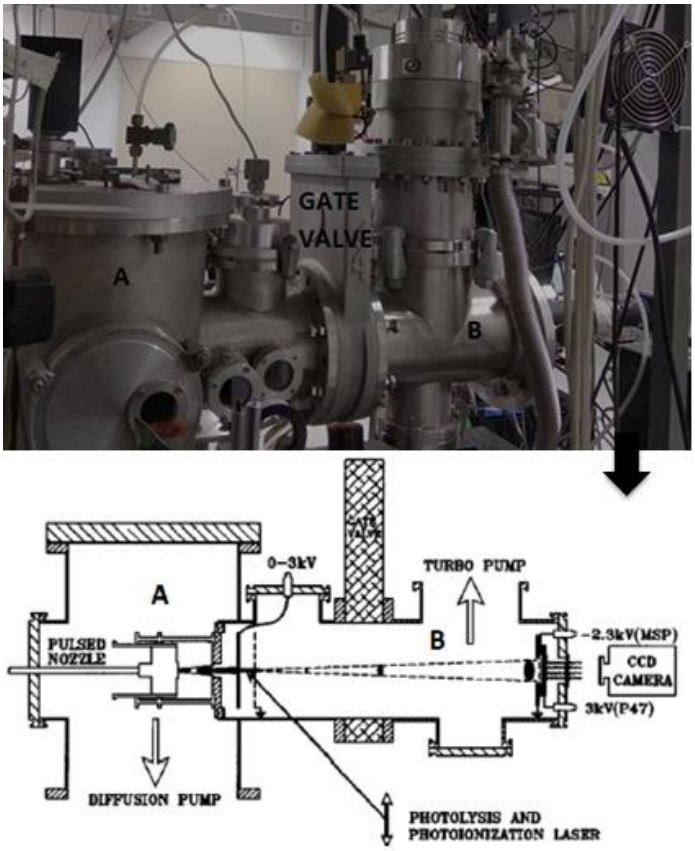

Figure 68. Vacuum system "Diamante".

During an experiment the pressure inside the source chamber increases up to 10^{-5} mbar. The pressure at the detector chamber has a maximum of 10^{-6} mbar. Chamber's pressure is measured with a cold cathode ionization gauge, the Leybold Vacuum GmbH PTR 225. The foreline pressure is measured by thermocouple gauges.

3. Molecular Beam

We use molecular beams in order to put molecules in a narrow range of initial energy states, narrower than that of a room-temperature Maxwell-Boltzmann distribution.[67] The molecules in the beam have high density, but (in the zone of silence) are still far apart and move independently of each other, thus collisions between them are negligible. They move in a well-defined direction with approximately equal velocities.

The main types of molecular beams are effusive and supersonic ones.[65] The principle behind the creation of a supersonic molecular beam from a nozzle source is the translation of the gas

thermal energy into directed mass motion.[66] The gas undergoes a free jet expansion under continuum conditions, shown in Figure 69.[67]

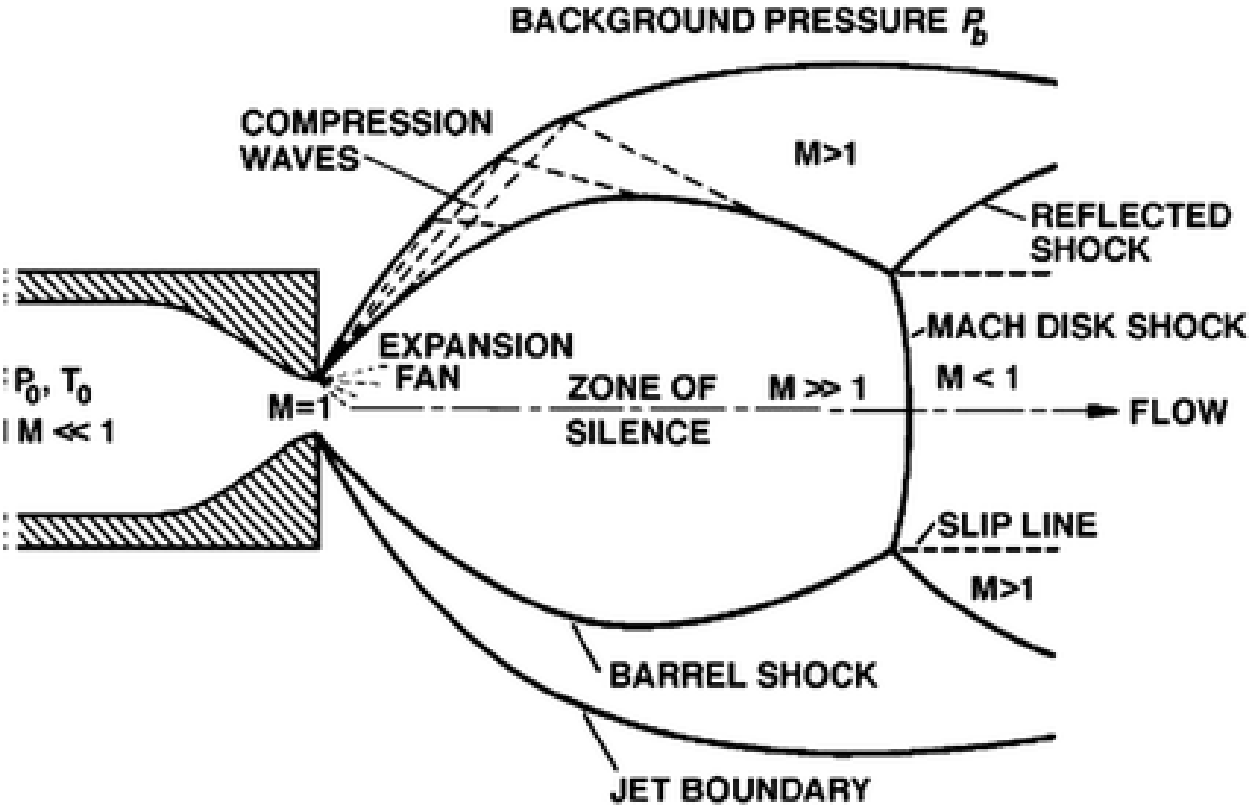

Figure 69. Free jet expansion under continuum conditions.[67]

In Figure 69 an (ideal) skimmer placed right after the nozzle (in the zone of silence) can isolated the central part of the beam. The zone of silence is an isentropic region that extends a few centimeters after the nozzle orifice.

The gas starts from the nozzle with small velocity, called the stagnation state with pressure P_0 and temperature T_0. From there it accelerates due to the difference in pressure between the initial state and the background pressure and the decrease of the nozzle volume towards the skimmer.

The Mach number (M) is used to describe the velocity of the flow in relation with the local speed of sound. If the mean velocity of the flow is below the one of sound, then $M < 1$. If the two velocities are equal then $M = 1$ and if the flow propagates in higher speed than the sound then $M > 1$. With that under consideration, the Mach number of the flow at the stagnation state is $M \ll 1$, as shown in figure 64.

There is a critical value G given by equation 25 that determines the exit pressure of the flow and its later behavior.

$$G = \left(\frac{\gamma+1}{2}\right)^{\frac{\gamma}{\gamma-1}} \text{ (Eq. 27)}$$

In equation 27 γ is the adiabatic constant characteristic of each gas.

G is less than 2.1 for all type of gases. If the pressure ratio $\frac{P_0}{P_b}$ is less than 2.1 then the speed of the flow is subsonic and its exit pressure is approximately equal to P_b. If the ratio is larger than G then the Mach number reaches the value of 1. In this case, the exit pressure of the flow does not depend on the background pressure and equals to $\frac{P_0}{G}$ a value larger than P_b. The flow undergoes a later expansion outside of the nozzle deformed by boundary conditions created by the background pressure.

As the expansion takes place, the Mach number increases and becomes larger than 1. Because the flow is supersonic, the information propagates in lower speed than the flow its self. Therefore, it is not aware of the boundary conditions (background pressure and M outside the nozzle).

Shock waves are a type of propagating disturbance moving faster than the local speed of sound with regions with different pressure, temperature, density and velocity gradients. These shock waves reduce the velocity of the flow, making it subsonic. Then the flow can adjust to the boundary conditions. In Figure 69 the compression waves, the reflected shock, the Mach disk shock and the barrel shock are shown. The latter compresses the flow at the sides and the Mach disk shock to the centerline.

Depending on the ratio $\frac{P_0}{P_b}$ it is possible for the flow to reexpand and create a pattern of expanding and compressing, however it is an unlikely scenario in the case of molecular beams.

All thermodynamics variables (temperature T, density n, pressure P) regarding the flow can be calculated considering an isentropic ideal gas expansion:

If the speed of sound for an ideal gas is $a = \sqrt{\gamma RT/W}$ with R the universal gas constant $8.314 J/mol \cdot K$, T the absolute temperature and W the molecular weight of the gas in kg/mol and $M \equiv V/a$ with V the velocity, then:

$$\frac{T}{T_0} = \left(1 + \frac{\gamma-1}{2}M^2\right)^{-1} \text{ (Eq. 28)}$$

$$V = \frac{M\sqrt{\gamma RT_0/W}}{\sqrt{1+\frac{\gamma-1}{2}M^2}} \text{ (Eq. 29)}$$

$$\frac{P}{P_0} = \left(\frac{T}{T_0}\right)^{\frac{\gamma}{\gamma-1}} \text{ (Eq. 28) and } \frac{n}{n_0} = \left(\frac{T}{T_0}\right)^{\frac{1}{\gamma-1}} \text{ (Eq. 30)}$$

4. Nozzle source

4.1 Nozzle operation

The operation of the Diamante nozzle is based on a piezoelectric crystal. A piezoelectric element changes its shape slightly when electric current runs through it. Therefore, when applying voltage difference on a piezoelectric crystal, one can change its dimensions. This crystal is mounted right below a poppet. The upper part of the poppet is inside the area where the gas is inserted and the corresponding molecular beam is formed by retracting the poppet which seals the expansion orifice.

The poppet encloses the small orifice from where the molecular beam will exit. The molecular sample is heated and enters the nozzle in the gas form. At this moment, the poppet encloses the orifice. Voltage difference is applied on the crystal and it slightly moves downwards, pulling the poppet away from the orifice, enabling the molecular beam to exit into the source chamber of "Diamante".

4.2. Nozzle designs

4.2.1 Nozzle assembly

The 3D design of the nozzle source was drawn using the Design Spark Mechanical program based on the designs of reference [68], which is in turn based on the design of Trickl and Proch[69]. The nozzle consists of 8 distinct parts that will be described in the next subsection.

The nozzle assembly is shown in Figure 70. All parts apart from the poppet are made of stainless steel. The poppet is aluminum or plastic.

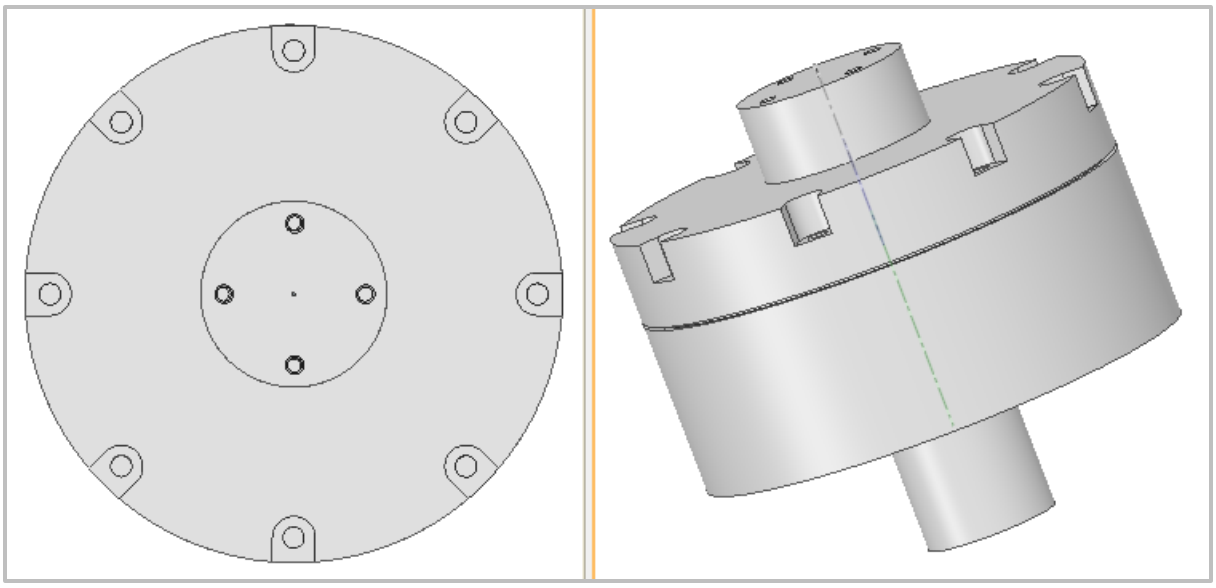

Figure 70. Nozzle assembly.

The cross-section assembly of the nozzle is shown in Figure 71. Part 3 houses the piezoelectric crystal.

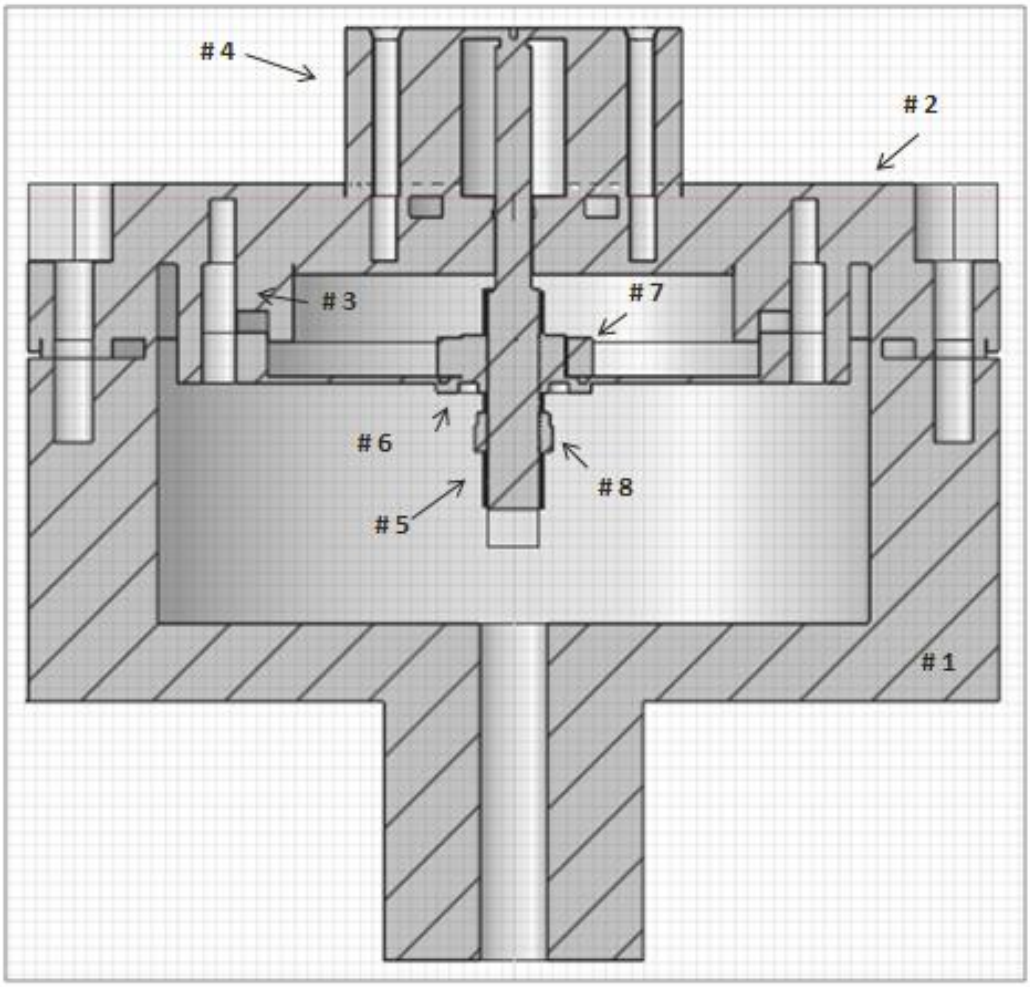

Figure 71. Cross section of the nozzle.

In Figure 71 each part of the nozzle is labelled. A tube of 6 mm diameter (Figure 72) is attached to part 4. Inside the tube, close enough to the nozzle there is cotton, wet with the molecular sample on it. A heating wire is tightened around the tube where the cotton is. Current of 1 A runs through the wire heating up the cotton up to 60-70 °C, in order for the molecules to evaporate. Then, the molecules in the gas form enter part 4 of the nozzle assembly.

Part 4 has an orifice of diameter 500 μm, sealed by part 5, which is a poppet equipped with an O-ring. A voltage of -700 V is applied to the piezoelectric crystal, forcing it to move downwards, pulling down a little bit the poppet. Thus, the poppet does not seal anymore the orifice and the molecular beam is created towards the interaction region. The circled region in Figure 72 is where the cotton is placed.

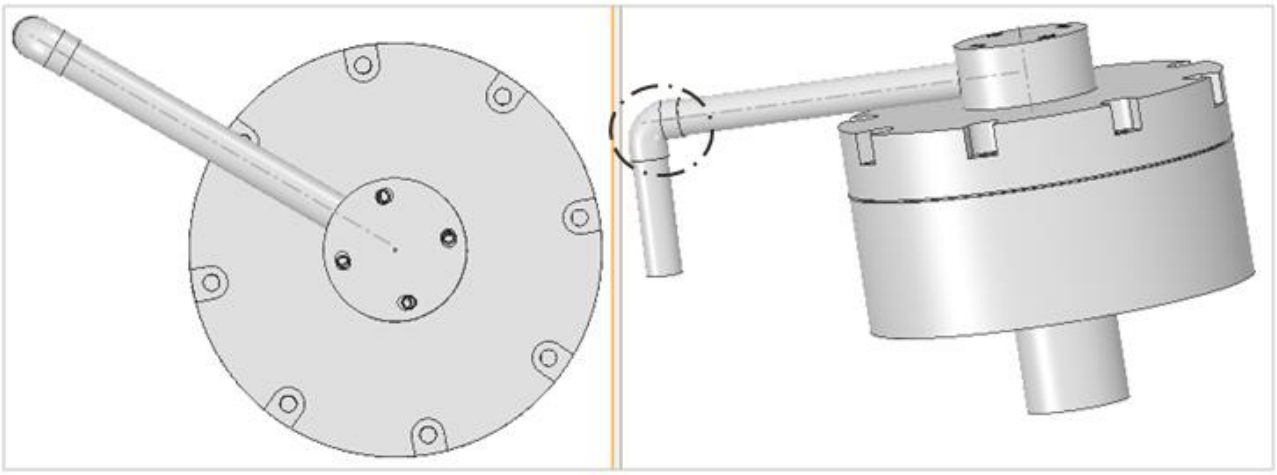

Figure 72. Nozzle with tube.

4.2.2. Parts of the nozzle assembly

Part 1 of the nozzle assembly labeled as # 1 in Figure 71 is the base of the nozzle.

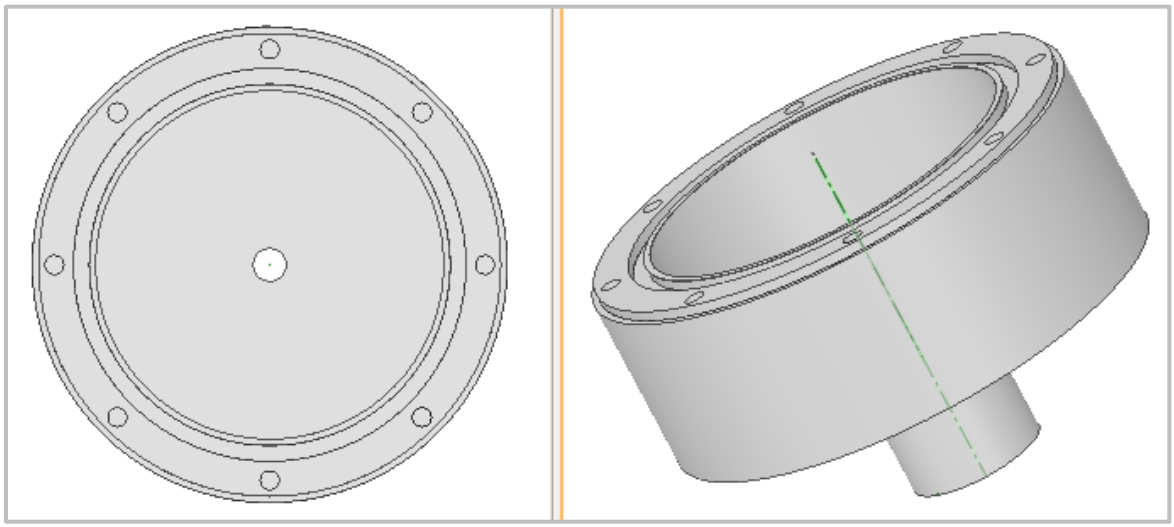

Figure 73. Part 1 of the nozzle assembly.

Eight symmetric holes with M3 threading are on a circle with diameter (6.8 ± 0.1) cm to fasten the rest of the nozzle on part 1. On the surface there is a small circular cavity with 1.5 mm depth and 0.1 mm tolerance, for an O-ring, if necessary.

Part 2 is mounted on part 1 with M3 screws. It is shown in Figure 74. On top of it there are two grooves (circular cavities) for O-rings: the outer groove is for an O-ring sealing part 4 and the

inner one is for O-rings sealing around the poppet (Part 5). The four (4) equidistant holes with M2 threading exist to screw part 4 on part 2.

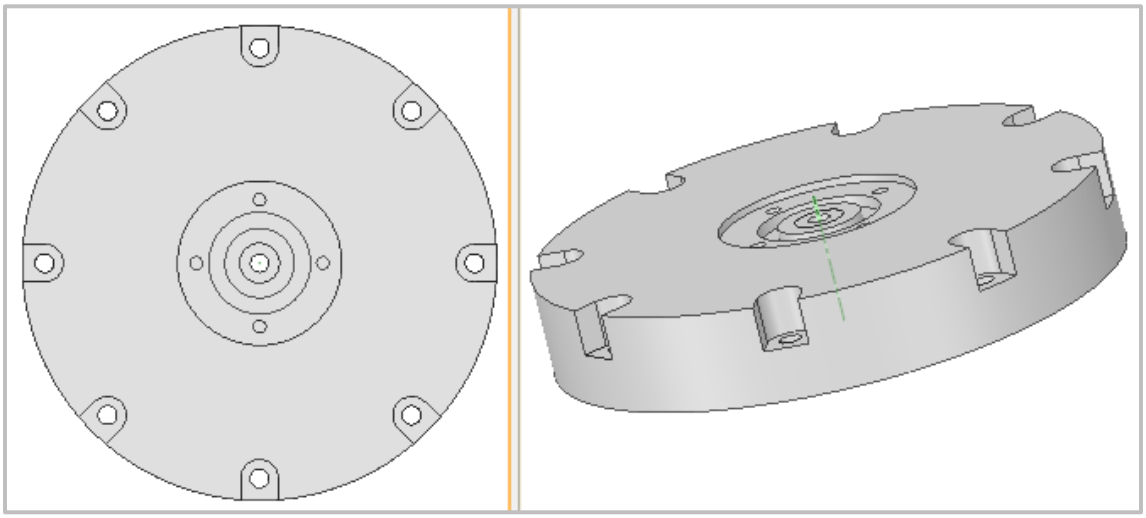

Figure 74. Part 2 of nozzle assembly.

Part 3 houses the crystal and connects on part 2 with 2 mm screws. It is shown in Figure 75.

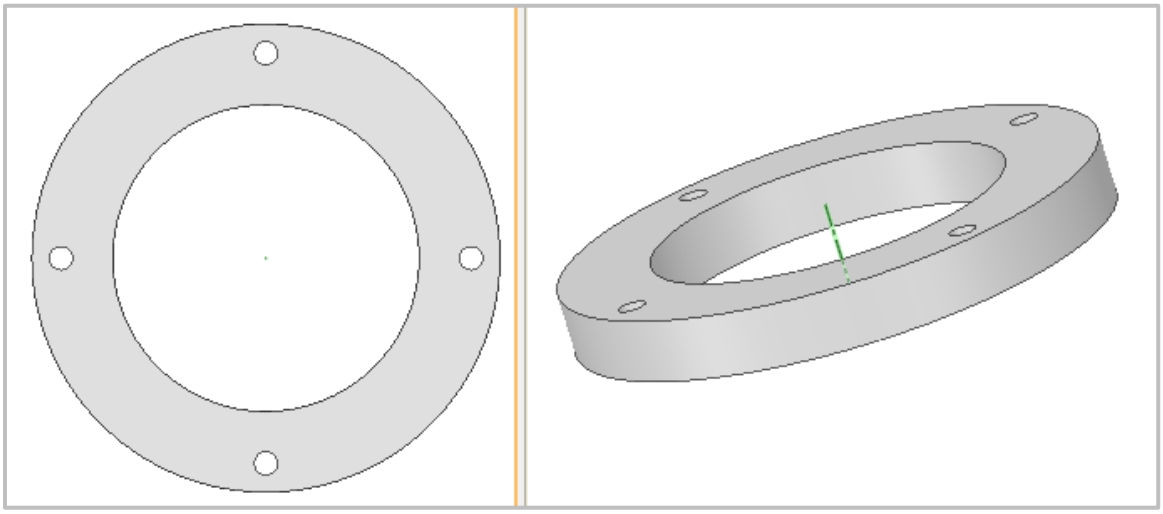

Figure 75. Part 3 of nozzle.

Right above part 2, is part 4 (Figure 76, Figure 77). Part 4 secures on part 2 with 4 M2 screws and seals with an O-ring. The inner area of Part 4 is the gas chamber. A 6 mm stainless steel tube welded on part 4 supplies the gas. A 90° angle stainless steel connector connects that tube with a 6 mm Teflon tube, extending (through a Cajon connector) outside the chamber and connecting to a gas manifold for seed gas supply. For this PECD nozzle, the 90° angle stainless steel connector is heated with heating wire and its temperature is monitored with K-type thermocouple. Another thermocouple attached on Part 4 monitors nozzle temperature, which should not exceed 100° C.

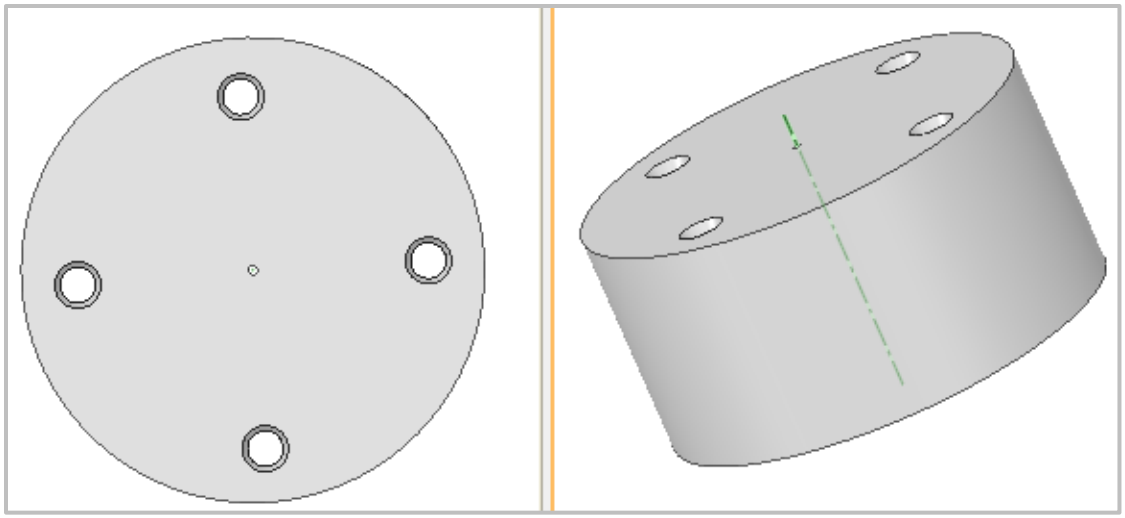

Figure 76. Part 4 of nozzle.

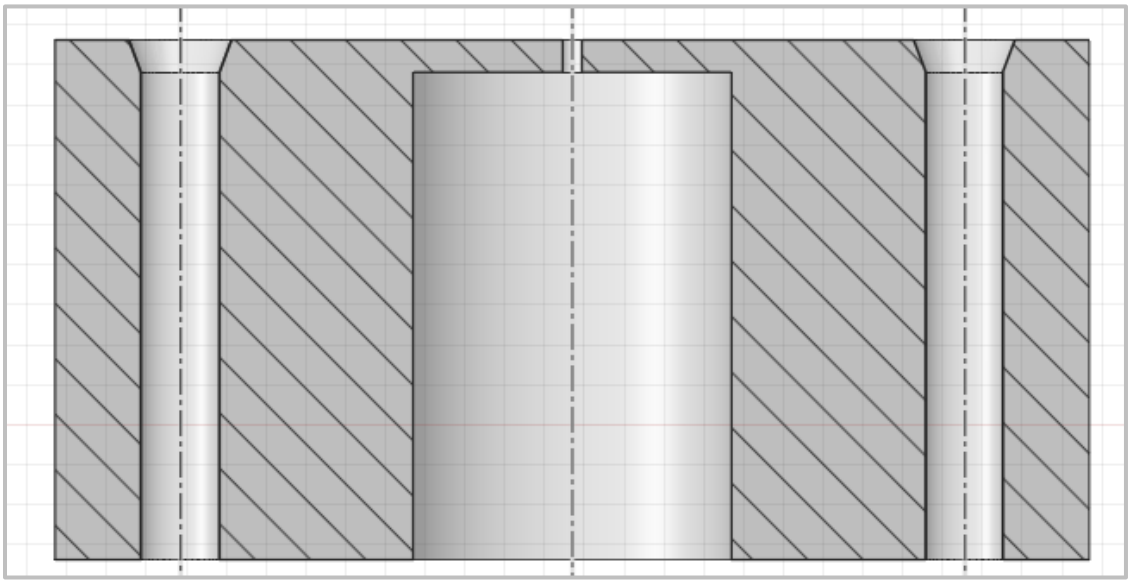

Figure 77. Cross section of part 4.

Inside part 4 the poppet (part 5) moves, sealing and unsealing the nozzle orifice. It has 40 mm length and M4 threading. It is shown in Figure 78. At the top of the poppet an O-ring is placed for sealing.

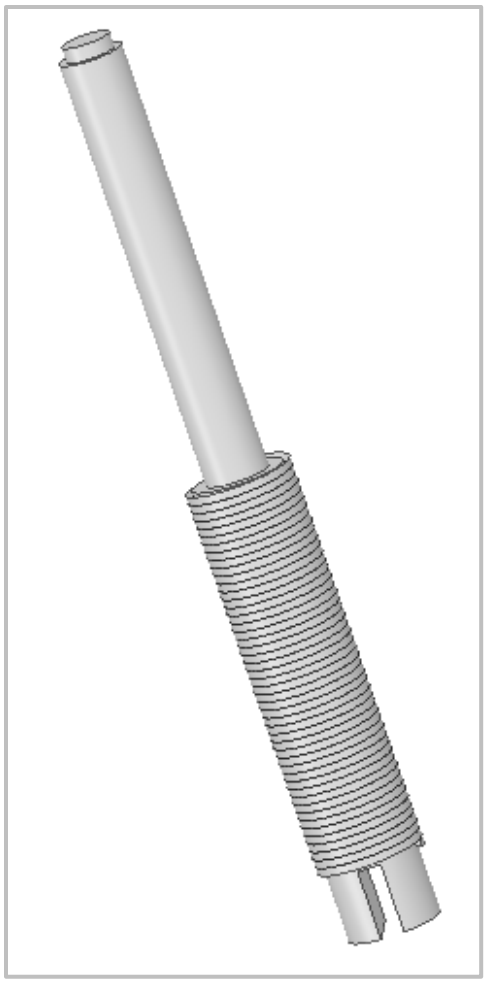

Figure 78. Part 5 of the nozzle assembly.

Parts 6 and 7 secure the poppet on the crystal assembly. Part 6 has internal thread of M4 and external thread M8 (Figure 79). Part 7 (Figure 80) tightly screws to part 6 with the crystal assembly in-between.

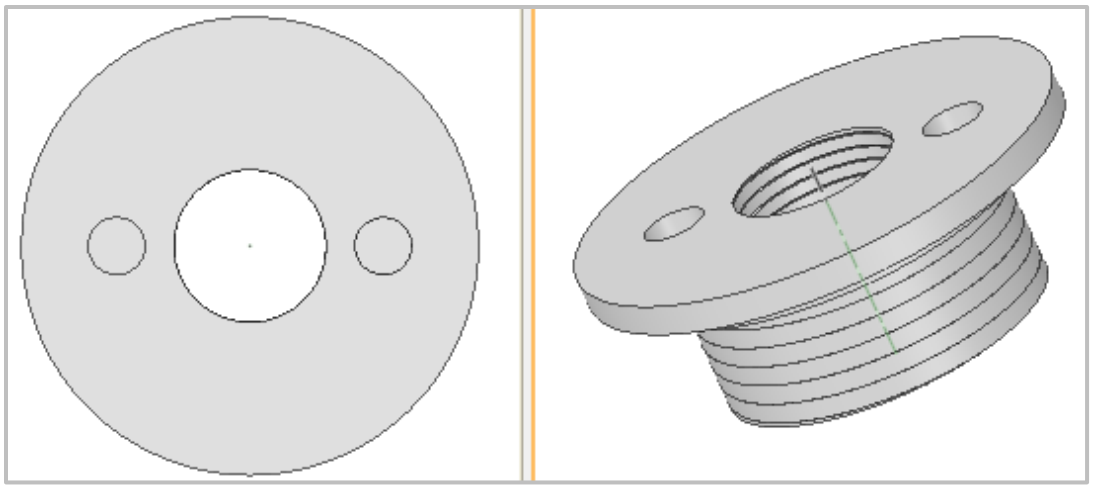

Figure 79. Part 6 of the nozzle assembly.

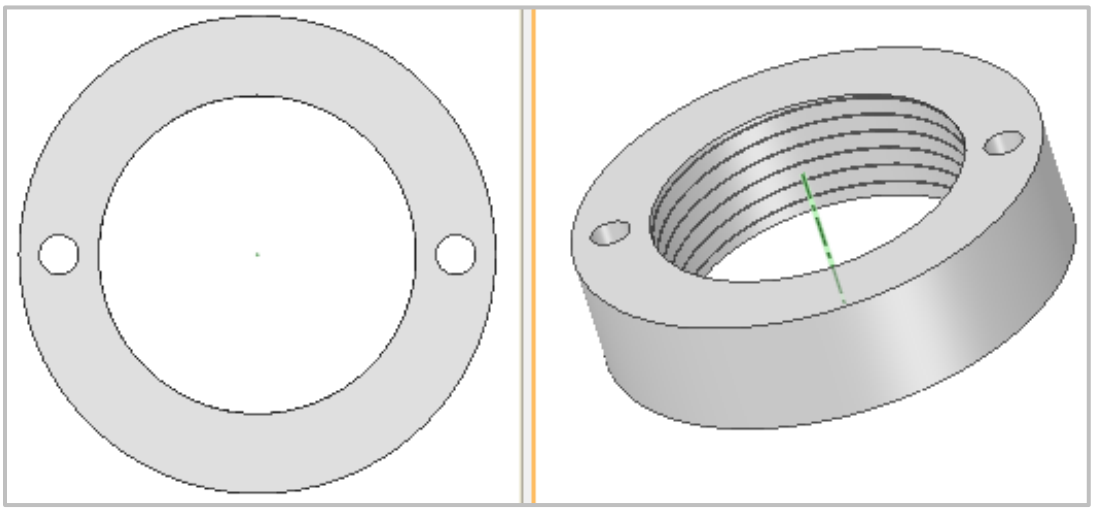

Figure 80. Part 7 of the nozzle assembly.

The last part, part 8 is an M4 nut (Figure 81), which secures the poppet in position after sealing adjustment.

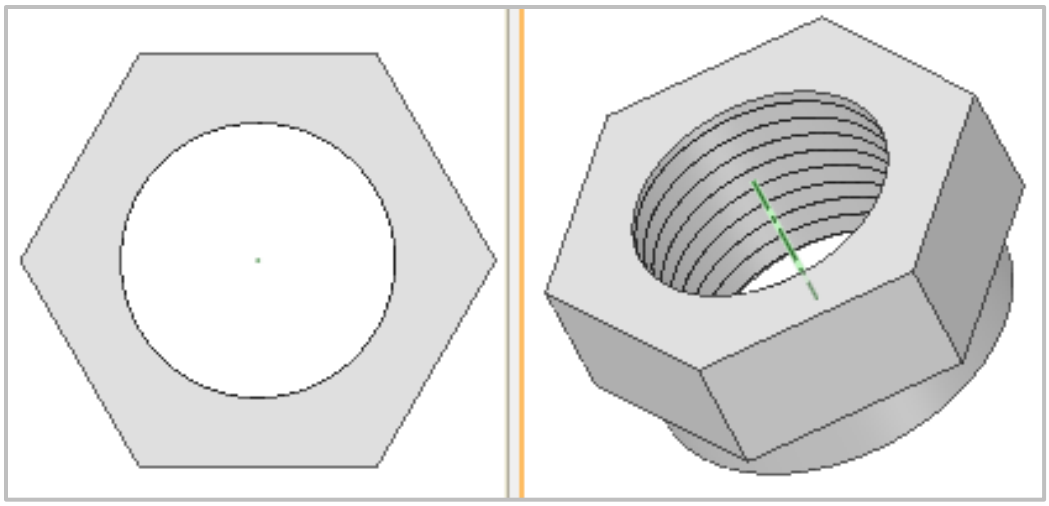

Figure 81. Part 8 of the nozzle assembly.

Gas supply tubing and wiring for nozzle and repeller as well as heating wire and thermocouple cables enter the vacuum through a ISO (KF) 160 flange.

ISO 160 flange that seals chamber A has two individual high voltage feedthroughs. Each high voltage feedthrough can each take up 10000 V and 30 A. One of them is used for the piezoelectric crystal (nozzle) and the other for the repeller. In the center of the flange there is one multi-pin feedthrough, with 9 pins that can take up 500 V DC and 3 A current each.

The heating wires and the K-type thermocouples used to measure temperature of heating area and nozzle are connected on pins of this connector. The flange is also equipped with a Cajon Ultratorr connector suitable for a 6 mm tube, leading to a gas manifold. The flange is shown in Figure 82.

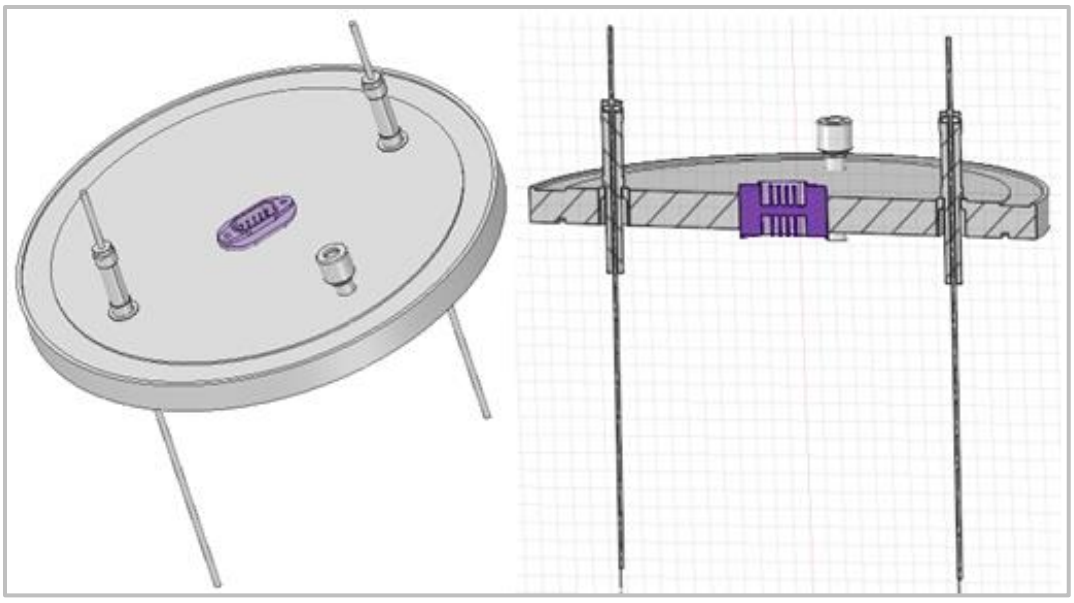

Figure 82. ISO 160 flange with multi pin feedhtough, two individual high voltage feedthroughs and a cajon.

References

[1] Atkins, P., & De Paula, J. (2013). Elements of physical chemistry. Oxford University Press, USA.

[2] Schellman, J. A. (1975). Circular dichroism and optical rotation. *Chemical Reviews*, *75*(3), 323-331.

[3] Gerald D. Fasman (1996). Circular dichroism and the conformational analysis of biomolecules.

[4] Woody, R. W. (1995). Circular dichroism. In Methods in enzymology (Vol. 246, pp. 34-71). Academic Press.

[5] Rodger, A., & Nordén, B. (1997). Circular dichroism and linear dichroism (Vol. 1). Oxford University Press, USA.

[6] Snyder, P. A., & Rowe, E. M. (1980). The first use of synchrotron radiation for vacuum ultraviolet circular dichroism measurements. Nuclear Instruments and Methods, 172(1-2), 345-349.

[7] Powis, I. (2008). Photoelectron circular dichroism: Chiral asymmetry in the angular distribution of electrons emitted by (+)-S-carvone. Chirality: The Pharmacological, Biological, and Chemical Consequences of Molecular Asymmetry, 20(9), 961-968.

[8] Ritchie, Burke. "Theory of the angular distribution of photoelectrons ejected from optically active molecules and molecular negative ions." Physical Review A 13.4 (1976): 1411.

[9] Rafiee Fanood, Mohammad M., Ivan Powis, and Maurice HM Janssen. "Chiral asymmetry in the multiphoton ionization of methyloxirane using femtosecond electron–ion coincidence imaging." The Journal of Physical Chemistry A 118.49 (2014): 11541-11546.

[10] Wigner, E. P. (1993). On the matrices which reduce the Kronecker products of representations of SR groups. In The Collected Works of Eugene Paul Wigner (pp. 608-654). Springer, Berlin, Heidelberg.

[11] Lehmann, C. S., Ram, N. B., Powis, I., & Janssen, M. H. (2013). Imaging photoelectron circular dichroism of chiral molecules by femtosecond multiphoton coincidence detection. The Journal of chemical physics, 139(23), 234307.

[12] Catone, D., Turchini, S., Stener, M. A. U. R. O., Decleva, P. I. E. T. R. O., Contini, G., Prosperi, T., ... & Zema, N. (2013). Photoelectron spectroscopy and circular dichroism of a chiral metal–organic complex. Rendiconti Lincei, 24(3), 269-275.

[13] Kastner, Alexander, et al. "Observation of photoelectron circular dichroism using a nanosecond laser." ChemPhysChem (2019).

[14] Böwering, N., Lischke, T., Schmidtke, B., Müller, N., Khalil, T., & Heinzmann, U. (2001). Asymmetry in photoelectron emission from chiral molecules induced by circularly polarized light. Physical review letters, 86(7), 1187.

[15] Eppink, A. T., & Parker, D. H. (1997). Velocity map imaging of ions and electrons using electrostatic lenses: Application in photoelectron and photofragment ion imaging of molecular oxygen. Review of Scientific Instruments, 68(9), 3477-3484.

[16] Plomp, V., Gao, Z., & van de Meerakker, S. Y. (2020). A velocity map imaging apparatus optimised for high-resolution crossed molecular beam experiments. *Molecular Physics*, e1814437.

[17] Dick, B. (2019). MELEXIR: maximum entropy Legendre expanded image reconstruction. A fast and efficient method for the analysis of velocity map imaging or photoelectron imaging data. Physical Chemistry Chemical Physics, 21(35), 19499-19512.

[18] Smith, L. M., Keefer, D. R., & Sudharsanan, S. I. (1988). Abel inversion using transform techniques. Journal of Quantitative Spectroscopy and Radiative Transfer, 39(5), 367-373.

[19] http://www.delmarphotonics.com/MCP_MCPImageIntensifiers/microchannel_plates.htm (last accessed: 24/09/20)

[20] Wiley, W. C., & McLaren, I. H. (1955). Time-of-flight mass spectrometer with improved resolution. Review of scientific instruments, 26(12), 1150-1157.

[21] http://www.chem.nottingham.ac.uk/PECD.php (last accessed: 11/09/2020)

[22] Garcia, Gustavo A., et al. "Circular dichroism in the photoelectron angular distribution from randomly oriented enantiomers of camphor." The Journal of chemical physics 119.17 (2003): 8781-8784.

[23] Nahon, L., Garcia, G. A., Harding, C. J., Mikajlo, E., & Powis, I. (2006). Determination of chiral asymmetries in the valence photoionization of camphor enantiomers by photoelectron imaging using tunable circularly polarized light. The Journal of chemical physics, 125(11), 114309.

[24] Stener, M. A. U. R. O., Di Tommaso, D., Fronzoni, G. I. O. V. A. N. N. A., Decleva, P. I. E. T. R. O., & Powis, I. (2006). Theoretical study on the circular dichroism in core and valence photoelectron angular distributions of camphor enantiomers. The Journal of chemical physics, 124(2), 024326.

[25] Powis, I., Harding, C. J., Garcia, G. A., & Nahon, L. (2008). A valence photoelectron imaging investigation of chiral asymmetry in the photoionization of fenchone and camphor. ChemPhysChem, 9(3), 475-483.

[26] Lischke, T., Böwering, N., Schmidtke, B., Müller, N., Khalil, T., & Heinzmann, U. (2004). Circular dichroism in valence photoelectron spectroscopy of free unoriented chiral molecules: Camphor and bromocamphor. *Physical Review A*, *70*(2), 022507.

[27] Garcia, G. A., Nahon, L., Harding, C. J., & Powis, I. (2008). Chiral signatures in angle-resolved valence photoelectron spectroscopy of pure glycidol enantiomers. Physical Chemistry Chemical Physics, 10(12), 1628-1639.

[28] Garcia, Gustavo A., et al. "Photoelectron circular dichroism spectroscopy in an orbitally congested system: the terpene endoborneol." The Journal of Physical Chemistry A 114.2 (2009): 847-853

[29] Garcia, G. A., Nahon, L., Daly, S., & Powis, I. (2013). Vibrationally induced inversion of photoelectron forward-backward asymmetry in chiral molecule photoionization by circularly polarized light. Nature Communications, 4(1), 1-6.

[30] Garcia, G. A., Dossmann, H., Nahon, L., Daly, S., & Powis, I. (2014). Photoelectron circular dichroism and spectroscopy of trifluoromethyl-and methyl-oxirane: a comparative study. Physical Chemistry Chemical Physics, 16(30), 16214-16224.

[31] Stranges, S., Turchini, S., Alagia, M., Alberti, G., Contini, G., Decleva, P., ... & Prosperi, T. (2005). Valence photoionization dynamics in circular dichroism of chiral free molecules: The methyl-oxirane. The Journal of chemical physics, 122(24), 244303.

[32] Catone, D., Turchini, S., Contini, G., Prosperi, T., Stener, M., Decleva, P., & Zema, N. (2017). Photoelectron circular dichroism of isopropanolamine. Chemical Physics, 482, 294-302.

[33] Tia, M., Pitzer, M., Kastirke, G., Gatzke, J., Kim, H. K., Trinter, F., ... & Henrichs, K. (2017). Observation of enhanced chiral asymmetries in the inner-shell photoionization of uniaxially oriented methyloxirane enantiomers. The journal of physical chemistry letters, 8(13), 2780-2786.

[34] Ganjitabar, H., Hadidi, R., Garcia, G. A., Nahon, L., & Powis, I. (2018). Vibrationally-resolved photoelectron spectroscopy and photoelectron circular dichroism of bicyclic monoterpene enantiomers. Journal of Molecular Spectroscopy, 353, 11-19.

[35] Lux, Christian, et al. "Circular dichroism in the photoelectron angular distributions of camphor and fenchone from multiphoton ionization with femtosecond laser pulses." Angewandte Chemie International Edition 51.20 (2012): 5001-5005.

[36] Ram, N. Bhargava, C. S. Lehmann, and M. H. M. Janssen. "Probing chirality with a femtosecond reaction microscope." EPJ Web of Conferences. Vol. 41. EDP Sciences, 2013.

[37] Rafiee Fanood, M. M., Powis, I., & Janssen, M. H. (2014). Chiral asymmetry in the multiphoton ionization of methyloxirane using femtosecond electron–ion coincidence imaging. The Journal of Physical Chemistry A, 118(49), 11541-11546.

[38] Lux, C., Senftleben, A., Sarpe, C., Wollenhaupt, M., & Baumert, T. (2015). Photoelectron circular dichroism observed in the above-threshold ionization signal from chiral molecules with femtosecond laser pulses. Journal of Physics B: Atomic, Molecular and Optical Physics, 49(2), 02LT01.

[39] Agostini, P., Fabre, F., Mainfray, G., Petite, G., & Rahman, N. K. (1979). Free-free transitions following six-photon ionization of xenon atoms. Physical Review Letters, 42(17), 1127.

[40] Eberly, J. H., Javanainen, J., & Rzążewski, K. (1991). Above-threshold ionization. Physics reports, 204(5), 331-383.

[41] Fanood, M. M. R., Janssen, M. H., & Powis, I. (2015). Enantioselective femtosecond laser photoionization spectrometry of limonene using photoelectron circular dichroism. Physical Chemistry Chemical Physics, 17(14), 8614-8617.

[42] Kastner, Alexander, et al. "Intermediate state dependence of the photoelectron circular dichroism of fenchone observed via femtosecond resonance-enhanced multi-photon ionization." The Journal of chemical physics 147.1 (2017): 013926.

[43] Lux, C., Wollenhaupt, M., Sarpe, C., & Baumert, T. (2015). Photoelectron circular dichroism of bicyclic ketones from multiphoton ionization with femtosecond laser pulses. ChemPhysChem, 16(1), 115-137.

[44] Beaulieu, Samuel, et al. "Multiphoton photoelectron circular dichroism of limonene with independent polarization state control of the bound-bound and bound-continuum transitions." The Journal of chemical physics 149.13 (2018): 134301.

[45] Miles, J., et al. "A new technique for probing chirality via photoelectron circular dichroism." Analytica chimica acta 984 (2017): 134-139.

[46] Singh, D., & Minns, R. Ultrafast Multiphoton Photoelectron Circular Dichroism in α-Pinene.

[47] Bond, C. M. M., & Greenwood, J. B. (2019, July). Asymmetric photoelectron emission from chiral molecules using a high repetition rate laser. In Journal of Physics: Conference Series (Vol. 1289, No. 1, p. 012027). IOP Publishing.

[48] Fehre, K., Eckart, S., Kunitski, M., Janke, C., Trabert, D., Rist, J., ... & Dörner, R. (2019). Link between Photoelectron Circular Dichroism and Fragmentation Channel in Strong Field Ionization. The Journal of Physical Chemistry A, 123(30), 6491-6495.

[49] Hofmann, C., Zimmermann, T., Zielinski, A., & Landsman, A. S. (2016). Non-adiabatic imprints on the electron wave packet in strong field ionization with circular polarization. New Journal of Physics, 18(4), 043011.

[50] Kastner, Alexander, et al. "Observation of photoelectron circular dichroism using a nanosecond laser." ChemPhysChem (2019).

[51] Kastner, A., Koumarianou, G., Glodic, P., Samartzis, P. C., Ladda, N., Ranecky, S. T., ... & Lee, H. G. (2020). High-resolution resonance-enhanced multiphoton photoelectron circular dichroism. Physical Chemistry Chemical Physics, 22(14), 7404-7411.

[52] Michel, L., & Zhilinskiı, B. I. (2001). Rydberg states of atoms and molecules. Basic group theoretical and topological analysis. Physics Reports, 341(1-6), 173-264.

[53] Mulliken, R. S. (1964). The Rydberg states of molecules. 1a parts I-V1b. Journal of the American Chemical Society, 86(16), 3183-3197.

[54] Powis, I. (2000). Photoelectron circular dichroism of the randomly oriented chiral molecules glyceraldehyde and lactic acid. The Journal of Chemical Physics, 112(1), 301-310.

[55] Davenport, J. W. (1976). Ultraviolet photoionization cross sections for N 2 and CO. Physical Review Letters, 36(16), 945.

[56] Dill, D., & Dehmer, J. L. (1974). Electron-molecule scattering and molecular photoionization using the multiple-scattering method. The Journal of Chemical Physics, 61(2), 692-699.

[57] Artemyev, A. N., Müller, A. D., Hochstuhl, D., & Demekhin, P. V. (2015). Photoelectron circular dichroism in the multiphoton ionization by short laser pulses. I. Propagation of single-active-electron wave packets in chiral pseudo-potentials. The Journal of chemical physics, 142(24), 244105.

[58] Müller, A. D., Artemyev, A. N., & Demekhin, P. V. (2018). Photoelectron circular dichroism in the multiphoton ionization by short laser pulses. II. Three-and four-photon ionization of fenchone and camphor. The Journal of Chemical Physics, 148(21), 214307.

[59] Lux, C. (2015). Molekulare Identifizierung chiraler Moleküle in der Gasphase mittels Femtosekundenlaserspektrometrie. kassel university press GmbH.

[60] Müller, A. D., Kutscher, E., Artemyev, A. N., & Demekhin, P. V. (2020). Photoelectron circular dichroism in the multiphoton ionization by short laser pulses. III. Photoionization of fenchone in different regimes. The Journal of Chemical Physics, 152(4), 044302.

[61] Suzuki, Y. I., & Suzuki, T. (2015). Linear and circular dichroism in photoelectron angular distributions caused by electron correlation. Physical Review A, 91(5), 053413.

[62] Demekhin, P. V., Artemyev, A. N., Kastner, A., & Baumert, T. (2018). Photoelectron circular dichroism with two overlapping laser pulses of carrier frequencies ω and 2 ω linearly polarized in two mutually orthogonal directions. Physical Review Letters, 121(25), 253201.

[63] Demekhin, P. V. (2019). Photoelectron circular dichroism with Lissajous-type bichromatic fields: One-photon versus two-photon ionization of chiral molecules. Physical Review A, 99(6), 063406.

[64] Goetz, R. E., Koch, C. P., & Greenman, L. (2019). Quantum control of photoelectron circular dichroism. Physical Review Letters, 122(1), 013204.

[65] Pilipenko, Y. K. (2005, May). Molecular Beams and Jets. In Proceedings of 8th International Workshop "Relativistic Nuclear Physics: from Hundreds of MeV to TeV", Dubna (pp. 246-251).

[66] Kantrowitz, A., & Grey, J. (1951). A high intensity source for the molecular beam. Part I. Theoretical. Review of Scientific Instruments, 22(5), 328-332.

[67] Scoles, Giacinto, ed. Atomic and molecular beam methods. Oxford university press, 1988.

[68] Diamantopoulou et al. 2011: http://dx.doi.org/10.1063/1.3592783

[69] 5D. Proch and T. Trickl, Rev. Sci. Instrum. 60, 713 (1989).